BIOAPPLICATIONS OF INTEGRATED MEMS CATHETER TRACKING SYSTEM FOR MRI AND SPLIT RING RESONATOR BASED GLUCOSE SENSOR

by

Emre Kuşakcı

B.S., Electrical and Electronics Engineering, Boğaziçi University, 2013

Submitted to the Institute for Graduate Studies in
Science and Engineering in partial fulfillment of
the requirements for the degree of
Master of Science

Graduate Program in Electrical and Electronics Engineering
Boğaziçi University

2015

BIOAPPLICATIONS OF INTEGRATED MEMS CATHETER TRACKING SYSTEM FOR MRI AND SPLIT RING RESONATOR BASED GLUCOSE SENSOR

APPROVED BY:

Assoc. Prof. Arda D. Yalçınkaya .....
(Thesis Supervisor)

Assist. Prof. Hamdi Torun .....

Assist. Prof. Onur Ferhanoğlu .....

DATE OF APPROVAL: 11.08.2015

ACKNOWLEDGEMENTS

Throughout my life I found them near me, feeling their compassion and guidance. I do not think that I can ever repay them, but I would like to dedicate this labor to my beloved parents Mustafa and Ayşe, my brother Ali Osman and my sisters Güldane and Merve.

The academic life is a path full of difficulties, but if one can find the right guide through this path, obstacles can be overcome. Therefore, I would like to express my deepest gratitudes to Professor Arda Deniz Yalçınkaya. He showed me how to look for a solution from different perspectives. Given the opportunity for taking part in MNCL lab, I had the chance to learn many things from various friends studying in this lab.

I would like to present my deepest thanks Prof Hamdi Torun for his professional approach to the encountered problems. He was very helpful during all this study. I would like to thank to Prof Onur Ferhanoğlu for accepting taking part in my thesis committee.

I would like to present my special thanks to Mehmet Yumak, for being a kind friend as well as being very helpful in cleanroom processes.

It is a duty for me to acknowledge the support of all my friends, my masters, my professors and all people who guided me and who have shaped my personality. I am really grateful to them.

I would like to thank my friends İsmail, Cihad, Rahmi, Alperen, Yasin, Semih, Yakup, Ahmet, Musa, Hüseyin, Manjur, Ramazan, Furkan, Ömer Faruk and many others which I believe the most precious people in the world. Among all, I am very thankful to all people in number 4 and number 5.

I owe my special thanks to Berk, Houssein, Baykal and Uraz for their devoted study and valuable contributions to the subject of my thesis. I would like to thank sincerely to Habib, Ida, Okan, Hikmet, Artun, Engin, Gonenç and all of my friends in MNCL and Beta family. Thank you all.

I would like to thank The Scientific and Technological Research Council of Turkey (TÜBİTAK) which supported this thesis study as a part of grant EEEAG 111E197.

Lastly, I would like to acknowledge the assistance of Turkish National Academy of Sciences Distinguished Young Scientist Award Program (TÜBA GEBİP).

ABSTRACT

BIOAPPLICATIONS OF INTEGRATED MEMS CATHETER TRACKING SYSTEM FOR MRI AND SPLIT RING RESONATOR BASED GLUCOSE SENSOR

This thesis mainly consists of design, implementation and characterization of two different types of resonators for bioapplications. The first part of the thesis is about the fabrication and characterization of two generations of nickel electroplated micro-electromechanical systems (MEMS) devices which will be used for catheter tracking in magnetic resonance imaging (MRI). MRI is an imaging technique which is widely used in medicine thanks to its high contrast and its being safe for human health. There are several techniques to track a catheter tip inside the MRI, most of them utilizing electrical interconnects for data readout and power transmission which in turn causes heating of the catheter tip. The heating problem can be overcome by devising an innovative system which uses optical power transmission and optical data readout. In this system, MEMS devices integrated to a complementary metal oxide semiconductor integrated circuit (CMOS IC) enable optical data readout via laser Doppler vibrometry (LDV). Both generations of MEMS resonators are fabricated by nickel electroplating which provides low stress devices. The second part of this thesis focuses on a bioapplication of split ring resonators (SRR) which are comparatively new to the biosensor field. The SRRs matched to 2 GHz resonant frequency will be modeled, fabricated, characterized and then they are used in glucose sensing. The reaction of glucose with glucose oxidase (GOx) enzyme changes the electromagnetic characteristics of the solution sample. Exploiting this property, the effect of reaction time, concentration, position, and volume of the sample on the resonance characteristics of the SRR was studied.

ÖZET

MRG İÇİN MEMS TÜMLEŞİK KATETER TAKİP SİSTEMİ VE YARIK HALKA ÇINLAYICI TEMELLİ GLUKOZ SENSÖRÜ BİYOUYGULAMALARI

Bu çalışma iki rezonatör biyouygulamasının tasarım, uygulama ve karakterizasyonundan oluşmaktadır. Tezin birinci kısım manyetik rezonans görüntüleme (MRG)'de kateter takibi için kullanılacak olan iki farklı jenerasyonda nikel elektrokaplı mikroelektromekanik sistem (MEMS) rezonatörlerin üretimi ve karakterizasyonu hakkındadır. MRG insan sağlığı açısından güvenli olması ve yüksek kontrastı sebebiyle tıpta çokça kullanılan bir görüntüleme tekniğidir. MRG içerisinde kateter ucunu takip etmenin çeşitli yöntemleri vardır; ancak bu yöntemlerin çoğu güç ve veri iletimi için ısınmaya yol açan elektriksel ara bağlantılar kullanmaktadır. Bu ısınma problemini optik güç iletimi ve optik data okunmasını mümkün kılan yeni sistemle aşmak mümkündür. Bu sistemde, bir bütünleyici metal oksit yarıiletken tümleşik çipe (CMOS IC) entegre edilen MEMS cihazlar lazer Doppler titreşimölçeri (LDV) ile optik data okumayı mümkün kılmaktadır. MEMS rezonatör nesillerinin ikisi de düşük yapısal gerilim sağlayan elektrokaplama ile üretilmişti. Tezin ikinci kısmında biyosensör alanına görece yeni olan yarık halka çınlayıcılar (YHÇ) çalışıldı. 2 GHz rezonans frekansına eşlenmiş YHÇ yapıları modellendi, üretildi, karakterize edildi ve ardından glucose algılamada kullanıldı. Glukozun glukoz oksidaz (GOx) enzimi ile reaksiyonunun çözelti örneğinin elektromanyetik özelliklerini değiştirir. Bu özellikten faydalanarak reaksiyon süresinin, örneğin yoğunluğunun, pozisyonunun ve hacminin YHÇ'nin rezonans karakteristikleri üzerindeki etkisi çalışıldı.

TABLE OF CONTENTS

ACKNOWLEDGEMENTS iii
ABSTRACT v
ÖZET vi
LIST OF FIGURES x
LIST OF TABLES xv
LIST OF SYMBOLS xvii
LIST OF ACRONYMS/ABBREVIATIONS xx
1. INTRODUCTION 1
1.1. Medical Tracking Systems 1
1.2. MRI Operating Principle and Proposed Model 3
1.3. Proposed Readout Method 4
2. THE FIRST GENERATION MEMS DEVICES 10
2.1. Design and Simulation of First Generation MEMS Bridges 10
2.1.1. Finite Element Simulations in COMSOL 10
2.1.2. Static Displacement Simulations on SolidWorks 13
2.2. Fabrication Process 18
2.2.1. The First Lithography 18
2.2.2. Sputtering 18
2.2.3. The Second Lithography 19
2.2.4. Nickel Electroplating 20
2.2.5. Releasing the Structures 20
2.3. Measurements and Outcomes 23
3. THE SECOND GENERATION MEMS DEVICES 29
3.1. Design and Simulation of Second Generation MEMS Bridges 30
3.1.1. Finite Element Simulations in COMSOL 30
3.1.2. Static Displacement Simulations on SolidWorks 35
3.1.3. Mask Design of Second Generation Devices 37
3.2. Fabrication Process 37

3.2.1. The First Lithography 41
3.2.1.1. Mask Aligner Calibration 42
3.2.2. Sputtering 43
3.2.3. The Second Lithography 44
3.2.4. Nickel Electroplating 45
3.2.4.1. Theoretical Background 45
3.2.4.2. Electroplating Bath Setup 47
3.2.4.3. Electroplating on PCB Copper 50
3.3. Outcomes 52
4. GLUCOSE MICROWAVE SENSOR WITH SRR 54
4.1. Introductory Information on Diabetes 56
4.2. Methods Used for Blood Glucose Sensing 57
4.2.1. Invasive Techniques 57
4.2.2. Reflectance Photometry 58
4.2.3. Amperometry and Coulometry 59
4.2.4. Noninvasive Techniques 59
4.3. Commercial Blood Glucose Measurement Devices 60
4.3.1. The Structure of BGM Strip 61
4.3.2. Working Principle of BGM 61
4.3.3. A Comparison between Commercial Sensors 64
4.4. The Proposed Model for Glucose Monitoring 64
4.4.1. The Tear Composition 65
5. FABRICATION, SIMULATION AND EXPERIMENTS OF SRR BASED GLUCOSE SENSING 68
5.1. Theoretical Modeling and Simulations of SRR Structures 68
5.2. Fabrication Methods 71
5.3. CST Simulations with and without DI water 75
5.4. Measurement Setup 78
5.5. Characterization Procedure and Results 79
5.5.1. The Effect of the Position of the Droplet 82
5.5.2. The Effect of Volume 85

5.5.3. The Effect of Concentration 86
5.5.4. The Effect of Reaction Time 89
6. CONCLUSION 92
REFERENCES 95

LIST OF FIGURES

Figure 1.1. Schematic of the proposed catheter system. 5

Figure 1.2. Proposed readout method. 7

Figure 1.3. Lorentz force acting on the resonator. 7

Figure 2.1. First generation single flexure device with diffraction gratings. . . 11

Figure 2.2. First generation double flexure device with perforations. 11

Figure 2.3. Six resonance modes with the lowest resonant frequency: (a) out of plane sliding, (b) torsional, (c) in plane sliding, (d) rocking, (e) Fifth mode, (f) Sixth mode. 12

Figure 2.4. Displacement simulation of a diffraction grated device under a DC force. 16

Figure 2.5. Displacement simulations of a MEMS resonator with a perforated mass under a DC force. 17

Figure 2.6. Photograph of the fabricated device taken by optical microscopy. . 21

Figure 2.7. Photograph of fabricated devices taken with AFM. 21

Figure 2.8. Characterization setup prepared for the first generation devices. . 24

Figure 2.9. The displacement measurement of an externally driven resonator. 25

Figure 2.10. Fiber butt-coupling on CMOS IC via a plexyglass cube. 26

Figure 2.11. Eight-device group driven by the CMOS IC characterization result. 27

Figure 3.1. Second generation beam type device. 31

Figure 3.2. Second generation resonator with perforated mass. 31

Figure 3.3. Displacement of a second generation resonator with a mass under a DC force. 35

Figure 3.4. Second generation devices mask for 10-device beam type group. . . 38

Figure 3.5. Second generation devices mask for five-device beam type group. . 38

Figure 3.6. Second generation devices mask for four-device group with masses. 38

Figure 3.7. Series connected resonators in a five-device beam type group. . . . 39

Figure 3.8. The proposed fabrication method for the second generation MEMS resonators: (a) first lithography, (b) sputtering, (c) second lithography, (d) electroplating, (e) releasing, (f) wet etching. 40

Figure 3.9. Micrograph of the second generation devices after the first lithography. 42

Figure 3.10. Mismatch problem in mask alignment prior to calibration. 42

Figure 3.11. Chromium-copper sputtered sample. 44

Figure 3.12. The photograph of second generation resonators taken by optical microscope after the second lithography. 45

Figure 3.13. The schematic of a sample nickel electroplating bath. 46

Figure 3.14. The photograph of the plating bath setup in cleanroom. 49

Figure 3.15. The front side of the anode holder designed in SolidWorks. 51

Figure 3.16. The back side of the anode holder designed in SolidWorks. 51

Figure 4.1. Some metamerials applications: (a) superlens, (b) magnifying hyperlens, (c) cloacking device. 55

Figure 4.2. Abbott's FreeStyle BGMS strip structure. 62

Figure 4.3. A collection of tear glucose level measurements on nondiabetic people since 1930. 67

Figure 5.1. Split ring resonator: relative dimensions. 69

Figure 5.2. Two media with different permittivities. 69

Figure 5.3. CST simulation results of SRRs designed with the hybrid calculational model. 72

Figure 5.4. A sample photograph of the devices taken out of laser cutter machine. 73

Figure 5.5. The fabricated SRRs with a chamber in the gap. 75

Figure 5.6. The simulation showing the resonance shift due to 1 μl DI water placed in the reservoir of SRR. 76

Figure 5.7. Electrical field distribution around the gap at the resonant frequency before DI droplet is placed. 76

Figure 5.8. Electrical field distribution around the gap at the resonant frequency after DI droplet is placed. 77

Figure 5.9. Surface current induced on the resonator. 77

Figure 5.10. Characterization setup used for SRR microwave glucose sensing tests. 79

Figure 5.11. The resonator holder designed for glucose measurement setup. . . 80

Figure 5.12. The fasTTest glucose test strips used in experiments as an enzyme source. 80

Figure 5.13. The measurement positions with respect to gap: (i) left end, (ii) left boundary, (iii) gap center, (iv) right boundary and (v) right end. 82

Figure 5.14. The effect of DI droplet placed on the left side of the resonator. . 83

Figure 5.15. The effect of DI droplet placed on the left boundary of the gap. . 83

Figure 5.16. The effect of DI droplet placed on the gap. 84

Figure 5.17. The effect of DI droplet placed on the right boundary of the gap. . 84

Figure 5.18. The effect of DI droplet placed on the right side of the resonator. . 84

Figure 5.19. The effect of DI droplet volume. 85

Figure 5.20. The effect of concentration on resonant frequency and dip value at 30 seconds. 88

Figure 5.21. The effect of concentration on resonant frequency and dip value at 90 seconds. 88

Figure 5.22. The effect of concentration on resonant frequency and dip value at 150 seconds. 88

Figure 5.23. Resonant frequency change during reaction for different concentrations. 89

Figure 5.24. Resonance dip change during reaction for different concentrations. 90

LIST OF TABLES

Table 2.1. The geometries of all first generation devices. 14

Table 2.2. Resonant frequencies of all first generation devices in six modes (kHz). 15

Table 2.3. The complete recipe for the first generation devices. 22

Table 2.4. The measured and simulated resonance characteristics of eight-device group. 27

Table 3.1. 10-beam type device groups. 33

Table 3.2. Five-beam type device groups. 34

Table 3.3. Groups with four resonators with perforated mass. 34

Table 3.4. DC displacement for the devices in G1 and G2 groups. 36

Table 3.5. DC displacement for the devices in G4 and G5 groups. 36

Table 3.6. DC displacement for the devices in G3 and G6 groups. 37

Table 3.7. Activity series for metals. 43

Table 3.8. Prepared electroplating bath compositions and operating conditions. 49

Table 3.9. Change of plating thickness with time. 52

Table 4.1. Main tear film chemical concentrations and corresponding values in blood. 67

Table 5.1. SRR dimensions determined with analytical model. 71

LIST OF SYMBOLS

A	Cross-sectional area of interest
a	Width of the gratings
$\vec{B}$	Arbitrary magnetic field
b	Width of the separation between gratings
$\vec{B_0}$	Static DC magnetic field vector
B_0	Magnitude of static DC magnetic field vector $\vec{B_0}$
$\vec{B_1}$	Oscillating magnetic field vector
$\vec{B}_{grad}(x)$	Gradient magnetic field vector along x direction
$B_{grad}(x)$	The magnitude of $\vec{B}_{grad}(x)$
C	Capacitance
c	Separation between two consequitve rings
C_{gap}	Gap capacitance of SRR
C_{surf}	Surface capacitance of SRR
c_d	Damping coefficient
Ca^{2+}	Calcium ion
Cl^-	Chloride ion
d	FR4 substrate thickness
$\vec{dl}$	Infinitesimal vector along the current propagation direction
E	Young's modulus
$\vec{F}_d$	Force driving the resonator motion
$\vec{F}_{lorentz}$	Lorentz force vector
$f_{isocenter}$	Resonance frequency of isocenter of MRI bore
f_{FID}	Frequency of free induction decay signal
f_{larmor}	Larmor frequency
f_{meas}	Measured resonant frequency
f_{ref}	Frequency of reference RF pulse
f_{sim}	Simulated resonant frequency
f_{srr}	Resonant frequency of SRR

f_x	Center frequency of the received output signal
fl	Flexure length
g	Gap width
G_x	Strength in the gradient field applied in the x axis
$G1$	The first group in second generation design
$G2$	The second group in second generation design
$G3$	The third group in second generation design
$G4$	The fourth group in second generation design
$G5$	The fifth group in second generation design
$G6$	The sixth group in second generation design
^1H	Hydrogen nucleus
h	Height of the copper plane
$HC0_3^-$	Bicarbonate ion
I	Moment of inertia for out of plane sliding motion
J	The magnitude of current density
$\vec{j}$	Unit vector along y-axis
$\vec{k}$	Unit vector along z-axis
K^+	Potassium ion
k_0	Spring constant of the mechanical structure
k_e	Elastic spring constant
L	Inductance
$\vec{l}$	Vector equal magnitude to the total length of MEMS bridges
l	Total length of the resonator beam
l_s	Width and length of the substrate plane for SRR structures
L_{eff}	Effective inductance of SRR
lf	Length of the flexure
lm	Length of the mirror
$\vec{M}_u$	Net magnetic moment vector in $\vec{u}$ direction
m	Mass of the mirror
Mg^{2+}	Magnessium ion
mw	Mirror width

Na^+	Sodium ion
r	Inner radius of the resonator
R_m	Average radius of a single ring SRR
t	Thickness of the resonator
t_f	Capillary chamber filling time
$\vec{u}$	Arbitrary direction vector
w	Copper width
x_f	Length along the filling axis of the capillary chamber
$\vec{z}$	Position vector along z axis
$\dot{\vec{z}}$	The first derivative of the position vector along z axis
$\ddot{\vec{z}}$	The second derivative of the position vector along z axis
α	Absorption coefficient of light
Δx	The distance of the micro-coil from the isocenter of the MRI bore
Δz_{max}	Maximum DC displacement in out of plane direction
ϵ_{eff}	Effective perimittivity
ϵ_r	Relative perimittivity of the substrate medium
γ_{gyr}	Gyromagnetic ratio
μ	Viscosity of the sample droplet
μ_o	Permeability of the free air
ω_F	Angular frequency of the driving force
ω_s	Measured resonant frequency of the stressed beam
ρ	Mass density
σ	Residual stress
σ_l	Liquid surface tension
θ_w	Wetting angle

LIST OF ACRONYMS/ABBREVIATIONS

2D	Two dimensional
3D	Three dimensional
AFM	Atomic force microscopy
BGMD	Blood glucose monitoring devices
BGMS	Blood glucose monitoring sensors
CMOS	Complementary metal-oxide semiconductor
DC	Direct current
DGI	Diffraction grating interferometry
DI	Deionized
EMTS	Electromagnetic tracking systems
FAD	Flavin adenine dinucleotide
FID	Free induction decay
FR4	Flame retardant 4
GDH	Glucose dehydrogenase
GOx	Glucose oxidase
GRIN	Gradient-index
IC	Integrated circuit
IR	Infrared
LDV	Laser Doppler vibrometry
LED	Light emitting diode
MEMS	Micro-electromechanical systems
MR	Magnetic resonance
MRI	Magnetic resonance imaging
OTS	Optical tracking systems
PQQ	Pyrroloquinoline quinone
PR	Photoresist
RF	Radio frequency
SRR	Split ring resonator

UV	Ultraviolet
XF	X-ray fluoroscopy

1. INTRODUCTION

In this thesis, two bioapplications of micro electromechanical systems (MEMS) bridges and split ring resonators (SRR) will be presented. The first bioapplication is of MEMS bridges utilized in an optical catheter tracking system. After providing the theoretical information about medical tracking systems and MRI operation principals; design, simulation, fabrication and characterization of two different MEMS bridges will be explained in details. This part of the thesis is up to Chapter 4. After Chapter 4, another bioapplication this time of SRRs will be presented. The SRR bioapplication study is about an innovative noninvasive glucose monitoring technique. In this second part of the thesis, first of all the commerical, noncommercial, invasive and noninvasive glucose monitoring techniques will be presented. Then, analytical SRR modeling, simulation and fabrication of split rings will be explained. Finally, the experimental results of the effects of sample droplet position, volume, concentration and reaction time on the resonance characteristics of SRR will be demonstrated.

1.1. Medical Tracking Systems

The tracking systems are vital in clinical cases, particularly in minimally invasive surgical operations. The operational instrument relative to the patient's anatomy should be found and tracked as accurately as possible which is necessary for the success of the operation as well as minimal tissue deformation during the operation. The requirements to track the instrument position correctly, led rapid innovations and new techniques in this field.

The first tracking systems were mechanical [1]. Using a mechanical digitizer with a robotic arm with several linkages [2] they could provide accurate position information for the time [3]. Even though they are reliable and can have an accuracy around 2-3 mm at the time they were first introduced [4], they have several limitations, such as operation complexity, hygiene maintenance and primarily the inability to track multiple devices. Therefore as an alternative method, ultrasonic transducers were

developed and used for localization [5,6]. The ultrasonic position sensing devices were using the speed of sound. The speed of sound is very dependent on environmental factors and ambient characteristics such as air humidity or temperature. This makes ultrasound tracking technique prone to the obstruction. The ultrasonic signals also diminishes very quickly as they go further into the body.

Therefore, optical tracking systems (OTS) [7,8] and image based computational techniques [9] were adopted by the field, rapidly. The precision of OTS is really good, but it has the line of sight problem. For tracking the instrument, the line of sight between the instrument and tracking system should always be maintained, which may not be possible inside the body. Image based computational techniques generally uses X-ray fluoroscopy (XF). However, XF uses ionizing radiation which can be harmful to the operation staff and the patient [10,11].

Another technique used is electromagnetic tracking systems (EMTS) [12–14] for MRI systems. EMTSs are not affected by the line of sight problem and MRI does not use ionizing radiation during the operation and their contrast agents are harmless comparatively [15]. This type of localization can track a catheter tip or a needle inside the body. They have lower resolution compared to OTS but have good soft tissue contrast. Also they can provide three dimensional (3D) images whereas XF can provide only two dimensional (2D) images.

Every tracking system has its advantages and disadvantages. The choice of tracking technique is therefore, very application dependent. It is necessary to know how much working space is available, what the minimum resolution allowed in that operation is and the how tight the safety conditions are. EMTS is a promising tracking technique comparing to OTS and XF, however, it has its own problems. It is prone to parasitic distortion due to the presence of metals. Also due to eddy currents induced on the catheter tip and utilization of electrical interconnects for power and data transmission can lead to heating problem at the catheter tip.

1.2. MRI Operating Principle and Proposed Model

Since the proposed system for catheter tracking will be used in magnetic resonance imaging (MRI), it would be better to explain the working principle of MRI. The nuclei of atoms spin around themselves randomly, so that they have either an upspin or downspin magnetic dipole moment. For a closed system, in which there is no external magnetic field, the number of upspin dipoles is exactly equal to the number of downspin dipoles. That is, the net magnetic moment in direction u ($\vec{M}_u$) is always zero in a closed system.

If a DC magnetic field $\vec{B_0}$ is applied in $\vec{k}$ direction perpendicular to the xy plane, some of the nuclei align themselves with the same direction with $\vec{B_0}$, which in the end causes a net magnetic moment greater than zero in $\vec{k}$ direction. Note that the net magnetic moment in xy plane is still zero. In the meantime, the nuclei make a precession movement around the $\vec{k}$ direction with a specific frequency called the Larmor frequency (f_{larmor}). It is related to the magnitude of $\vec{B_0}$ (B_0) by a constant known as the gyromagnetic ratio γ_{gyr} which can be seen in Equation 1.1.

$$f_{larmor} = \gamma_{gyr} B_0 \tag{1.1}$$

The gyromagnetic ratio has a unit of Hz/T. The value of γ_{gyr} is determined by the type of nuclei [16]. Since it is very abundant in human body, hydrogen nuclei (^1H) is utilized in MRI applications. The value of γ_{gyr} for ^1H is 42.576 MHz/T, so that for a 3 T MRI environment f_{larmor} is 127.728 MHz.

If an RF pulse $\vec{B_1}$ with f_{larmor} is applied in $\vec{j}$ direction, the energy carried by this pulse is absorbed by the ^1H nuclei which causes distortions from the precession angle around $\vec{k}$ direction. Nuclei absorb energy so that their magnetic moment axis deflects more from the precession axis ($\vec{k}$). When (^1H) dipoles return their equilibrium states they emit a signal called as free induction decay (FID) during relaxation. The decaying rate is dependent on the tissue type.

To determine the position of the signal another DC field with a gradient along x direction ($\vec{B}_{grad}(x)$) is applied just after the RF pulse so that the frequency of FID signal (f_{FID}) change with the position along the x axis as in Equaiton 1.2.

$$f_{FID} = \gamma_{gyr}(B_0 + B_{grad}(x)) \tag{1.2}$$

where the $B_{grad}(x)$ is the magnitude of $\vec{B}_{grad}(x)$ vector.

The proposed system for catheter tracking adopts the same idea. The FID signal around the catheter tip inside the MRI is received by a CMOS IC and downconverted to an electrical current which pass through the MEMS bridges causing them to vibrate under the strong DC magnetic field. However, in this system the IC block containing the receiver and signal processor unit is optically powered up. Also the data will be transmitted optically. In this design, using optical means for power and data transmission will prevent heating problem at the catheter tip. A sample schematic representing the compact form of the proposed catheter module can be seen in Figure 1.1.

1.3. Proposed Readout Method

In this part of the thesis, the design, simulation and fabrication processes of the MEMS devices will be explained. Then their experimental characterization result will be presented briefly.

There are two different generations of MEMS devices studied in this thesis. Each generation of devices contains different geometries of bridges suitable for data readout via optical methods such as laser Doppler vibrometry (LDV) or diffraction grating interferometry (DGI). Using optical methods instead of electrical transmission of the signal as the readout method is one of the promising novelties in this new type optical catheter localization system. Thanks to utilization of the optical readout method, we can eliminate the heating problem at the tip of the catheter which stems from the data transmission through radio frequency (RF) waves.

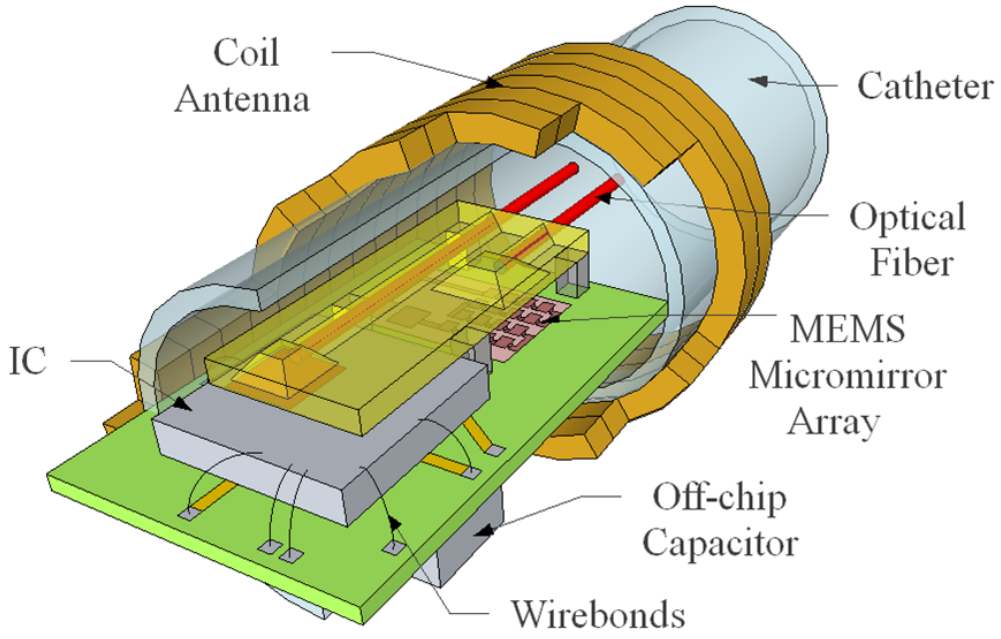


Figure 1.1. Schematic of the proposed catheter system [17].

The detailed explanation for the design, simulation, fabrication and characterization of the MEMS structures will be provided in the following chapters. Briefly, both generations of the devices have similar two-mask fabrication processes, and their structural parts are deposited by nickel electroplating. The basic difference between the first and the second generation of devices is that, the latter allows us to characterize a multiple device-group all together at once whereas the first generation of devices can be characterized only one by one.

In [18], an application of the complementary metal-oxide-semiconductor (CMOS) based catheter tracking system utilizing optical power source and optical data readout methods is explained. Data readout is obtained via a light emitting diode (LED) driven by complementary metal-oxide-semiconductor integrated circuit (CMOS IC) and coupled to fiber optical cable. The intensity of light of an LED is proportional to the current flowing through it. So to get a proper data read out, the LED consumes a high amount of current, on milliampere scale which makes continuous data transition challenging. Therefore, instead of the LED, a novel system utilizing a MEMS resonator

which consumes much lower current (minimum 25 μA) is proposed.

In this novel system, the MEMS resonator, which is a micro-bridge, is integrated with and driven by a CMOS IC. The CMOS IC collects the position data via a receiver from inside of MR bore. This position data is processed and downconverted so that the position data is mapped to a frequency interval. The MEMS resonator resonates due to Lorentz force which is a natural result of current flowing through it under a strong DC magnetic field which is present in MRI machine. The Lorentz force is:

$$\vec{F}_{lorentz} = i \int \vec{dl} \times \vec{B} \tag{1.3}$$

where $\vec{F}_{lorentz}$ the resulting force vector, i is the electrical current flowing through the MEMS bridges, $\vec{dl}$ is the infinitesimal length vector of the bridges and $\vec{B}$ is the DC magnetic field vector.

Since the current can be thought as flowing through a straight line, the cross product with the magnetic field $\vec{B}$ always remains the same. Therefore, the differential equation becomes as Equation 1.3:

$$\vec{F_{lorentz}} = i\vec{l} \times \vec{B} \tag{1.4}$$

where $\vec{l}$ is a vector equal magnitude to the total length of MEMS bridges.

The amplitude of this resonance depends on how well the frequency of the driving current overlaps with the eigenfrequency of the MEMS bridge. The vibration of the MEMS bridge is read out via LDV, which is an optical method that measures the phase shift of the incoming and reflected beam as in Figure 1.2. Also the basic actuation mechanism is given in Figure 1.3.

The very first MEMS devices for this application, which is not in the scope of this thesis, had been fabricated using sputtering. However, sputtering has some limitations. Metals cannot be deposited thicker than half a micron.In addition, sputtering

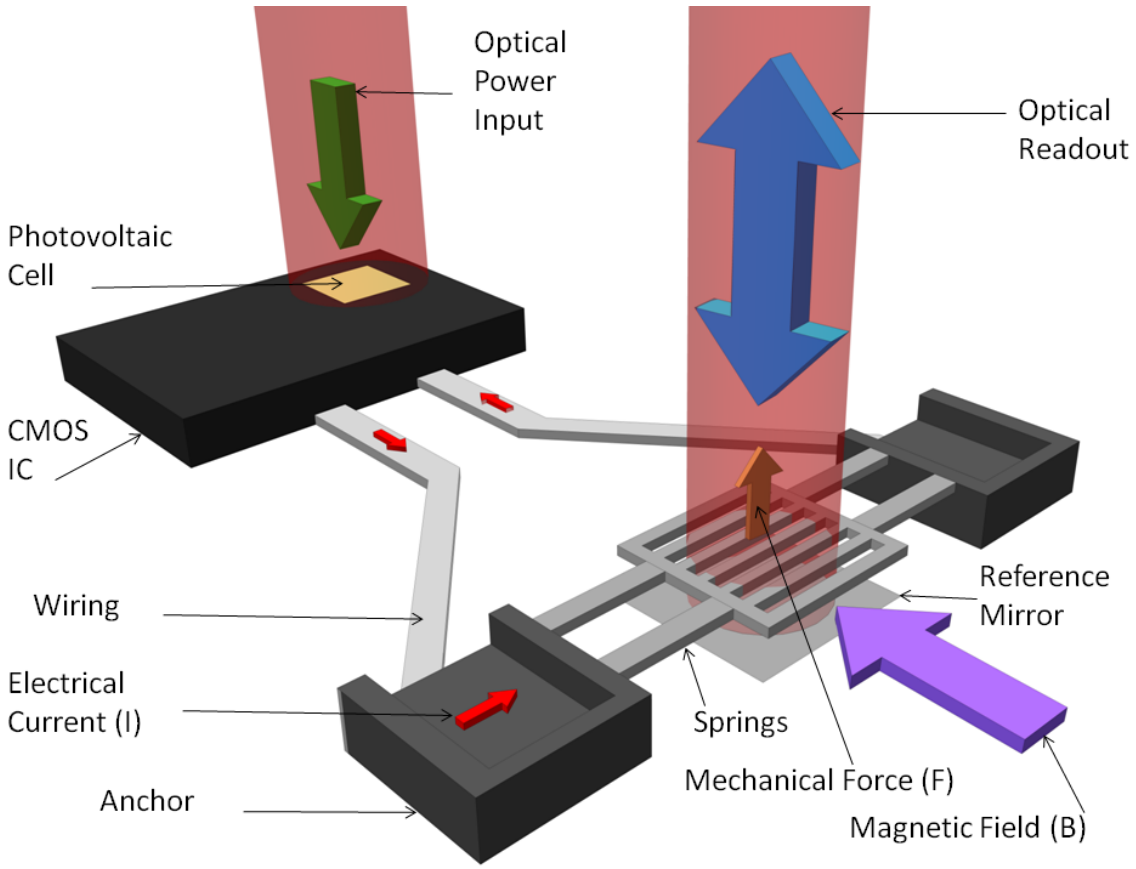


Figure 1.2. Proposed readout method [19].

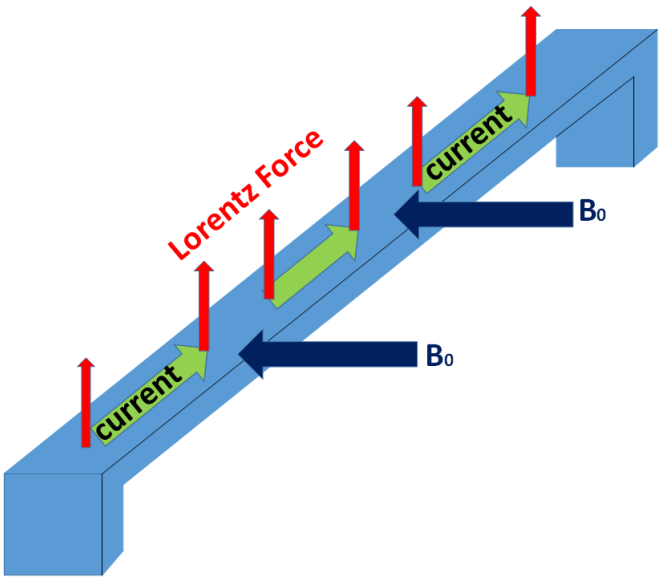


Figure 1.3. Lorentz force acting on the resonator.

process very slow. More importantly, the resulting aluminum devices yield to too much residual tensile stress which limits the lifetime of the devices significantly. Therefore, as an alternative way of metal deposition, nickel electroplating is proposed for the first generation nickel MEMS devices.

Nickel electroplating enables fast, well-polished, stable, ductile and low stress metal deposition. It is very common in industrial applications on macro level. There are some MEMS applications that uses electroplating as a metal deposition way [20,21].

The first generation MEMS devices are designed, simulated, fabricated and characterized. The characterization results showed that electroplating technique gave us, conformal MEMS resonators with residual stress values smaller than 50 MPa even though they have three times higher aspect ratio compared to sputtered devices. The resonators were also tested with the CMOS IC in a hybrid fashion in the lab environment and the fabricated devices are proved to be functional under MRI-imitating conditions. However, the first generation devices are bulky in volume. They are approximately 50 μm wide and 150 μm long. That means only a single device can be characterized by LDV with a beam size of 50 – 60 μm.

A single MEMS bridge can provide us with the data only in a narrow frequency interval which is not enough to map the whole MRI bore. The laser beam size of LDV is the limiting factor on the number of devices that can be characterized – read out. There are two direct ways to overcome this obstacle, which are increasing the LDV beam diameter or shrinking the MEMS module. There are several problems for the first approach. First of all, the size of the catheter should be smaller than 7 french which is approximately equal to 2.2 mm. Therefore, we want the design to be as small as possible. Moreover, to make LDV beam wider, the beam should pass through an optical setup and after that the widened beam should be transmitted to the MEMS module through a fiber optical cable which is a cumbersome work. Therefore, shrinking the MEMS module is accepted as a solution. By a much more compact design with narrower MEMS bridges, obtaining data from multiple devices fitting into LDV laser beam size can be possible. This way, a frequency interval wide enough for imaging

MRI bore can be possible.

The eigenfrequency of a MEMS bridge depends on its geometrical features. The thickness of the devices in the same group cannot be changed practically due to fabrication process. The width of the resonator beam (or bridges) is kept as small as possible because we want to fit as many devices as possible into a small area. However, we can change the length of the resonators to change the resonant frequency. This way, several of these thin beams with different lengths can be placed parallel to each other in a device group. Shrinking the design area, a complete device group with multiple resonators can fit in the LDV beam size.

2. THE FIRST GENERATION MEMS DEVICES

The first generation of MEMS bridges fabricated in this study are clamped-clamped bridge like structures with square masses in the middle. On average, a single device is around 50 μm wide and 150 μm long-including the length of the flexures. The thickness of the device can be changed by changing the plating time; however in this study the devices fabricated are 1.5 μm thick.

2.1. Design and Simulation of First Generation MEMS Bridges

The first generation devices are designed and simulated. The frequency simulation is done in COMSOL Multiphysics while DC displacement simulations are done in SolidWorks.

The devices in this first design can be categorized into two main groups: the ones compatible with LDV and the ones compatible with DGI readout methods. These two types of designs with different flexure varieties count a total of 39 different structures, which were designed, simulated and fabricated for the first generation of devices. The relative dimensions of the devices can be seen on Figure 2.1 and Figure 2.2:

2.1.1. Finite Element Simulations in COMSOL

As it was mentioned, the geometries of the designed bridges vary from device to device. Any difference in these geometrical features results in different eigenfrequency values. That is, the system tends to vibrate at different resonance frequencies at the presence of any driving force due to different geometrical features. A clamped-clamped, beam like structure can have infinitely many modes of resonance with different eigenfrequency values. The first six of the resonance modes with the lowest eigenfrequency values can be seen in Figure 2.3:

LDV measures the phase shift between the incident and reflected laser. This

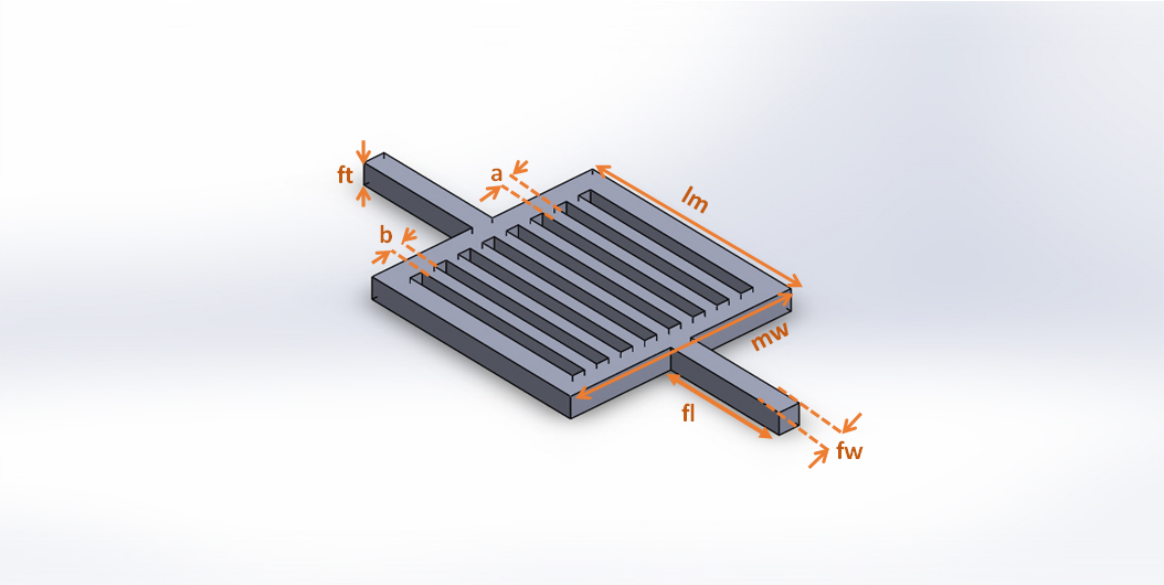


Figure 2.1. First generation single flexure device with diffraction gratings.

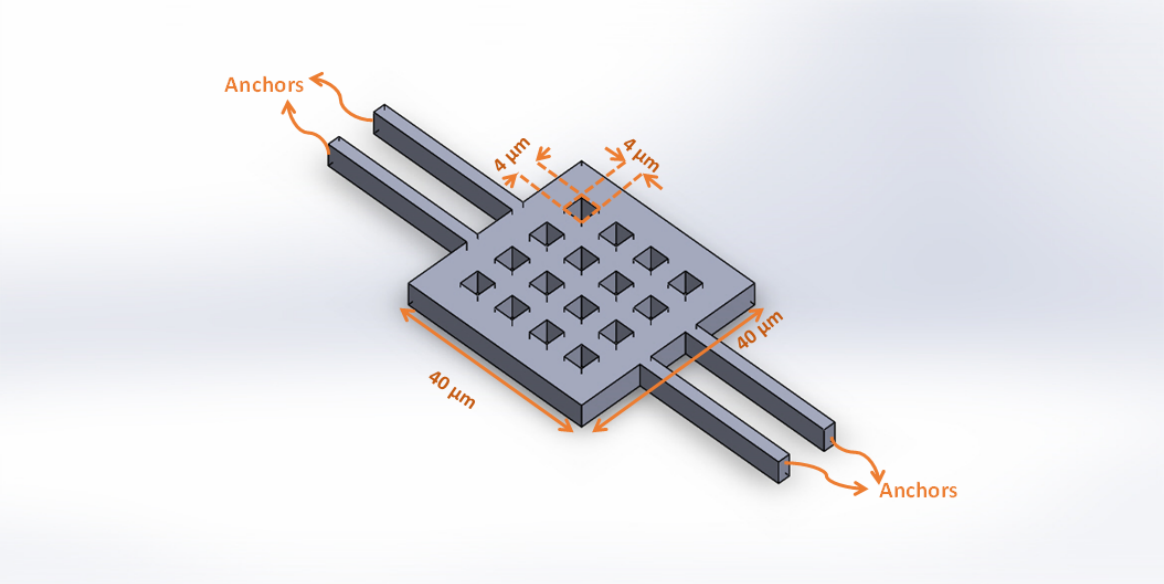


Figure 2.2. First generation double flexure device with perforations.

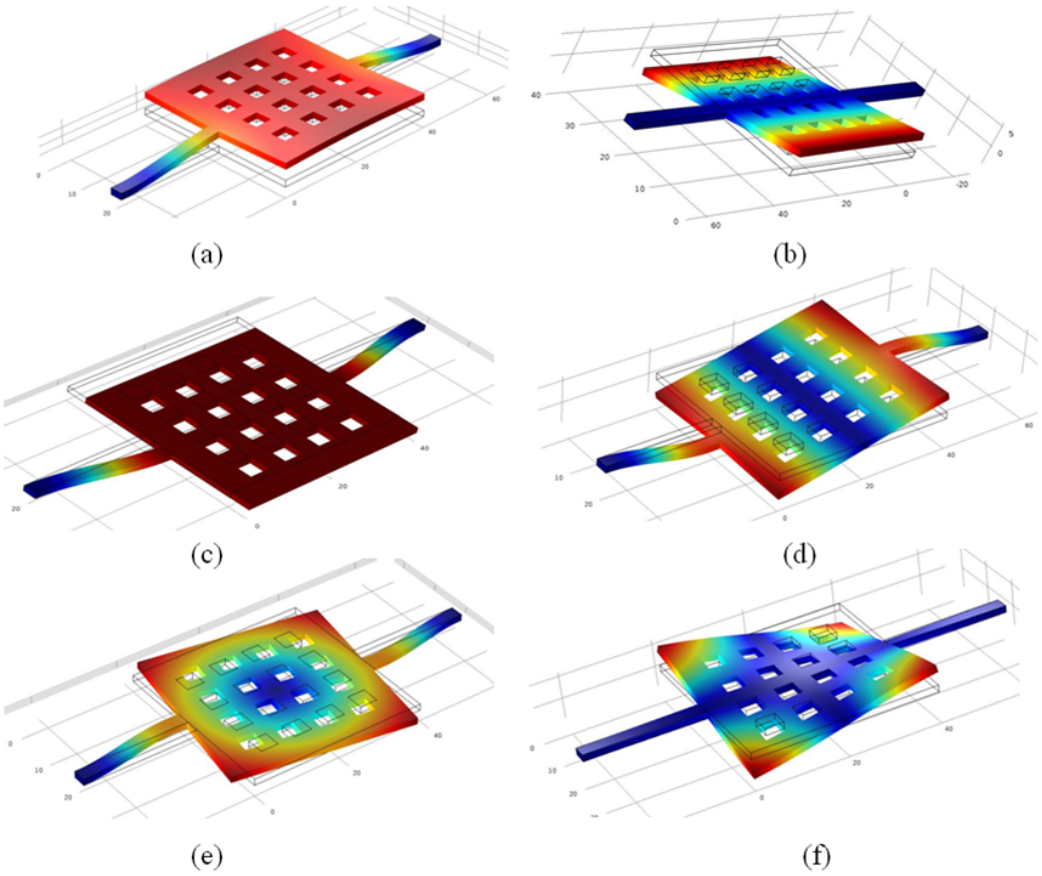


Figure 2.3. Six resonance modes with the lowest resonant frequency: (a) out of plane sliding, (b) torsional, (c) in plane sliding, (d) rocking, (e) Fifth mode, (f) Sixth mode [22].

phase shift data, would be used to generate the resonant frequency information of the resonator. Since LDV will be used as data read out method, only the out of plane bending motions are meaningful.

The designed resonators are drawn in COMSOL Multiphysics 4.3b can be seen in Table 2.1, and the eigenfrequency information about all different structures are recorded for all different resonators in Table 2.2.

2.1.2. Static Displacement Simulations on SolidWorks

The displacement value of a clamped-clamped structure under a DC force only depends on the magnitude of applied force and the spring constant of the beams. Gravitational force due to the weight of the resonator is too small compared to the Lorentz force. Note that the Lorentz force acting here is actually not a DC force, but for simple manual calculation we first calculate the DC force and then it is possible to find resonant displacement by multiplying DC displacement with the quality factor of the device. In that case, the mass has only a fractional contribution on the DC displacement and the amount of deflection from the normal position can be calculated only considering Lorentz force.

However, if we consider the dynamic analysis which should be the case in here, things get complicated because there are viscous damping forces such as squeeze film damping acting on the resonator. If particularly the subject is a micron scale device these damping forces become more important, because the mass scales with the cube of dimension whereas the damping forces scale with the square of the dimension. The dynamic motion can be modelled analytically as in [23–26]; these models can provide correct numerical results if the values of the required physical parameters are known. The general mathematical relation defining the behavior of the structure is given in Equation 2.1

$$m\ddot{\vec{z}} + c_d\dot{\vec{z}} + (k_e + k_0)\vec{z} = \vec{F}_d sin\omega_F t \tag{2.1}$$

Table 2.1. The geometries of all first generation devices [22].

#	Flexure length (lf) (μm)	Flexure width (fw) (μm)	Mirror type	No. of flexures	No. of diffraction gratings	a (μm)	b (μm)
1	60	3	Square perforation	single			
2	60	4	Square perforation	single			
3	60	5	Square perforation	single			
4	60	2.5	Square perforation	double			
5	31	5	Diffraction grating	single	13	2	2
6	41	3	Square perforation	single			
7	45	5	Square perforation	single			
8	45	2.5	Square perforation	double			
9	40	4	Square perforation	single			
10	42	5	Square perforation	single			
11	42	2.5	Square perforation	double			
12	31	5	Diffraction grating	single	9	2.5	2.5
13	30	5	Diffraction grating	single	8	3	3
14	31	2.5	Diffraction grating	double	13	2	2
15	31	2.5	Diffraction grating	double	9	2.5	2.5
16	30	2.5	Diffraction grating	double	8	3	3
17	31	3	Square perforation	single			
18	32	4	Square perforation	single			
19	32	5	Square perforation	single			
20	30	4	Square perforation	single			
21	32	2.5	Square perforation	double			
22	26	3	Square perforation	single			
23	26	5	Square perforation	single			
24	22	3	Square perforation	single			
25	26	2.5	Square perforation	double			
26	23	4	Square perforation	single			
27	22	5	Square perforation	single			
28	20	4	Square perforation	single			
29	22	2.5	Square perforation	double			
30	17	3	Square perforation	single			
31	18	4	Square perforation	single			
32	19	5	Square perforation	single			
33	19	2.5	Square perforation	double			
34	16	5	Square perforation	single			
35	16	2.5	Square perforation	double			
36	14	5	Square perforation	single			
37	14	2.5	Square perforation	double			
38	8	5	Square perforation	single			
39	8	2.5	Square perforation	double			

Table 2.2. Resonant frequencies of all first generation devices in six modes (kHz) [22].

#	Out-of-plane sliding	Torsional	In-plane sliding	Rocking	Fifth mode	Sixth mode
1	145.3314	259.4027	315.6028	558.5339	906.4583	
2	162.0689	309.0468	472.7014	604.7998	1328.482	1705.417
3	175.5509	352.9947	642.1609	638.7496	1770.271	
4	179.8541	345.6389	331.4438	650.0245	1656.175	
5	230.6228	275.6028	1247.32	751.5695		1042.27
6	247.3701	312.805	562.6918	831.2691	1336.357	
7	259.5519	405.215	984.7096	876.4871	2380.536	
8	268.2511	435.0196	514.9958	904.6615	2252.977	
9	280.4099	374.7867	863.895	925.1372	2002.231	2728.286
10	284.0719	419.1313	1088.857	941.2707	2550.575	
11	294.2477	460.9167	571.6544	975.4965	2358.474	
12	295.4036	280.684	1333.39	806.6927		1231.359
13	299.456	268.0261	1370.961	813.1645		1204.998
14	302.76	325.9562	692.3347	839.0237	1170.112	993.4972
15	318.372	387.9143	736.6966	887.0552	1350.585	1212.559
16	325.2901	379.2323	760.6488	909.9569	1335.875	1146.922
17	350.1807	355.6479	841.2231	1074.387	1756.648	2720.031
18	370.87	416.5154	1192.806	1146.5	2501.148	2748.431
19	398.5034	476.239	1604.281	1228.484	3334.676	2782.63
20	400.2823	428.3348	1305.564	1215.025	2662.869	2755.275
21	417.4727	585.0265	858.9821	1298.988	2687.231	
22	431.8806	385.8103	1083.067	1261.978	2101.278	2733.262
23	505.752	524.3942	2132.888	1484.212		2812.044
24	520.6342	417.4381	1371.99	1463.839	2496.187	2748.558
25	535.2988	708.1773	1166.012	1601.155	2911.221	0
26	540.5338	487.1274	1891.14	1542.103	3475.081	2786.795
27	603.719	566.2739	2661.427	1712.919		2839.438
28	624.1549	513.5266	2282.462	1734.394	3993.708	2802.09
29	645.1921	828.1289	1485.481	1884.649	3106.152	4242.288
30	675.945	469.6288	1957.399	1817.702	3269.137	2775.84
31	691.0468	539.3952	2621.412	1887.74		2818.686
32	696.975	605.1348	3206.407	1928.125		2866.086
33	751.7567	949.5484	1828.656	2165.124	3298.726	4300.473
34	812.4118	648.8028	3956.553	2190.562		2898.216
35	886.9523	1109.271	2324.411	2532.643	3557.319	4350.921
36	905.8627	686.9474	4615.928	2403.883		2928.62
37	997.7527	1245.543	2788.365	2845.575	3785.687	4385.133
38	1288.923	865.0445		3223.61		3090.299
39	1480.039	1880.972	5644.026	4334.893	4981.23	4543.915

where m is the mass, $\vec{z}$ is the out of plane displacement vector, k_e is the elastic spring constant (which is associated with damping), k_0 is the spring constant of the mechanical structure, c_d is the damping coefficient, $\vec{F}_d$ is the driving force vector and ω_F is the angular frequency of the driving force.

The displacement simulation of the resonator is therefore very complex, because to simulate the displacement for a particular resonance mode, one has to determine the values of the first and the second damping factors, which are k_e and c_d in this case, that will characterize the resonance amplitude. However, making a healthy estimation for these damping factors is not an easy work. Therefore, the two types of resonators are drawn and only the displacement of the resonators under a constant force is simulated in SolidWorks. The simulated types are single flexure-resonator with gratings and the double flexure-resonator with perforations which can be seen in Figure 2.4 and in Figure 2.5.

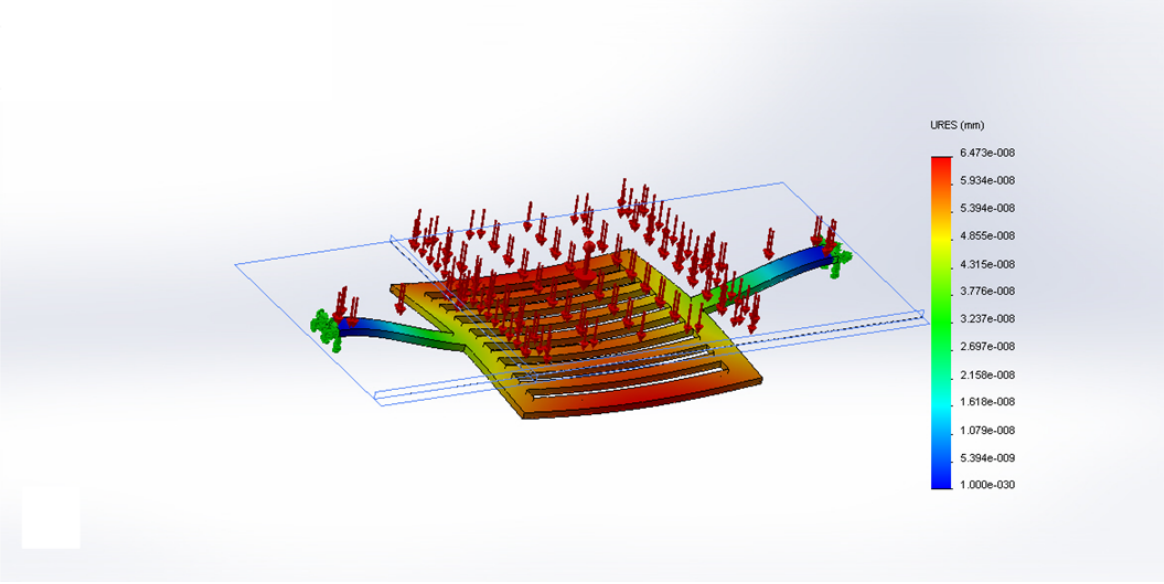


Figure 2.4. Displacement simulation of a diffraction grated device under a DC force.

By these displacement simulations, it is aimed to get crude information about the magnitude of out of plane deflection. This simulation is important because we need to understand: (i) whether the height margin beneath a resonator is enough to operate freely without hitting the bottom substrate, (ii) whether current amplification

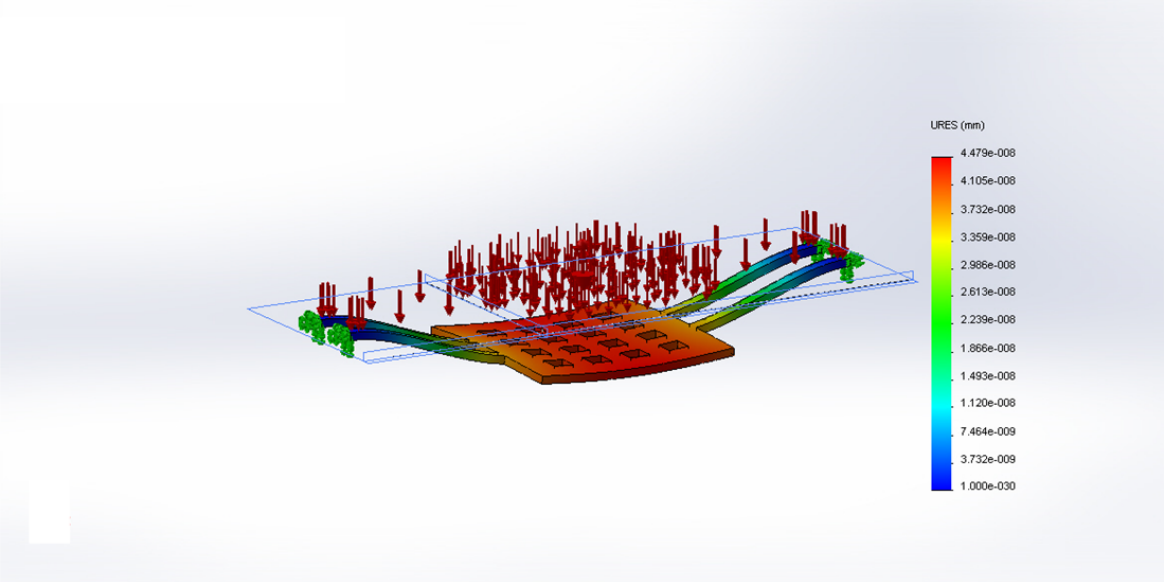


Figure 2.5. Displacement simulations of a MEMS resonator with a perforated mass under a DC force.

is necessary to actuate the resonator, (iii) whether the device thickness is enough to give the resonator enough strength. In any case, it is better, but if air gaps below the devices are as high as possible, because as the air film thickness beneath the structure increases the effect of damping due to thin film squeezing decreases.

To have an idea of the deflections of the resonators under a real MRI, the magnetic field is entered as 3 T and it is always assumed to be perpendicular to the direction of current propagation. The force is distributed over the whole resonator surface, that is the pressure values are hand calculated and force per area value is applied. Note that the pressure value on the mass is not the same as the pressure value on flexures. The current is distributed over a larger surface in the mass part, which results in a lower pressure value. Simulations showed that the amplitude of the deflection is on the Angstrom level. Here note that in Figure 2.4 and Figure 2.5, displacements are given in 10^{-7} mm scale. In some cases to actuate the devices, we will need current amplification to get a detectable resonance peak. This will be necessary also since we use 0.62 T magnetic field during the experiment, not 3 T.

2.2. Fabrication Process

The fabrication process of the first generation devices was explained in detail in [22] together with possible causes of failures and in the end, obtaining of the optimal fabrication recipe. This process consists of six steps. These six steps are two masked lithography, one sputtering, one nickel electroplating and a two-step releasing processes. In the first lithography process, the anchor places are built. On the first layer of photoresist (PR), first a very thin layer of titanium then 10 to 12 times thicker copper is sputtered. In the second lithography, the patterns for the bridges are built. Then in electroplating part, these patterns and the anchor places are plated with nickel. In releasing process, firstly the sacrificial layer is removed with acetone and propanol then the sputtered copper layer is etched away.

2.2.1. The First Lithography

A standard, 4 inches, p-type silicon wafer is coated with TI Prime in spin coater with 4000 rpm for 40 seconds. Then the sample is baked on 120 °C hotplate for 120 seconds. After letting the TI Prime coated wafer cool down for a few minutes, it is spin-coated with 3.2 μm thick AZ4533 photoresist with 6000 rpm for 50 seconds. After that, the sample is soft baked on 110 °C hotplate for 50 seconds then, left again to cool down. Using the first mask, which determines the position of the anchors, the sample is exposed to UV with a dose of 100 mJ/cm^2 and a total exposure of 110 mJ/cm^2. Finally, the sample is developed in 1:4 diluted AZ400K developer for 90 seconds and then hard baked on 120 °C hotplate for 180 seconds.

2.2.2. Sputtering

In order to electroplate nickel we need a conductive plating base. Initially, the substrate is coated with a 10 nm thick layer of titanium to increase the adhesion of the surface; then on top of it 120 nm of copper is coated with sputtering.

It is important to optimize both titanium and copper thicknesses. Increasing the

titanium thickness will give us a better adhesion to the sample whereas increasing the copper thickness is necessary for a better conductance of the surface. Also, one should be aware that these two metals have different thermal expansion coefficients. If the ratio of Cu/Ti thicknesses is not chosen well, during the baking processes in the second lithography cracks can happen in the copper layer. The cracks are not desired since they decrease the conductivity of the surface, which results in a bad electroplating in the end.

2.2.3. The Second Lithography

The second mask that determines the position of the resonators was designed as a clear field mask, which means an image reversal process is necessary. Therefore, AZ5214E is used as a negative photoresist. Since the adhesion of AZ5214E to copper layer is good enough so that there was no need for an additional adhesion promoter layer. AZ5214E is spin-coated with 6000 rpm for 50 second on the sample and then soft baked at 110 °C on the hotplate for 50 seconds. After leaving the sample to cool down for nearly 10 minutes, using the second mask, the sample is exposed to UV with a dose of 40 mJ/cm^2. Then the sample is baked at 120 °C hotplate for 120 seconds. After baking the sample, a second UV exposure takes place without using the mask. The dose of unmasked UV exposure is 250 mJ/cm^2. At the end of second photolithography, the sample is developed in a developer solution, which is 1:4 diluted with deionized (DI) water, for 60 seconds and then hard baked at 120 °C for 120 seconds.

AZ5214E is not as viscous as AZ4533 photoresist, so it cannot be spin-coated thicker than 2 μm. Moreover, since the process is image reversal, the slope of the side-walls (after the lithography) is negative. This negative slope does not allow electro-plating nickel thicker than 1.5 μm. This is one of the drawbacks of the first generation devices.

2.2.4. Nickel Electroplating

The detailed explanation about the plating bath set up will be provided in the fabrication process of the new generation resonators.It suffices to say that, the electroplating setup and plating bath solution is prepared and characterized. The optimum current density is found to be 0.01 A/cm^2. By electroplating, a low-stress, conformal 1.5 μm thick nickel layer is deposited on the conductive locations of the sample.

2.2.5. Releasing the Structures

Releasing the structures is realized in two steps. In the first step the sacrificial layer is removed and in the second step the sputtered metal layers beneath nickel should be etched away. With the help of oxygen plasma and aceton and propanol wet etching we can remove both of the sacrificial layers. However, to remove Ti and Cu seed layers, nickel compatible metal etchants are required. Therefore, we have prepared a nickel compatible copper etchant solution. The solution consists of 1:1:18 glacial acetic acid: 30% hydrogen peroxide: DI water, respectively. The prepared etchant solution is very selective on copper; it etches away the copper very fast whereas the nickel layer remains safe. During this process, the very thin titanium layer is also lifted off. The fabricated devices can be seen in Figure 2.6 and Figure 2.7.

The whole fabrication recipe of the first generation resonators can be found in Table 2.3.

The process is optimized under a set of conditions with certain devices and chemicals at one time, may not provide us the same devices in another time. Most probably, the process will give us close results; but one should know that any fabrication attempt is unique on its own. The process which was optimized to result in 3.2 μm PR thickness with a certain rotation speed and a certain development time, can result in 2.9 μm when it is repeated another time. Therefore, a microfabrication process should be optimized for every different attempt.

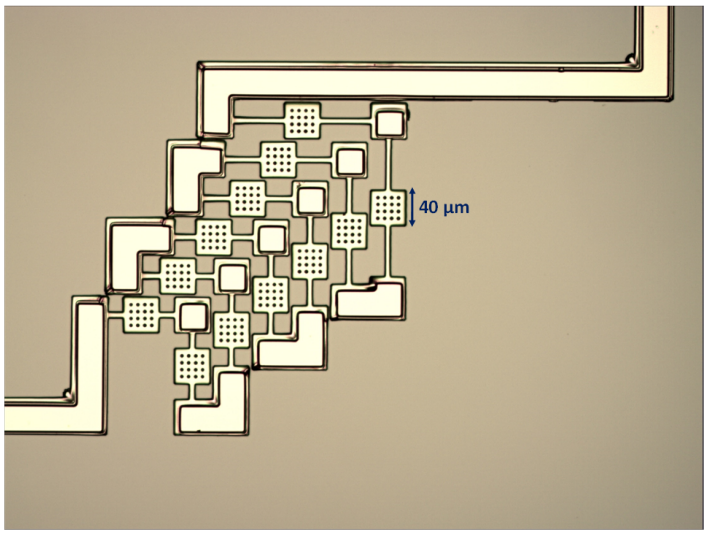


Figure 2.6. Photograph of the fabricated device taken by optical microscopy [22].

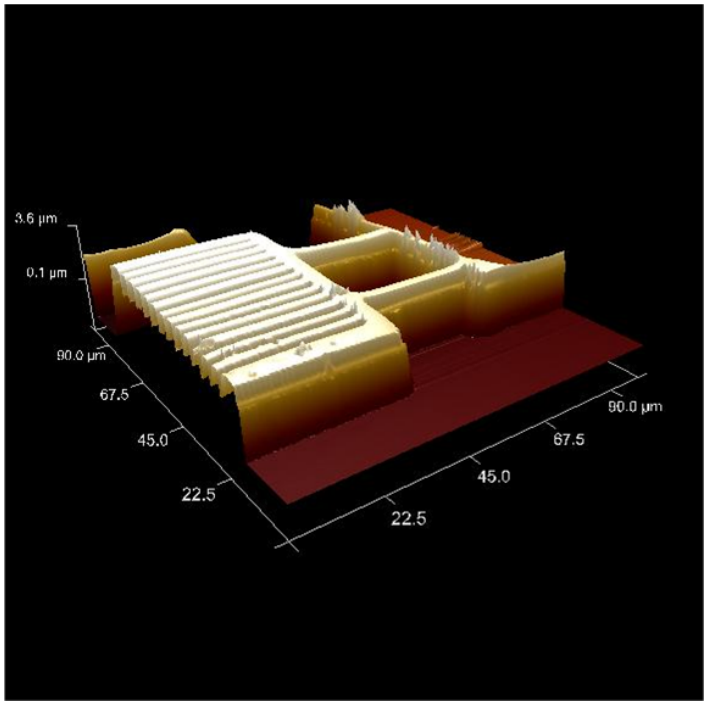


Figure 2.7. Photograph of fabricated devices taken with AFM [27].

Table 2.3. The complete recipe for the first generation devices [22].

FIRST LITHOGRAPHY		AZ4533
TI prime spin coating	4000 rpm	40 seconds
Baking	120 °C	120 seconds
PR coating	600 rpm	50 seconds
Soft baking	110 °C	50 seconds
Delay	wait	10 minutes
Exposure	100 mJ/cm^2	soft contact
Development	AZ400K 1:4 diluted	90 seconds
Post bake	120 °C	180 seconds
SPUTTERING		
Ti thickness		10 nm
Cu thickness		120 nm
SECOND LITHOGRAPHY		AZ5214E
PR coating	6000 rpm	50 seconds
Soft baking	110 °C	50 seconds
Delay	wait	10 minutes
Exposure	40 mJ/cm^2	hard contact
Delay	wait	10 minutes
Image reversal baking	120 °C	120 seconds
UV flood exposure	250 mJ/cm^2	Flood exposure
Development	AZ400K 1:4 diluted	60 seconds
Oxygen plasma	Power = 200 W	180 seconds
Hard bake	120 °C	120 seconds
ELECTROPLATING		
Ni electroplating		10 minutes
	J = 0.001 A/cm^2	1.5 μm Ni
RELEASING		
Wet releasing	Aceton-Propanol	2 minutes each
Ultrasonic	Level 3	3 minutes
Copper etchant		5 seconds

2.3. Measurements and Outcomes

The fabricated MEMS devices resonate under the strong DC magnetic field which is present in MRI machine. To imitate the strong magnetic field inside an MRI machine in the lab environment, two magnets were used. To keep these strong magnets separate from each other a magnet holder was designed in SolidWorks 2013 and fabricated by a 3D printer. The magnet holder is also necessary to keep the magnetic field lines between the magnets mostly linear.

The separation between the magnets is exactly 1 inch. The magnetic field just in the midpoint of the separation of the magnets is measured as 0.62 T by a gaussmeter. Therefore, the strength of the magnetic field provided by the magnets is around five times lower compared for a conventional 3 T MRI system. Since the Lorentz force is depending on the cross product of magnetic field and the length of the conductive line that the current flows through, the resulting force would be five times lower. Therefore, to exert the same amount of force to the resonators, the current flowing through the devices is amplified in some cases during characterization.

For the characterization setup a 3D stage is mounted on the optical table in our lab. Then the holder that keeps the magnets in position is mounted on 3D stage. The fabricated MEMS resonators are placed carefully in the middle of magnets. A precision positioner, probe station is used to make electrical contact with the MEMS devices. There are two types of laser beam in the setup. The green laser beam is used for getting a magnified view of MEMS devices, so that we can observe whether the probes are in the right position. The red laser beam, on the other hand, belongs to LDV device by which we measure the resonance frequency. Figure 2.8 shows the setup prepared for the characterization of the first generation resonators.

The characterization is done in two stages. In the first stage, the driving current is supplied directly from an external current source. In Figure 2.9, a sample measurement result belonging to a double flexure diffraction grated resonator with the dimensions of $a = 3$ μm, $b = 3$ μm, $t = 1.5$ μm, $fw = 2.5$ μm, $lf = 31$ μm, $mw = 55$ μm, $lm = 60$

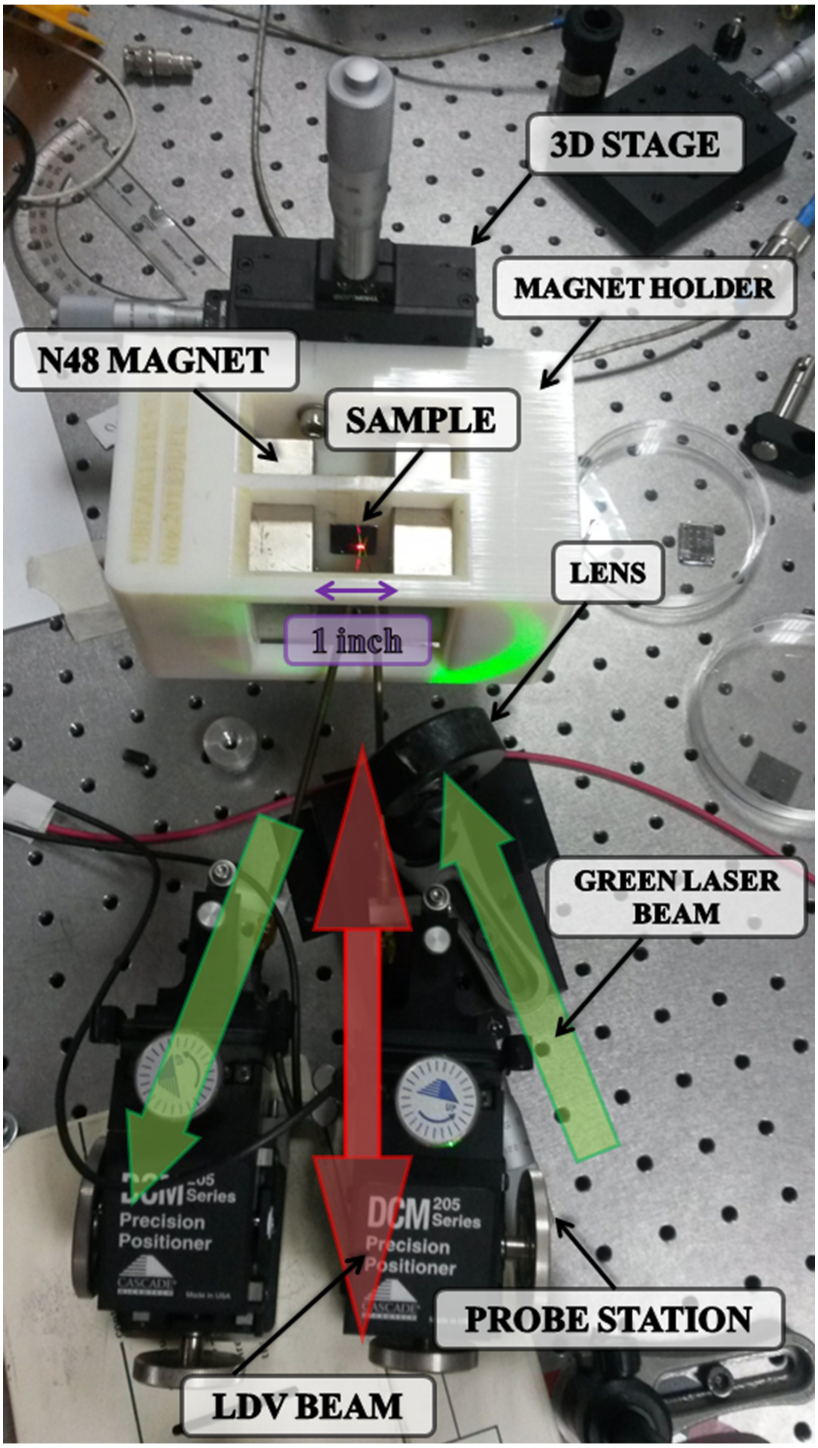


Figure 2.8. Characterization setup prepared for the first generation devices [28].

μm and number of gratings = 8. In Figure 2.1 corresposding geometrical features can be seen. The COMSOL simulation for this device gave 325 kHz out of plane bending resonant frequency and 379 kHz torsional mode resonant frequency.

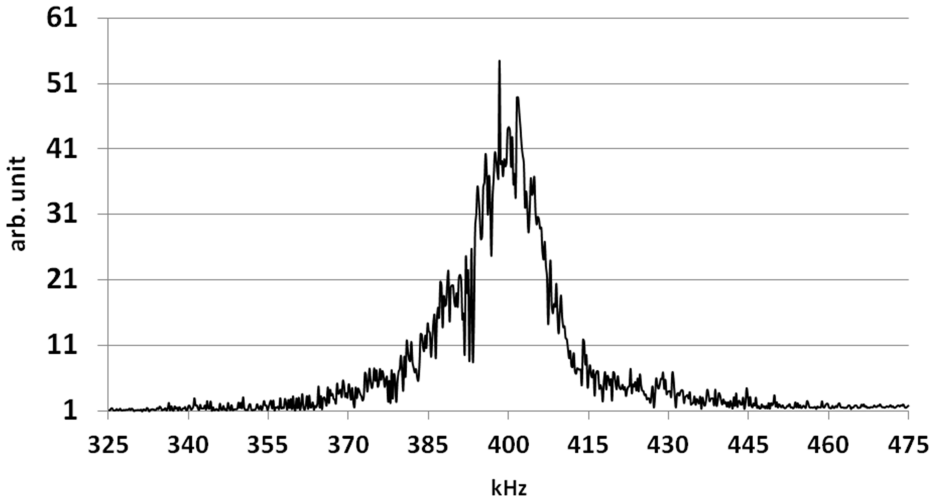


Figure 2.9. The displacement measurement of an externally driven resonator [27].

The measured value for the resonant frequency is 385 kHz. Using the model in [29] and [30] the difference between the theoretical and experimental values of the out of plane sliding resonance frequency can provide us with the information about the stress that the structure has. For this purpose, Equation 2.2 is used:

$$\omega_s^2 = \frac{(2\pi)^4}{3}\left(\frac{El}{\rho A}\right)\frac{1}{l^4} + \frac{(2\pi)^2}{3}\left(\frac{\sigma}{\rho}\right)\frac{1}{l^2} \tag{2.2}$$

where ω_s is the measured resonant frequency rad/sec of the stressed beam, E is the Young's Modulus of nickel, I is the moment of inertia for the out of plane sliding motion of the clamped-clamped resonator, ρ is the density of nickel, A is the cross sectional area, l is the total length of the beam and σ is the residual stress. The moment of inertia for the out of plane sliding motion of the clamped-clamped resonator can be found using Equaton 2.3.

$$I = \frac{4}{3}(fw)(t)^3 \tag{2.3}$$

where fw is the half of the flexure width, t is the half of the flexure thickness.

Using Equations 2.2 and 2.3, the calculated value of the residual stress of the resonator is 45.4 MPa. In [31], the stress value for the 0.5 μm aluminum sputtered devices fabricated for the same purpose is calculated as 685 MPa. Electroplated resonator has 15 times lower residual stress than the aluminum sputtered resonator even though the nickel resonator is three times thicker.

In the second stage, the current is supplied by a CMOS IC which converts the laser power to electrical current via a triple well photodiode structure on it [32]. The laser used for powering up the CMOS IC is COHERENT CUBE660-75 FP. Laser beam is transmitted through a coupled fiber with 62.5 μm diameter to the butt-coupled IC. As it can be seen in Figure 2.10, the butt-coupling is realized with the help of 1 cm unit cube fabricated in 3D printer. There is a hole opened through the cube in which the fiber optical cable end is placed. After finding the optimum position by try and error, the fiber cable end position is fixed by epoxy. The relative loss in power due to this hand made coupling is 3.1 %.

Several different devices with different resonant frequencies are characterized and the results in Figure 2.11 are obtained. For some of the devices the current is amplified to actuate the resonator bridges. The numerical values are shown in Table 2.4, where f_{meas} is the measured resonant frequency and f_{sim} is the simulated resonant frequency. Note that in Table 2.4, the resonators are designated with the numbers corresponding to the peaks from left to right in Figure 2.11.

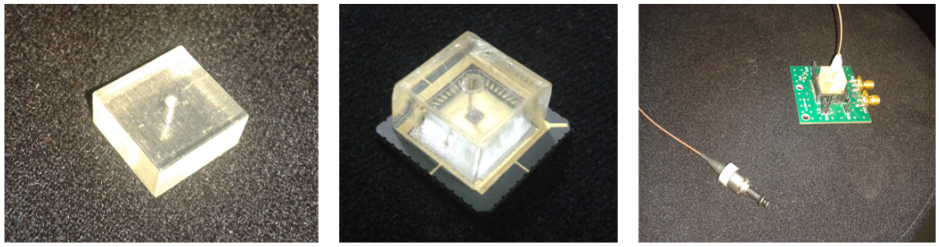


Figure 2.10. Fiber butt-coupling on CMOS IC via a plexyglass cube [28].

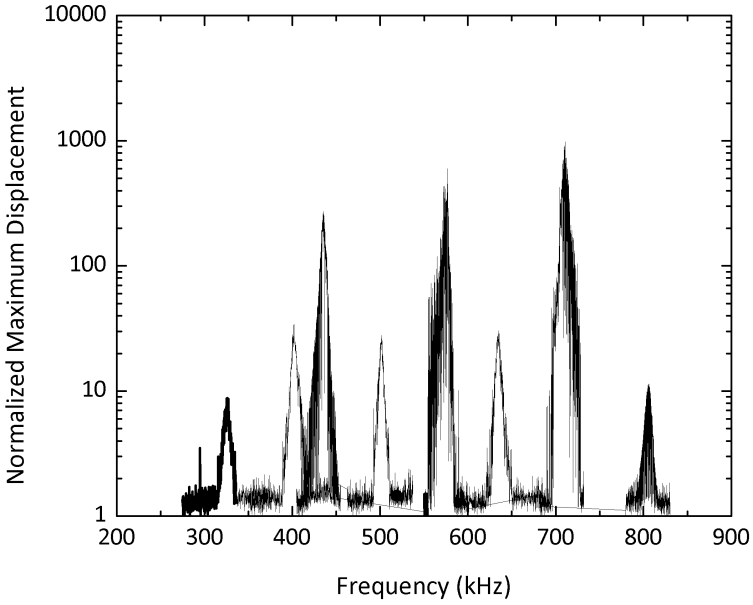


Figure 2.11. Eight-device group driven by the CMOS IC characterization result [19].

Table 2.4. The measured and simulated resonance characteristics of eight-device group [19].

Resonator No	1	2	3	4	5	6	7	8
f_{sim} (kHz)	268	325	417	431	535	624	645	751
f_{meas}(kHz)	325	402	435	502	575	635	710	805
Error percentage	21.3	23.7	4.3	16.5	7.5	1.8	10	7.2
Quality factor	35	77.3	87.1	143.4	192	127	88.7	115
Actuation current (μA rms)	25	3800	360	250	4500	3800	4500	4500
Number of flexures	2	1	2	1	2	1	2	2

With this second measurement, it is shown that the proposed catheter setup is functional under an actual MRI environment.

All in all, this part demonstrated us that electroplating is a cost and time effective metal deposition technique. It enabled rapid and conformal metal deposition and fabrication of the structures with much higher aspect ratio compared to sputtering. With the first generation nickel electroplated devices, it is shown that devices with much lower residual stress are fabricated by electroplating.

On the other hand; using negative photoresist in the second lithography limited the metal deposition thickness. In the case of the first generation nickel electroplated devices, the nickel layer thickness is 1.5 μm. More importantly, in this design, the devices can only be characterized one by one, since the LDV laser beam size cannot cover more than a single device. A single device is not enough to cover the frequency interval necessary for magnetic resonance imaging applications. Particularly to eliminate the second obstacle a new design is necessary.

3. THE SECOND GENERATION MEMS DEVICES

This part explains the ongoing process of the design and fabrication of the second generation nickel electroplated MEMS resonators. As it was mentioned in the previous sections, the second generation of nickel devices was designed in order to eliminate the weak points of the first design. In this new design, we wanted to augment our previous design in terms of two main points: The first point is to eliminate the limit on the device thickness by eliminating the image reversal process in the previous design. The second point, which is the basic factor that pushed us for a new design, is that we need to cover a wider frequency interval for MRI applications.

In [18], which explains the study on a previous attempt on catheter tracking system with LED data readout part, the chosen gradient interval is 150 – 450 kHz with a center frequency at 300 kHz. The MEMS modules should be designed to respond the need of a same amount of frequency interval. As it is mentioned in Chapter 1, the frequency interval is used to map the whole diameter of MRI bore. We can assume that the proximity of bore border will be irrelevant in cardiovascular surgery and use 200 kHz interval with the same gradient value. Also, it is known that the MRI system itself is less accurate at the borders [33, 34].

In an MRI, the position of the microcoil receiver of the catheter can be calculated using the frequency of the output signal as in Equation 3.1:

$$\Delta x = \frac{f_x - (f_{isocenter} - f_{ref})}{\gamma_{gyr} G_x} \tag{3.1}$$

where Δx is the distance of the micro-coil from the isocenter of the MRI bore, f_x is the center frequency of the received output signal, f_{ref} is the frequency of the reference RF pulse, $f_{isocenter}$ is the resonance frequency corresponding to the isocenter, and G_x is the strength of the gradient field applied in the x-axis.

Therefore for a 0.7 m diameter MRI bore and for 7.05 mT/m G_x in Equation 3.2

$$f_{isocenter} - f_{ref} = 0.7\gamma_{gyr}G_x \tag{3.2}$$

the frequency interval necessary to map the MRI bore is found as 210.11256 kHz. If G_x is increased, the required interval will also increase so that the imaging resolution will increase. If G_x is arranged to a lower value, we need a narrower frequency interval for imaging. However, using narrower frequency interval will cost us a worse imaging resolution. Therefore, $f_{isocenter}$ as well as the bandwidth can be freely assigned. However, there are boundary limits for these values.

If the center frequency is chosen too low, the gradient signal can behave like MRI signal and excite the molecules which is an undesired situation. The receiver cut off frequency of the CMOS IC is around 1.1 – 1.2 MHz and it determines the upper boundary for the frequency interval that can be chosen. Therefore, any frequency interval greater than 200 kHz and remaining in between 100 kHz and 1 MHz was assumed to be safe and functional.

3.1. Design and Simulation of Second Generation MEMS Bridges

There are basically two types of resonators in the second generation design. The first type is the beam-shaped resonator which is a straight line without a mass in middle Figure 3.1 and Figure 3.2. The second type resonator has a mass with perforations in between two flexures located in each side of the mass. Different from the first deign there are no resonators with double flexure on each side.

3.1.1. Finite Element Simulations in COMSOL

The first type resonators are all drawn and simulated in COMSOL Multiphysics by sweeping the length, the width and the thickness of the structure. The same procedure was followed for the second type resonator by changing the geometrical dimensions of the flexure and device thickness. For each resonator type and device

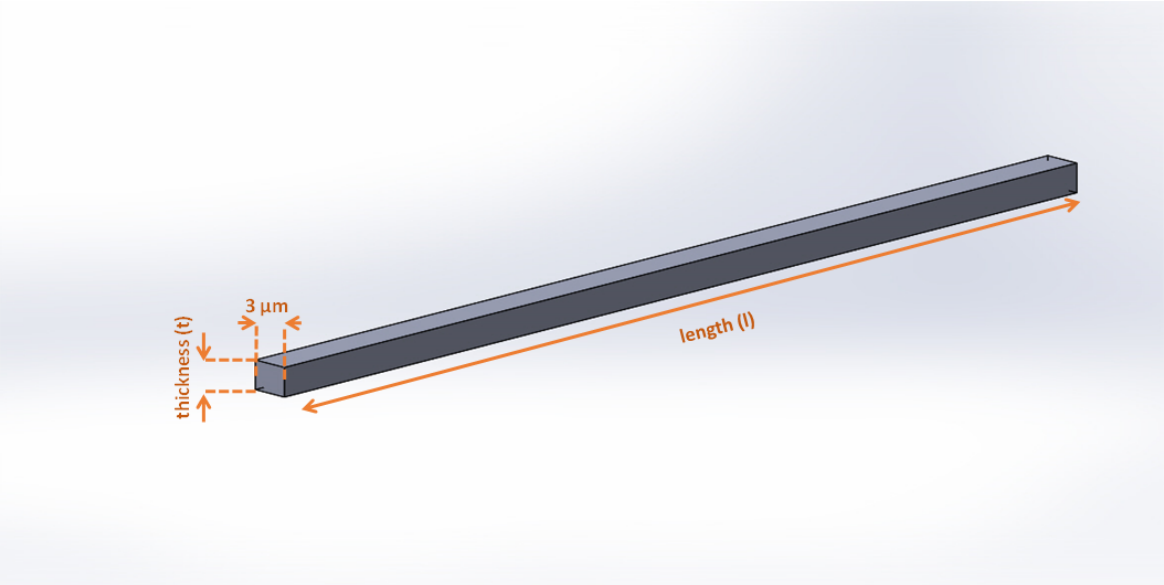


Figure 3.1. Second generation beam type device.

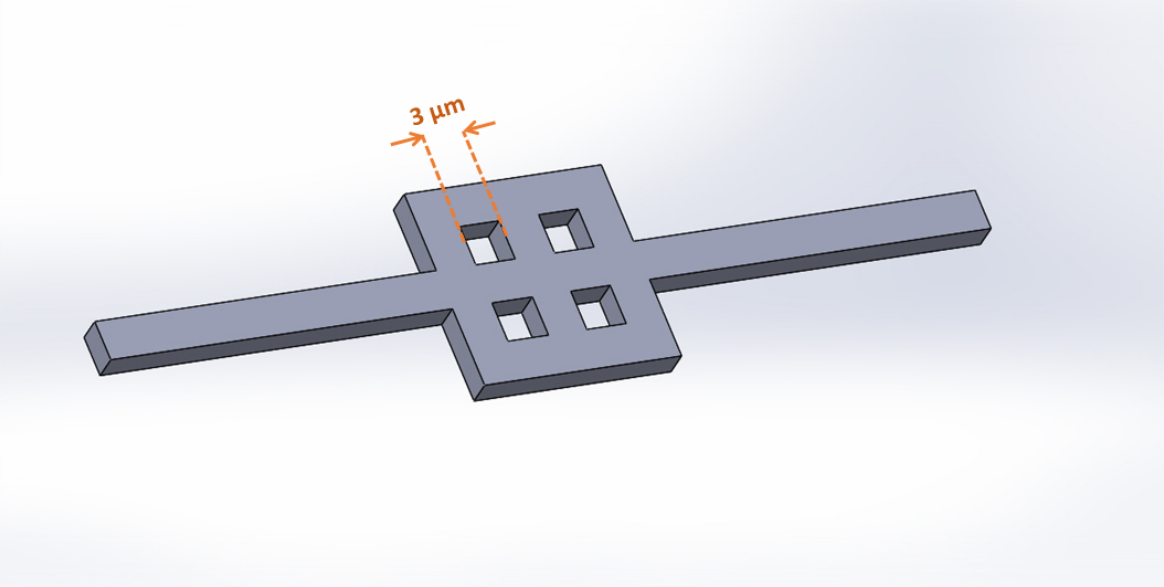


Figure 3.2. Second generation resonator with perforated mass.

thickness groups containing several resonators with different lengths are formed. In each group, each device was chosen such that their out of plane bending resonant frequencies divide the desired frequency interval of the group into equal pieces. Desired frequency interval, in this case, should be greater than 200 kHz. For most groups the frequency interval is arranged greater than 300 kHz.

In the previous design all the devices were 1.5 μm thick and that thickness provided enough strength for the resonator to not to stick to the substrate during releasing. Considering the mass of the second generation resonators is much smaller compared the mass of the first generation resonators, sticking during releasing will not be a problem. 1.5 μm devices were also ductile enough to endure the stress. However, since we want to observe also the effect of device thickness, we decided on three different device thicknesses: 0.5 μm, 1 μm and 1.5 μm. The beam thicknesses are chosen as 1 μm and 1.5 μm and thicknesses for the devices with the mass are 0.5 μm and 1 μm. All these device groups are placed on the same substrate. It is not a problem in terms of electroplating, because prior to the plating process the wafer is diced. Dicing the sample is also necessary to filter out the electrolyte to prevent possible particles from reaching the cathode surface. In all pieces, there is only a single type of device groups. That means each piece can be electroplated independently. However, if it is necessary, the chance to electroplate thicker nickel layer is still exist contrary to the first generation devices. If a thicker layer is electroplated the resonant frequency of all devices in a group will just shift to higher frequencies, because the spring constant increases as the device thickness increases. Choosing width is also another important aspect of the design. Since we want to maximize the number of devices that can fit into 50 μm LDV beam diameter, the width should be chosen as small as possible. However, if the width is chosen to be too small, the fabrication of the devices will be very problematic. Moreover, too small widths will adversely affect the strength of the device. Therefore, the beam (and flexure) widths are chosen as 3 μm and even that width is a possibly problematic choice for the fabrication. The only variable left to arrange the frequency is the beam (or flexure) length. By changing the length of the devices which are identical in width and thickness, six different device groups are

formed. Each device group covers a frequency interval greater than 200 kHz.

The simulation results of arranged groups which is designated by G1 through G6 can be seen in Table 3.1 through Table 3.3. G1 and G3 groups consists of 10 beam type devices with thicknesses 1 μm and 1.5 μm, respectively. These two groups provide approximately 300 kHz frequency interval. G4 and G5 groups consists of five beam type devices again with the thicknesses 1 μm and 1.5 μm, respectively. Since there are less devices in this group, the frequency interval of this group is 200 kHz. Finally, in G3 and G6 groups there are five resonators with mass in the middle with respective thicknesses of 0.5 μm and 1 μm.

Table 3.1. 10-beam type device groups.

G1 (thickness = 1 μm)		G2 (thickness = 1.5 μm)	
length (μm)	resonant frequency (kHz)	length (μm)	resonant frequency (kHz)
95	567	105	695
100	512	109	649
105	464	113	607
110	423	117	562
115	387	121	521
120	355	125	490
125	327	129	463
130	302	133	442
135	280	137	411
140	260	140	391
Δf (kHz) = 260 - 567		Δf (kHz) = 391 - 695	

The measurement method is kept to be the same as the first generation, that is the measurement by using LDV. Therefore, again only the out of plane bending motion and rocking modes are meaningful for data readout. Since the rocking mode resonance is at much higher frequencies than out of plane mode resonance it may not

Table 3.2. Five-beam type device groups.

G4 (thickness = 1 μm)		G5 (thickness = 1.5 μm)	
length (μm)	resonant frequency (kHz)	length (μm)	resonant frequency (kHz)
100	511	115	579
108	540	123	508
115	387	130	453
123	341	138	403
130	302	145	364
Δf (kHz) = 302 - 511		Δf (kHz) = 364 - 579	

Table 3.3. Groups with four resonators with perforated mass.

G3 (thickness = 0.5 μm)		G6 (thickness = 1 μm)	
length (μm)	resonant frequency (kHz)	length (μm)	resonant frequency (kHz)
63	100	95	100
41	200	63	200
31.5	300	49	300
26	397	41	400
Δf (kHz) = 100 - 397		Δf (kHz) = 100 - 400	

be considered during characterization and data readout. Moreover, since this time the devices are very narrow torsional motion of the MEMS bridges will not be important in data readout.

3.1.2. Static Displacement Simulations on SolidWorks

As in the case of the first generation devices, the static displacement of the selected resonators is simulated in SolidWorks 2013. However, this time the simulation is done for all devices. Force is applied uniformly as force per unit area which is the maximum pressure due to Lorentz force. In simulation of the resonator with masses which can be seen in Figure 3.3, since the current travels through a larger area in mass part the pressure here is calculated separately. Another important point is that, since the mass can be important in this type of devices, the gravitational force is also taken into account. However, it has only a minor contribution to the deflection magnitude as the simulation results showed.

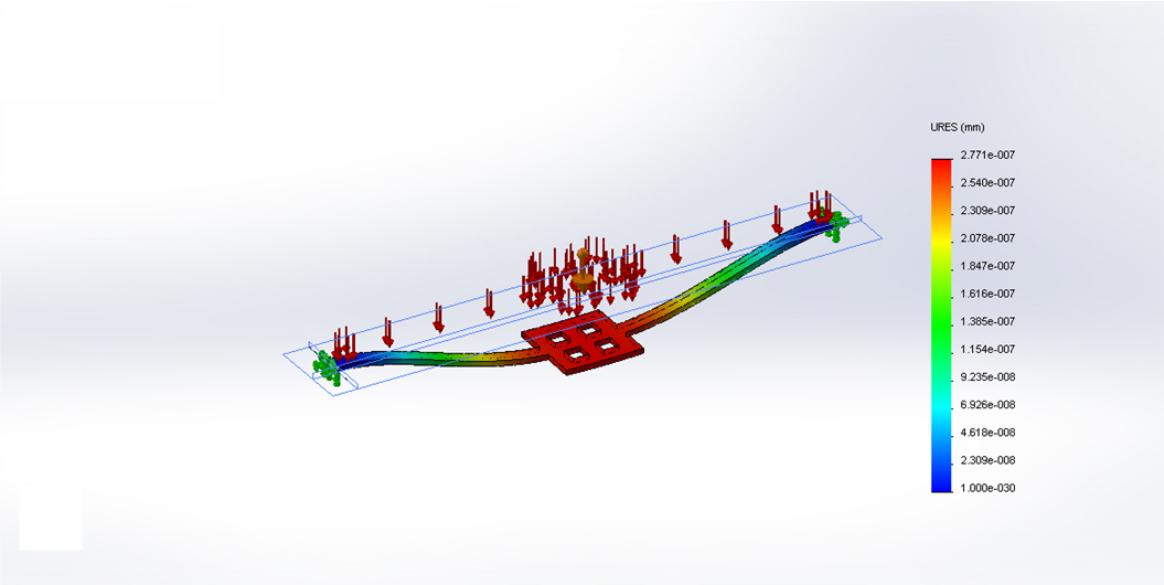


Figure 3.3. Displacement of a second generation resonator with a mass under a DC force.

Table 3.4 through Table 3.6 demostrates the simulated values for the new resonators under a consant DC force. Compared to the first generation devices, the second

generation MEMS devices bend more under the same working conditions. Even though the exerted Lorentz force per unit length is the same for both generations, since the second generation devices are much narrower, they are exposed to greater values of pressure which is the Lorentz force per unit area of the MEMS bridge.

Table 3.4. DC displacement for the devices in G1 and G2 groups.

G1 (thickness = 1 μm)		G2 (thickness = 1.5 μm)	
length (μm)	Δz_{max} ($10^{-7}\times$mm)	length (μm)	Δz_{max} ($10^{-7}\times$mm)
95	3.012	105	1.335
100	3.697	109	1.55
105	4.494	113	1.791
110	5.415	117	2.058
115	6.47	121	2.355
120	6.762	125	2.682
125	9.035	129	3.041
130	10.57	133	3.438
135	12.29	137	3.869
140	14.22	140	4.22

Table 3.5. DC displacement for the devices in G4 and G5 groups.

G4 (thickness = 1 μm)		G5 (thickness = 1.5 μm)	
length (μm)	Δz_{max} ($10^{-7}\times$mm)	length (μm)	Δz_{max} ($10^{-7}\times$mm)
100	3.012	115	1.921
108	5.032	123	2.515
115	6.47	130	3.138
123	8.471	138	3.985
130	10.57	145	4.855

Table 3.6. DC displacement for the devices in G3 and G6 groups.

G3 (thickness = 0.5 μm)		G6 (thickness = 1 μm)	
length (μm)	Δz_{max} ($10^{-7}\times$mm)	length (μm)	Δz_{max} ($10^{-7}\times$mm)
63	103.4	95	60.49
41	21.87	63	13.05
31,5	8.759	49	5.225
26	4.61	41	2.771

3.1.3. Mask Design of Second Generation Devices

After the simulations, the two masks required for the fabrication process of the devices was drawn in L-Edit. In the first design, since only one device is characterized in one time, we need only a pair of contact pads. The current can flow through the resonator passing through the contacts, which are the probe station tips. In the second generation design we want to characterize a group of resonators simultaneously. To make taking contacts easier, the contact region is maximized. To actuate all devices simultaneously, all resonators in a group should be series connected. When the current flows from one probe to the other, it would be flowing through all devices. To make the resonators series connected, the anchors of the bridges should be electrically isolated from each other. It can be seen that the anchors are separated from each other in the Figure 3.4 through Figure 3.7.

3.2. Fabrication Process

The fabrication process of the second generation MEMS resonators are similar to the fabrication process of the first generation devices except that for the second generation devices AZ4533 positive PR is used as photoresist and chromium used as the adhesion promoter. AZ4533 is chosen because it can be deposited up to 4.7 μm thickness which is at least twice thicker compared to the maximum possible thickness

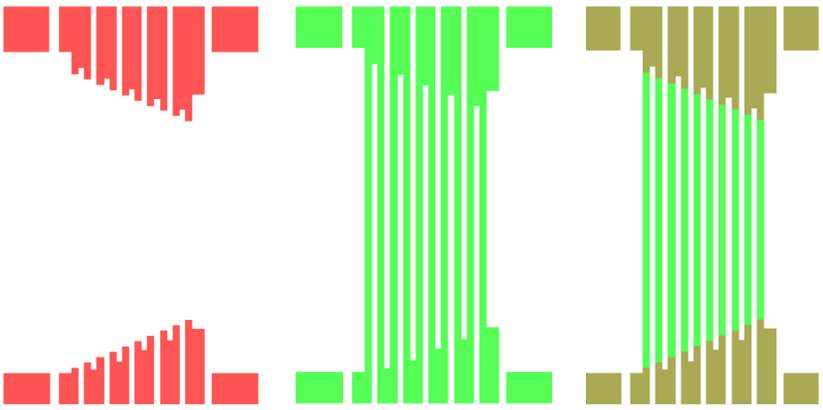


Figure 3.4. Second generation devices mask for 10-device beam type group.

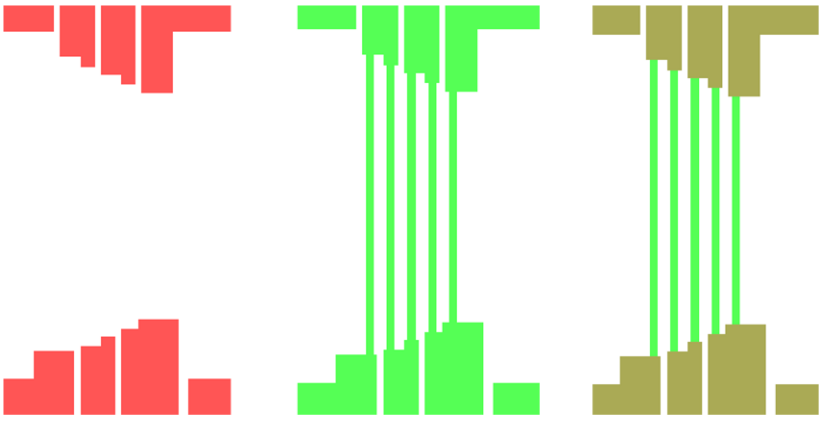


Figure 3.5. Second generation devices mask for five-device beam type group.

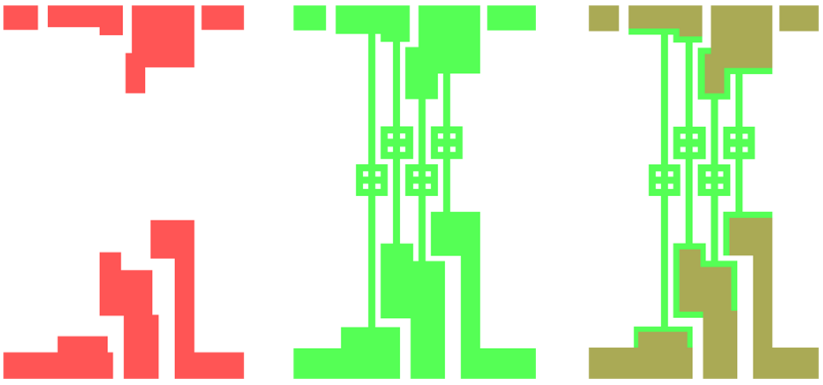


Figure 3.6. Second generation devices mask for four-device group with masses.

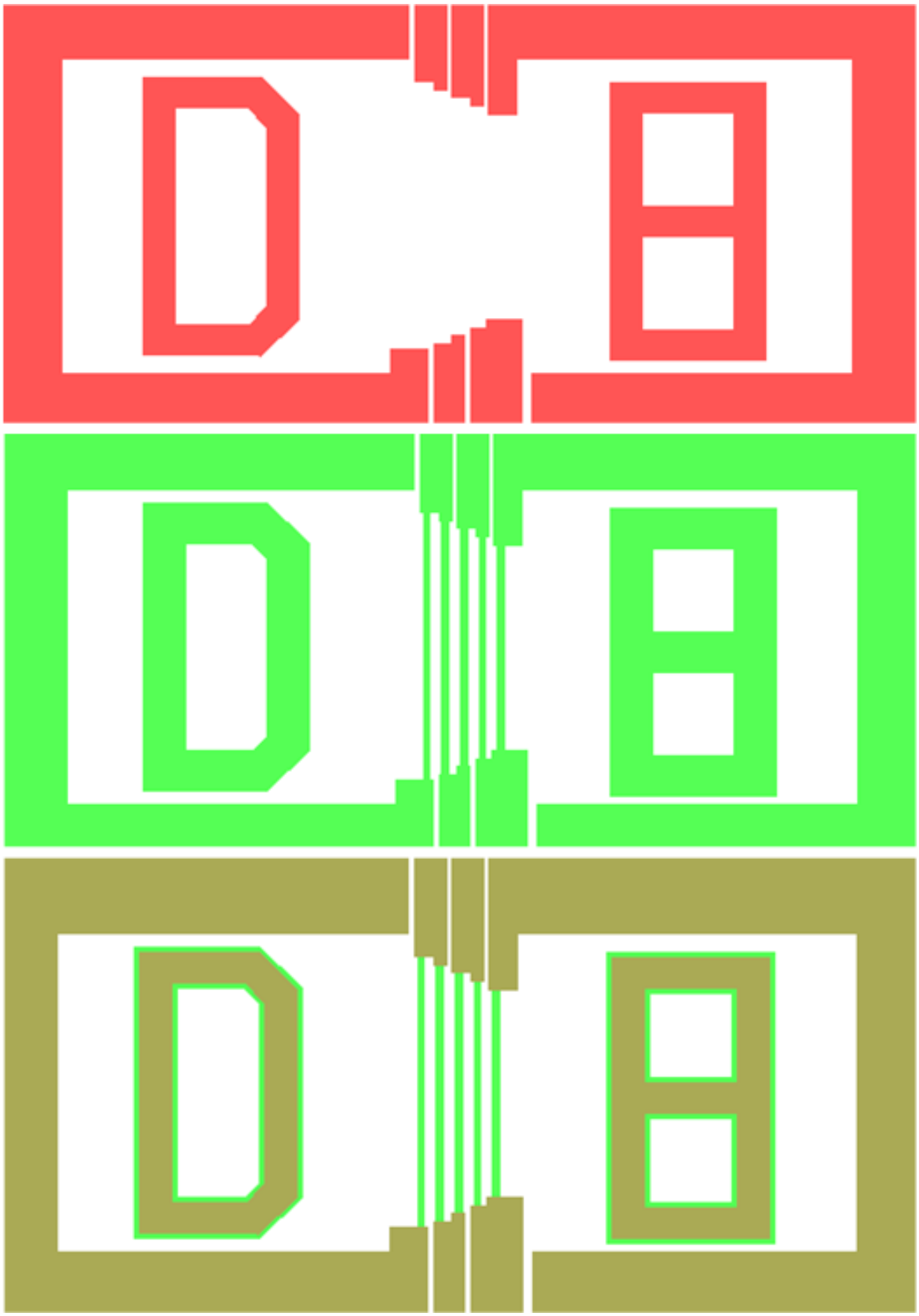


Figure 3.7. Series connected resonators in a five-device beam type group.

of AZ5214E negative photoresist which is used in the fabrication of first generation devices. The proposed fabrication method for the second gneration devices can be seen in Figure 3.8.

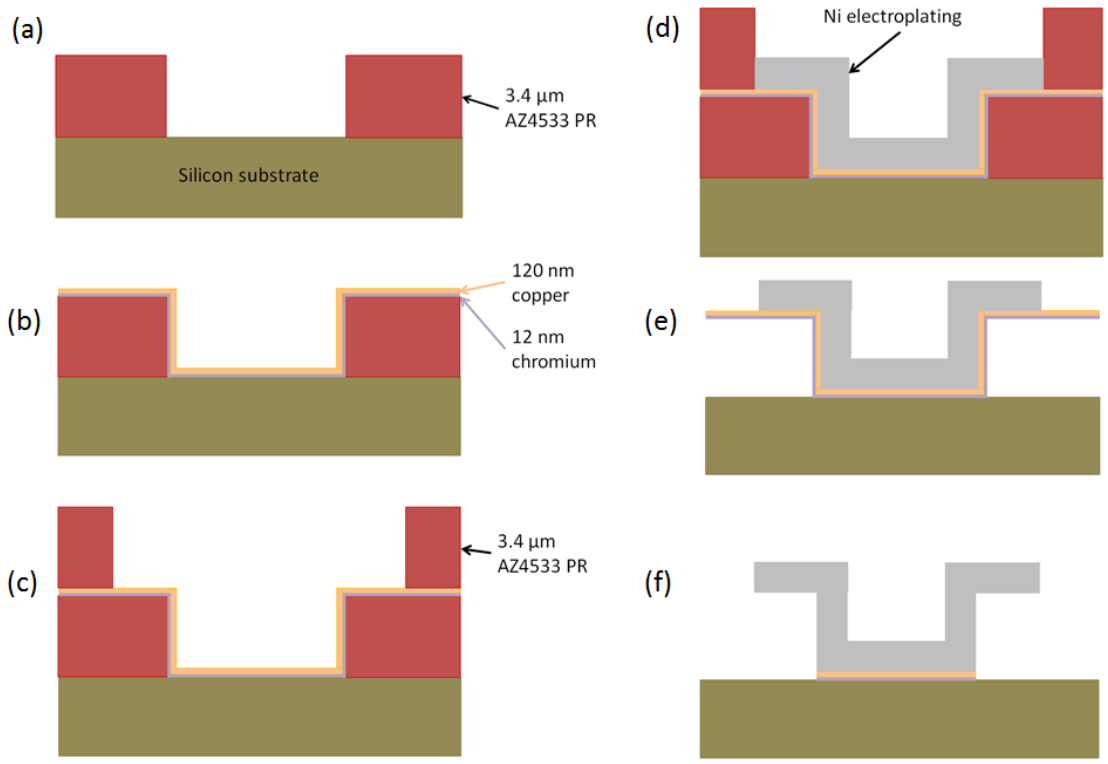


Figure 3.8. The proposed fabrication method for the second generation MEMS resonators: (a) first lithography, (b) sputtering, (c) second lithography, (d) electroplating, (e) releasing, (f) wet etching.

The fabrication of the second generation resonators is an ongoing process; it is not completed successfully yet, due to several reasons. In this part, the fabrication study will be explained together with successful and unsuccessful attempts step by step.

3.2.1. The First Lithography

In the first lithography, we want to determine the positions of the anchors. Also, the height of the resonator from the surface of the silicon substrate will be determined by the thickness of the photoresist that will be spin-coated. Therefore, the first lithography step is of essential importance for the next fabrication steps. If the height is not enough, the beams can stick to the substrate surface during wet releasing.

Firstly, TI Prime is spin coated on a p-type silicon substrate with 4000 rpm spin speed for 40 seconds. The TI Prime coated sample is baked on a 120 °C hotplate for 120 seconds and left for 5 minutes to cool down. Then AZ4533 photoresist (PR) is spin coated on the sample with 5000 rpm for 50 seconds and soft baked on 100 °C hotplate for 50 seconds. The reader should be careful here. According to the datasheet of AZ4533 photoresist this coating speed and temperature values should give us 3 μm thick PR layer. However, it certainly depends on lab humidity, spin coater calibration and the photoresist itself etc. In this case, the PR thickness is around 3.4 μm. The reason for this can be that the AZ4533 in the cleanroom is outdated. Even though it is outdated, it can be used as a sacrificial layer as long as it sticks to the substrate and the coating is conformal. However, the experimenter should measure the thickness of the PR layer by a profilometer to be sure about the PR layer thickness.

Using the first mask in soft contact, the sample is exposed to UV with 100 mJ/cm^2 exposure dose and 1200 mJ/cm^2 total exposure. During UV exposure, nitrogen gas is formed in the photoresist. We wait for nearly ten minutes to let the sample release this nitrogen gas to preveent bubbling during any thermal heating process. After UV exposure the sample is ready for development. The sample is developed in AZ400K developer (1:4 diluted with DI water) for 85 seconds and then it is immersed into DI water and dried. Two micrographs taken from an optical microscope can be seen in Figure 3.9.

The optimization of the recipe for this step is very hard. The tiny nosings that the beams will be placed on can be eroded if UV exposure or the development time

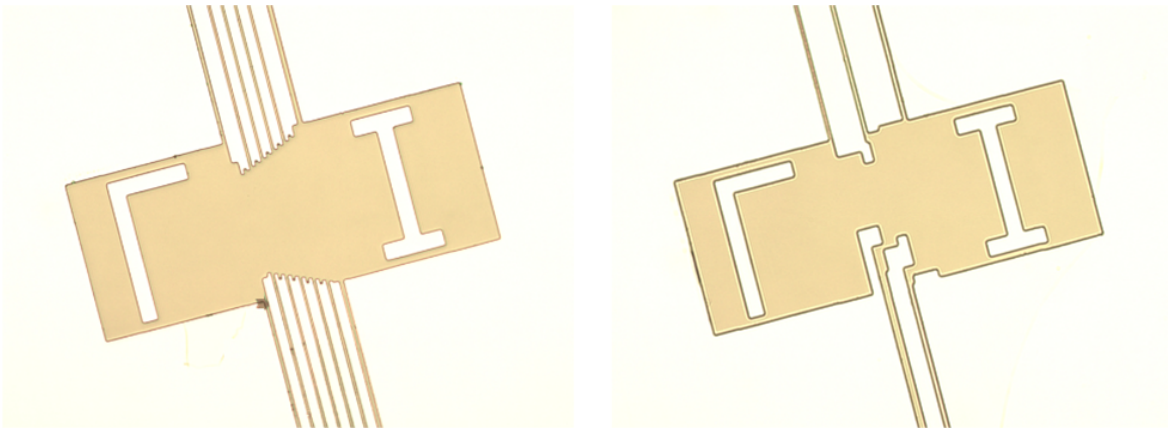


Figure 3.9. Micrograph of the second generation devices after the first lithography.

is higher than optimum. Also the tiny photoresist barriers that isolate the anchor lines from each other face the same threat. If the continuity of this barrier is gone or its height is not enough for the desired thickness of electroplating, anchors will be electrically shorted in the end. If there is an electrical short between the anchors, the current will not flow through the devices connected to those anchors.

3.2.1.1. Mask Aligner Calibration. The first lithography was a problematic process for a long time. The structures on the wafer were not proper and the amount of deformation was following a pattern from left of the substrate to its right which can be seen in Figure 3.10. That is an indicator of bad alignment which is caused by either the tilt of the mask or the substrate. Since they are not parallel to each other, UV exposure is not precise. This problem is solved by cleaning the parts of mask holder and substrate tray and recalibration of the mask aligner, EVG620.

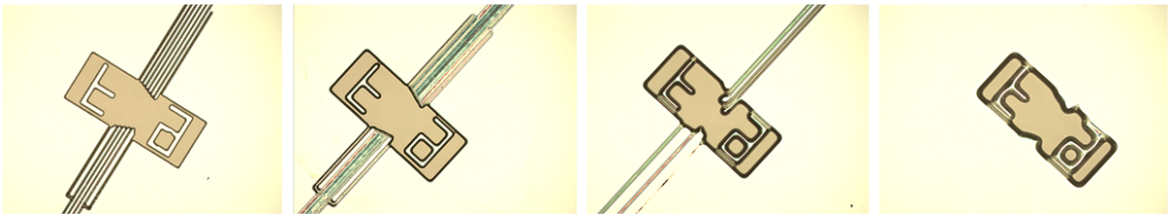


Figure 3.10. Mismatch problem in mask alignment prior to calibration.

3.2.2. Sputtering

Electroplating can be done on the conductive surfaces. However, the choice of metal for the plating base is also important [35]. A metal can only be electroplated on a plating base only if the plating base is more electronegative than the metal itself. The order of metals can be seen in Table 3.7.

Table 3.7. Activity series for metals.

1- Lithium	10- nickel
2- Potassium	11- tin
3- calcium	12- lead
4- sodium	13- hydrogen
5- magnesium	14- copper
6- aluminum	15- mercury
7- zinc	16- silver
8- chromium	17- platinum
9- iron	18- gold

During the fabrication of the first generation MEMS resonators, we observed that the nickel electroplating on chromium plating base is not efficient. However, when nickel was plated on gold or copper, it worked well. Gold or copper plating bases also has very good conductivity even though they are not thicker than 120 nm. The lack of nickel compatible gold etchant at the moment eliminated the gold plating base option. On the other hand, the nickel compatible copper etchant solution can be prepared in lab environment with the chemicals in hand. The prepared solution is very selective on copper. Therefore, copper is decided as plating base.

To increase the adhesion of copper, a very thin (around 12 nm) titanium layer is sputtered before copper layer. However, experiments showed that the adhesion of copper to chromium is better than adhesion to titanium. The difference in linear

expansion coefficient is larger between copper and chromium. That is also another important factor, because due to different thermal expansion, cracks may occur on copper layer which will decrease the conductivity of the plating base. However, a better adhesion can compensate this difference. Figure 3.11 shows the pictures of sputtered sample.

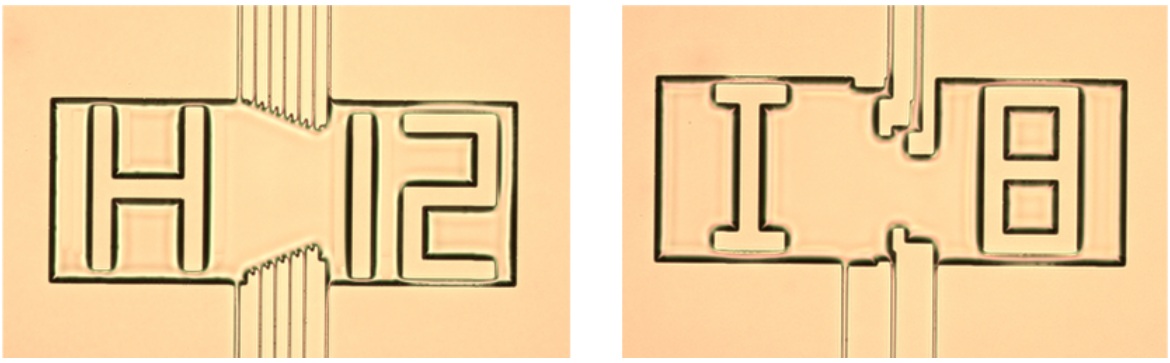


Figure 3.11. Chromium-copper sputtered sample.

3.2.3. The Second Lithography

Eliminating the image reversal process for the second lithography enabled using a positive PR, in this case AZ4533. AZ4533 is a more viscous photoresist compared to AZ5214E. AZ5214E can be coated maximum up to 2μm which limits the device thickness. Also in negative photolithography process, the sidewalls have negative slope, which again limits the device thickness and plating efficiency.

The second lithography process is the same as the first lithography except we do not coat with TI prime since adhesion is good this time. AZ4533 photoresist is spin coated on Cr and Cu sputtered sample with 5000 rpm spin speed for 50 seconds as it was in the first lithography. The coating thickness is measured to be 3.4 μm. The sample is baked on the 100 °C hotplate for 50 seconds. Then the sample is left to cool down for 10 minutes. By waiting we also let the photoresist to absorb enough humidity from the lab environment which is necessary to prevent cracks on PR layer. AZ4533 PR coated sample is exposed to UV light with a dose of 100 mJ/cm^2 and a total exposure of 1200 mJ/cm^2. Then we let the sample to release the nitrogen gas

formed inside the substrate during the exposure. Finally, in a 1:4 diluted AZ400K developer, the sample is developed for 85 seconds with small agitations, washed with DI water and dried. Now the sample is ready for electroplating. The photograph of the sample after the second lithography can be seen in Figure 3.12.

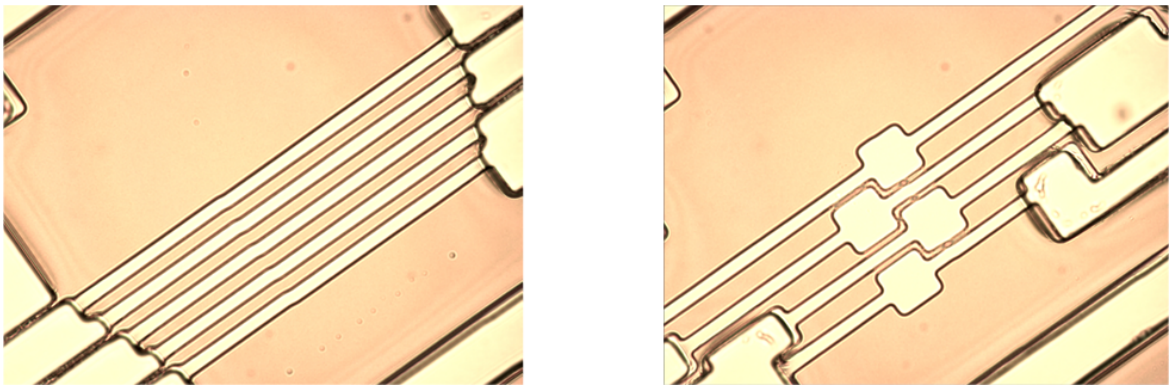


Figure 3.12. The photograph of second generation resonators taken by optical microscope after the second lithography.

3.2.4. Nickel Electroplating

Electroplating is a fast, cheap and easy way of thick metal deposition. It is widely used for nickel, zinc, gold, silver and copper metals coating, particularly in industrial applications. Even though there are exceptions, it is not used in microelectronic fabrication as much as in industry, probably due to the more precise knowledge is required for the thickness of the material in microelectronics. However, once the plating bath is characterized the plating thickness can be estimated correctly since the plating thickness is linear with plating time. Electroplating gives us a more ductile, conformal and polished nickel deposition. The nickel devices fabricated with electroplating have much lower tensile stress though their aspect ratio is much higher.

3.2.4.1. Theoretical Background. Electroplating process has a relatively easy theoretical background. There is an anode and a cathode inside an appropriate liquid media which is called as electrolyte. The anode is the metal that we will plate with; in this case it is a nickel ingot. The cathode is the surface that the metal will be plated

on. The liquid media is a conductive solution specified for the anode metal. When a current supply is connected to anode and cathode, due to this conductive solution the current flows from the anode to the cathode with the help of oxidized metal ions leaving the anode surface. The oxidized metal ions travel through the liquid media and when they reach the cathode, they are reduced and stacked on the cathode surface (see Figure 3.13). The speed of process is determined by the amount of current driving the setup. The electroplating process is therefore perfectly linear with time albeit there are some points that can affect the efficiency.

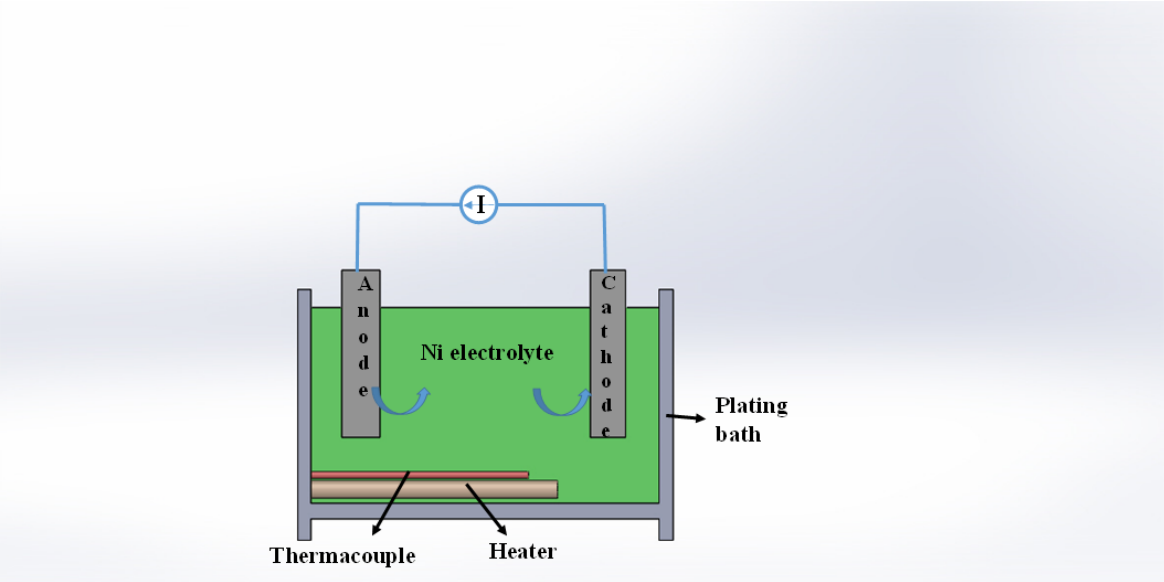


Figure 3.13. The schematic of a sample nickel electroplating bath.

First of all, the water molecules and other polar molecules inside the electrolyte behave like dipoles. They are attracted by the positive metal ions on the cathode and form a very thin layer of water (or other aqueous molecules) on the cathode. This layer is called as cathode diffusion layer. As the cathode diffusion layer gets thicker, it gets harder for the metal ions coming from the anode to reach the cathode surface. Therefore, to increase plating efficiency, the cathode diffusion layer should be thinned.

Temperature is the first factor that affects the cathode diffusion layer [36]. As the temperature increases, cathode film thickness decreases. Agitation is another factor that needs to be considered. Increasing the agitation speed will again decrease the film

thickness, so the agitation should be as much as possible. Agitation is also necessary for the temperature and concentration homogeneity of the electrolyte. The third factor is the current density, as current density increases the film thickness decreases. Finally, increasing the (anode type) metal ion concentration in the electrolyte will also decrease the diffusion film thickness. On the other hand, mixing other kinds of salt can increase the diffusion film thickness; therefore the electrolyte should be kept safe from contamination.

Obviously, cathode film thickness is not the only thing that affects the electroplating efficiency. As the cations coming from anode is reduced when they reach to cathode, hydrogen gas is released. If the current density is too high, the gas release gets faster which results in a porous deposition of metal. The porous structure results in dark surface with low reflectivity and low structure elasticity. Therefore, the current density as well as temperature and pH should be in their optimum values for electroplating. In [37], satisfying information about the plating process, the linear relationship between the plating time and plating thickness can be seen. In the same study, the stiffness, elasticity, conformity and brightness of the plated nickel versus plating thickness and current density relationships are explained.

3.2.4.2. Electroplating Bath Setup. The design of the plating bath setup is another work done for the fabrication of both of the first and the second generation MEMS devices. While studying with chemicals, safety comes first. Since the process is mainly acidic, the material chosen for plating path should be resistant to strong acids. Choosing 1 cm thick polypropylene for the walls of the bath will be safe enough for the strong acid.

The electrolyte is expensive, so the dimensions of the bath are chosen carefully. The inner dimensions are 30 cm, 15 cm and 25 cm length, width and depth, respectively. Considering also the 3 cm safety margin depth, which is left empty, a bath with these dimensions can only take around 10.5 l electrolyte. Also, this way there will be enough distance between the electrolyte and the copper bars which are placed

for taking electrical contact for anode and cathode easily.

Temperature homogeneity is important, it will affect the quality and characterization of plating. In the beginning, the heating is supposed to be done via a heater sinking into the electrolyte vertically from one corner, but the heating was not homogeneous. Therefore, the heating technique is changed, even though it is very effort consuming. We opened two 4.5 cm and 1 cm diameter holes at the bottom of the side walls of the bath. A quartz heater is placed horizontally through the big hole. Through the smaller hole another thin quartz tube is placed. This quartz tube preserves the thermocouple temperature sensor inside it from the acidic electrolyte.

To put it more correctly, the quartz heater and the thermocouple is not put through the holes, they are actually screwed to the holes. To prevent leakage a separate polypropylene part is designed, machined as a flange and welded to the holes. Another screw-like part is added to the heater so that they are screwed through the holes. To take another precaution against liquid leakage, a resin like glue is coated inside the flange. Lastly, on the outer parts a water proof silicon liquid seal is coated. The heater and the sensor is connected to a control unit outside the plating bath which controls the temperature with 0.1 °C precision. The prepared bath can be seen in Figure 3.14.

Before starting to prepare the electrolyte solution, the plating bath is bleached with DI water for 8 hours. Then it is bleached with 60 g/l trisodiumphosphate solution at 50 °C temperature for 8 hours. Lastly, the polypropylene plating bath is filled with 5-10 % (in this case it was 8 %) H_2SO_4 solution till the top and is bleached at 60 °C for another 8 hours. The bath is rinsed and dried.

The electrolyte used in this process is a sulphamate based solution. It is a commercial product of Enthone. The solution enables fast, ductile, bright, low stress, stable electroplating of nickel. The complete formulation of electrolyte solution is given in Table 3.8. The solution is agitated with a magnetic stirrer rotating a paramagnetic fish inside solution with more than 1000 rpm rotation speed. The prepared solution in this study has 3.38 pH value which is close to the optimum value.

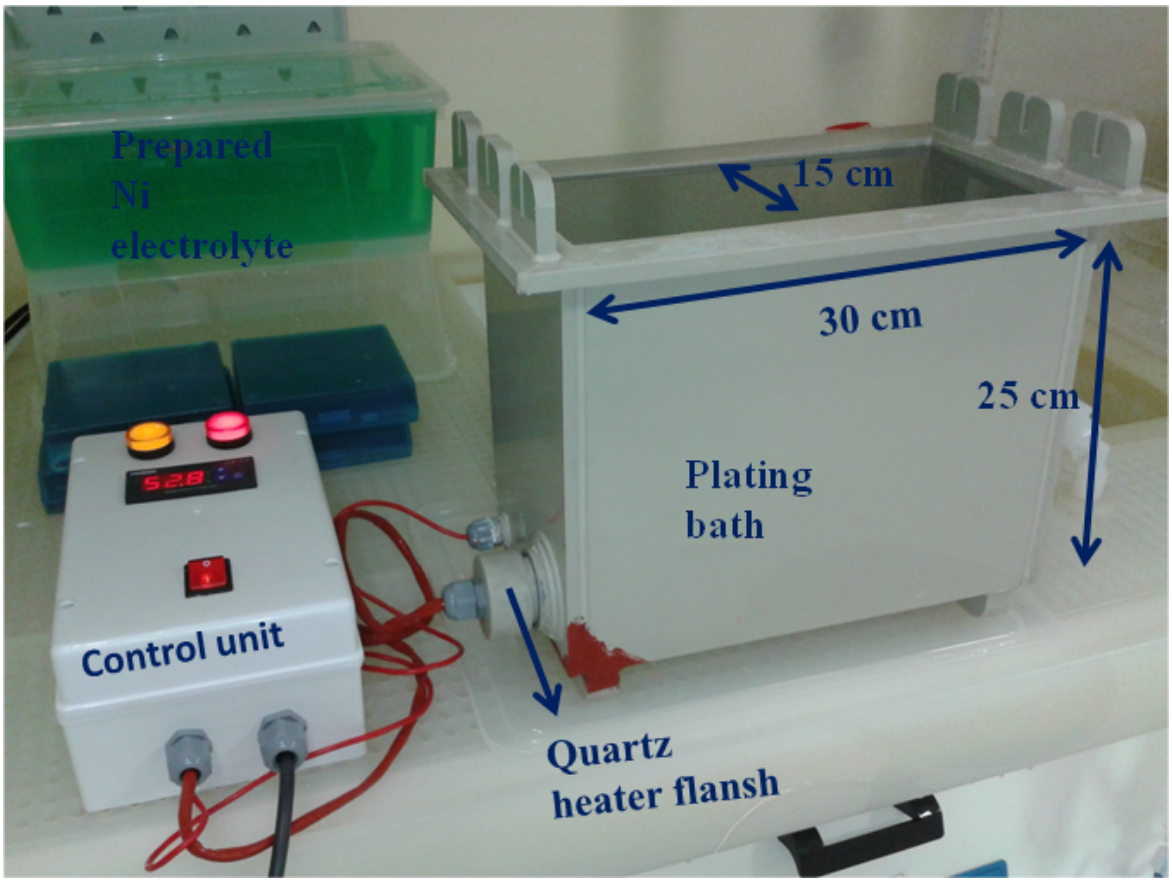


Figure 3.14. The photograph of the plating bath setup in cleanroom.

Table 3.8. Prepared electroplating bath compositions and operating conditions.

Nickel as metal	g/l	122
Boric acid	g/l	40
LECTRO-NIC 10-03 Anode Activator	ml/l	85
LECTRO-NIC 10-03 HSL Addition Agent C	ml/l	22
LECTRO-NIC 10-03 HSL Wetting Agent	ml/l	10
pH		3.38
Temperature	°C	58
Agitation	rpm	1000
Current Desity	A/cm^2	smaller than 0.25

The electrolyte should not be contaminated by any unknown particle. Also, in the beginning the nickel ingot has some black spots and stains on the surface even though it is 99.95 % pure nickel. The anode and the socks, which are used as a filter, are cleaned first in DI water for 30 minutes then in 2.5% H_2SO_4 solution and lastly in DI water again. In the meantime the anode is brushed with a toothbrush for further cleaning. In the end they are both dried with nitrogen.

The contact regions of ingot with the current carrying cables should be isolated from the electrolyte. Isolation band can be used for this purpose. However, to be on the safe side the contact region should be kept dry and therefore out of electrolyte.

To carry the heavy anode which is around 1.5 kg, an anode holder is drawn in SolidWorks 2013 to meet the requirements. The front and back side views of the designed holder can be seen in Figure 3.15 and Figure 3.16, respectively. The holder supports the anode from beneath and with two belts it is kept in vertical position. To leave as much open areas on anode as possible (to not interrupt electrical and liquid current between anode and cathode) and to allow agitation as much as possible, the belts are kept as narrow as possible and the back of the holder is designed as a fence like structure. The holder structure is strengthened in necessary positions, by making those areas thicker and putting circular features to necessary positions. Moreover, the holder can be hanged to the bath wall so that the current contacts can be kept safe and dry out of electrolyte. The back of the holder does not contact and so it does not stick to the bath wall thanks to the small bulge that was put at the backside of the foot shaped structure. This is important, because if it sticks to the wall the liquid flow around the anode will be interrupted.

3.2.4.3. Electroplating on PCB Copper. The electroplating process is optimized on FR4 samples, observed to be a successful process. The plating on square openings with a 2.5 cm side length showed us that for 0.01 mA/cm^2 current density the plating thickness is linearly increasing with plating time (Table 3.9):

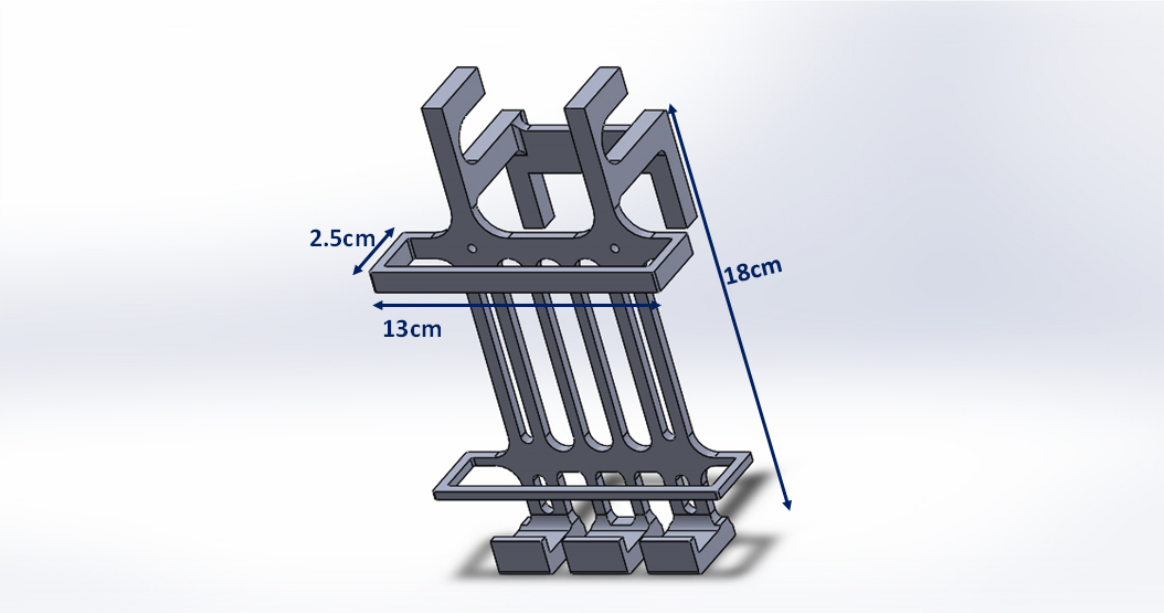


Figure 3.15. The front side of the anode holder designed in SolidWorks.

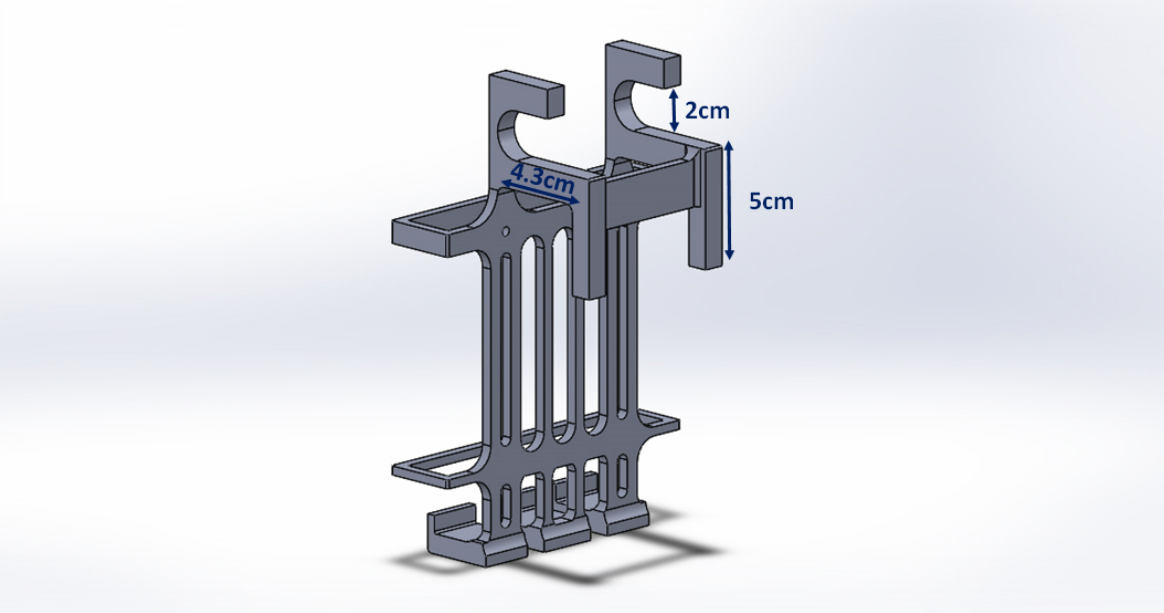


Figure 3.16. The back side of the anode holder designed in SolidWorks.

Table 3.9. Change of plating thickness with time [22].

Plating Time (min)	Plated nickel weight (mg)	Average Thickness (μm)
26.88	27	5
10	10	1.8
7.5	7	1.25
5	5	0.9
2.5	2	0.36

3.3. Outcomes

The second generation devices are designed, simulated, each fabrication step is optimized; but there is no characterizable device, yet. However, there is an accumulation of knowledge on the fabrication techniques and methodology. First of all, the devices are too narrow with a minimum feature size of 3 μm. This minimum feature size actually defines most of the geometrical features in this design including the beam and flexure widths, separation between anchor blocks and flexures and perforation dimensions in the devices with masses.

To increase the number of devices such a densely populated design is necessary; but this makes the fabrication process really hard. If the sample is not developed sufficiently then that means we have thinner devices which will not endure vibration, they will be problematic for characterization. If the sample is overdeveloped even a little, which is the general case during lithography processes, that may cause electrical shorts between successive devices or neighbor anchors. As it is explained in Section 3.1.3 all the resonators in a group are series connected and they are placed parallel to each other. Therefore any electrical short between any two resonators or partial anchors will cancel out two bridges, because the current will not flow through these bridges. Losing perforations may not be that much critical in terms of getting a working device.

There is another difficulty of fabrication relating the design geometry. That is, the nosings (see Figure 3.4 through Figure 3.6) expanding from the anchors to make contact with the bridges (the movables parts of the resonator) are just in the same width with the beams. During developing process it is inevitable that the corners of those nosings are rounded or even the nosings themselves are shortened. This makes matching between the masks, and in the end matching the beams with the anchors, difficult or sometimes impossible. During this study, these effects are minimized by further optimization of the process over many trials.

4. GLUCOSE MICROWAVE SENSOR WITH SRR

Split ring resonators are studied for no more than three decades. In most primitive forms, they are basically metal rings with a split. Despite their relatively simplistic design they can have strong resonance characteristics depending on their geometry. Theoretically, they can be fabricated for any application with a resonant frequency spanning from hundreds of MHz to THz range [38–40]. The ring resonators can have very high quality factors. When they are used as a certain array of devices they can provide an effective negative permittivity and a negative permeability, which results in a negative refraction index [41–46]. Thanks to these strong and unnatural characteristics, they can be used in variety of optics, electronics and biomedical applications, such as superlenses [47], biosensors [48], and magnifying hyperlenses [49], subwavelength imaging and cloacking [50].

Split ring resonators can be used as biochemical sensors. Due to their high quality resonant responses they are quite useful in detection of certain molecules [52]. Detection technique mainly utilizes the resonant frequency shift which is mainly caused by either the change in capacitance value or in inductance value or in both values of the resonator. It is known that the capacitance and inductance values are mainly determined by the geometry of the device. The change in geometry causes a change in resonant frequency. The resonant frequency of a split ring resonator is determined by its characteristic inductance (L) and capacitance (C), as in Equation 4.1. The inductance value depends on the total length of conductive line, in this case copper. The capacitance value, on the other hand, is the sum of the gap capacitance and the fringing capacitances resulting from the surface and side walls of the conductor. Therefore, the most direct way is changing the capacitance and inductance by playing with the resonator size. However, the capacitance value can also be changed by changing the electromagnetic properties of the media.

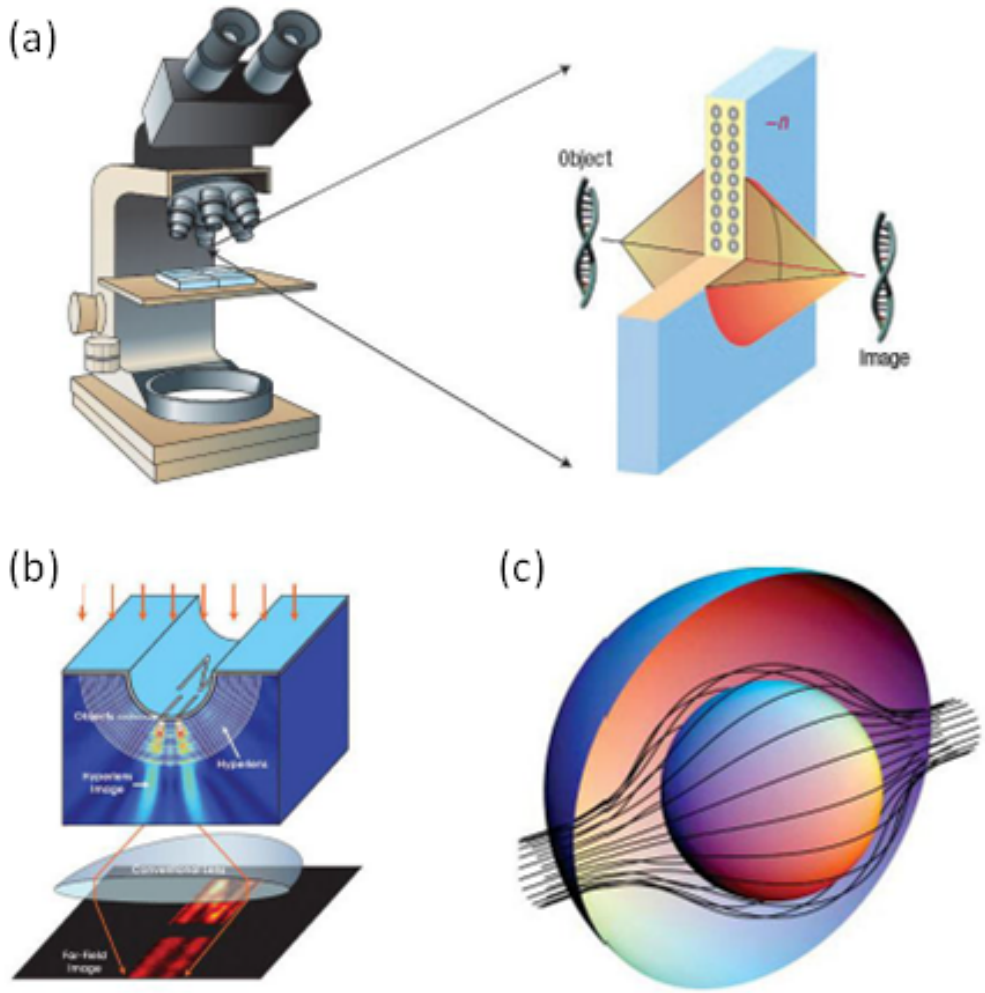


Figure 4.1. Some metamerials applications: (a) superlens, (b)magnifying hyperlens, (c) cloacking device [51].

$$f = \frac{1}{2\pi\sqrt{LC}} \tag{4.1}$$

As a bioapplication, exploiting this property, SRRs will be used for monitoring the presence of glucose inside a solution sample, in this thesis. Relative responses of glucose solutions of different concentrations and different volumes and also the enzymatic reaction of glucose with glucose oxidase (GOx) enzyme will be characterized. Possible solutions are proposed for the problems considering the measurement technique. In the end it is aimed to design an innovative blood glucose sensor. For this purpose, learning the theoretical background starting from the diabetes disease to the blood glucose monitoring sensor (BGMS) technologies will be useful.

4.1. Introductory Information on Diabetes

Diabetes can be described as the failure of blood glucose regulation of the body. The normal values for the blood glucose is 4.4 – 6.6 mM (80 – 120 mg/dl) whereas the pathological range is 2 – 30 mM (36 – 540 mg/dl) [53]. If glucose level in bloodstream is higher than the normal value it is called as hyperglycemia, if the glucose level is lower than the normal value it is called as hypoglycemia.

In diabetes mellitus, blood glucose is higher than the normal values. There are two types of diabetes mellitus. In type 1 diabetes, the patients' pancreas cannot produce enough insulin to keep the glucose level under control. In type 2 diabetes, the body cannot use the produced or injected insulin effectively. Insulin is a hormone produced by pancreas which allows glucose in bloodstream to enter the body cells to be used for energy or for storage as a future source of energy. Persistently high blood glucose can trigger severe health problems such as blindness and damage to retina and kidney and loss of organs as a result of amputations. Even with today's advances in medical care technology diabetes is not a curable disease, however, it is manageable. The patients with diabetes diagnosis should control their blood glucose level several

times a day and keep it in the normal interval by injecting insulin to their body when needed.

The diabetes is one of the most common diseases that can be seen in many patients from all ages. According to World Health Organization report [54] it has also a tremendously increasing trend. According to 2011 data there were 285 million people diagnosed diabetes, and this number is estimated as 439 million by 2030 with an increase rate of 7 million diabetes diagnosis each year [55]. Even though there are intensive study on curing diabetes, such as artificial pancreas growing, it looks like it will not happen in the near future. There are also other studies for curing the disease such as pancreatic cell transplantation [56, 57]. However, all these studies suggest tissue transplantation as a solution, which is always a risky operation. Therefore, it is not curable for now, albeit the diabetes can be kept under control.

Considering the prevalence of the diabetes cases as well as its rapidly increasing trend, it is no surprise that blood glucose measuring sensors dominates the sensor market. The BGMS were estimated to have 85 % of the total biosensor market which has a total market value of USD 6.1 billions in 2012 [53,58]. Therefore, the commercial potential of BGMS market attracts many researchers as well as investors. There are several companies in blood glucose sensor market and various studies on different devices and methods for monitoring the blood glucose.

4.2. Methods Used for Blood Glucose Sensing

There are many methods studied for blood glucose sensing [59]. In terms of their intrusion to the body of the patient these methods can be divided into two categories: invasive and noninvasive.

4.2.1. Invasive Techniques

The invasive methods generally use a lance-like or needle-like structure to take a tiny droplet (exact amount changes with the applied technique and different brand

sensors) and analyse the sample out of the body. The invasive methods generally utilizes three different techniques to analyze blood glucose: reflectance photometry, amperometry and coulometry. All commercial sensors on the market utilizes invasive methods so that they mostly use one of these techniques. The commercial products will also be explained in Section 4.3.

4.2.2. Reflectance Photometry

As an old fashioned, home-use blood glucose monitoring technique the reflectance photometry is the way to read out the glucose value in the first generation commercial glucosemeters. An enzyme, mostly GOx or glucose dehydrogenase (GDH), inside the strip catalyzes the oxidation of the blood glucose. The oxidized glucose reacts with a chromatic reagent, mostly an iron or an iron compound, which results in a color change of the compound. The change in color depends on the amount of glucose in the sample. By comparing this color change to a color chart, which shows the corresponding glucose concentration intervals, numerical values for the blood glucose level are obtained.

The first attempt for the detection of diabetes was also using reflectance photometry. However, that time urine was used as the sample instead of blood [60]. Instead of an enzymatic reaction, the glucose containing urine was reacting with a copper-compound reagent and the amount of glucose was tried to be estimated. However, containing many other ions, urine certainly cannot provide us with the correct results. Also, its concentration changes too much depending on liquid intake. Consistently, it is shown that there is no reliable relationship of the blood glucose with the urine glucose [61, 62].

Even though the blood sample is used in reflectance photometry, there are still too many limitations on utilizing this technique. First of all, the technique is affected by temperature, humidity and altitude. Moreover, the color chart can only provide semiquantitative results for blood glucose concentration. That is, it can only provide a concentration interval. Even this can be interpreted wrongly because of the insufficient

illumination of the environment.

4.2.3. Amperometry and Coulometry

These two methods will be explained together as both of them utilize electrochemical techniques. The glucose in blood sample is oxidized by the enzyme (again either GOx or GDH) inside the strip as in the reflectance photometry. However, this time this reaction leads to a transient current which is proportional to the amount of glucose in blood sample [63]. This current is converted to a numerical value via an electronic system.

There are also differences between amperometry and coulometry. In amperometry, only a small portion of the sample is oxidized by the enzyme and the resulting current is multiplied to scale the measurements to the blood glucose levels.Therefore, it can be affected by the hematocrit, environmental temperature, medications and several other factors even though the measurement result are mostly very reliable.

The coulometry, on the other hand is a relatively new technique. It uses the least amount of sample among the invasive techniques, with a blood sample size of 300 nL. In coulometry all of the sample is oxidized and the total amount of charge is measured by the measuring the current resulted. Coulometric devices have a smaller range of measurement, however they have higher precision [64].

4.2.4. Noninvasive Techniques

The intensive study for a noninvasive method that can monitor the blood glucose concentration led to many different techniques. Raman spectroscopy [65, 66], birefringence measurement [67], optical coherence tomography [68], electrical impedance measurement [69], infrared (IR) [70], surface plasmon resonance in nanoparticles [71], photonic crystal photometry [72] are all some of the techniques devised and utilized for a noninvasive BGMS (blood glucose measuring sensor).

There are many other studies on the field of noninvasive BGMSs. For instance in [73], a novel system using a double split ring resonator which is wearable to the abdominal to measure the real time blood glucose level is designed. In another study [74], glucose level is estimated with 8.3 % error by a two step approach. In the first step the glucose data is collected by near infrared spectroscopy and impedance spectroscopy from the skin surface. In the second step the data collected by these two methods is processed with a software to crate the estimation results. However, despite the number of techniques and very intensive study, there is not even a single noninvasive commercial blood glucose monitoring devices (BGMD) for home use yet.

4.3. Commercial Blood Glucose Measurement Devices

The market for glucose biosensor market and for diabetes-related healthcare technology has a huge monetary capacity which attracts several giant companies to the blood glucose sensor field. The leading companies such as Bayer, Minimed, Abbott, Lifescan, Roche Diagnostics and Dexcom are investing on the research and development of self-BGMDs. Despite the fact that few noninvasive sensors such as Smart Contact Lens developed by Google and Novartis may find a place in the glucose biosensor market in the near future, all commercial BGMS are invasive. Previously, sensors using reflectance photometry was also on the market. However, today all commercial BGMDs use electrochemical measurement technique, so that they are either coulometric or amperometric.

The detailed chemical reactions, performance criteria of each glucose sensor technology and how the researchers overcome the encountered problems are beyond the scope of this thesis. Therefore, only the structure and working principle of a commercial glucose sensor will be explained here shortly and a small comparison between the available commercial technologies will be provided.

4.3.1. The Structure of BGM Strip

An ordinary BGMS is generally in the form of a rectangular strip which basically consists of a capillary chamber to take the sample in and two or three electrodes. Figure 4.2 shows the structure of Freestyle BGM strip produced by Abbott. The three electrodes are working, reference and auxiliary electrodes. In most commercial BGMSs the auxiliary and reference electrodes are the same. The active electrode is generally screen printed carbon ink or vapor-deposited gold or palladium. The reference/auxiliary electrodes which are mostly made of Ag-AgCl are placed very close to the active electrode to make the capillary chamber smaller which means smaller blood sample volume is necessary. The smaller sample volume is desired for faster response, since as the sample size gets bigger the filling time will also increase as in Washburn equation [75]:

$$t_f = \frac{3\mu x_f^2}{[\sigma_l \cos\theta_w]s} \tag{4.2}$$

where t_f is filling time, μ is viscosity, x_f is length along fill axis, σ_l is the liquid surface tension, θ_w is the wetting angle and s is the capillary thickness.

4.3.2. Working Principle of BGM

The active electrode which contains the enzyme that will react with the glucose molecules are coated on the active electrode. The coated enzyme is either GOx or GDH. The glucose molecules in the sample are oxidized by the enzyme as the reactions in Equation 4.3 through Equation 4.6 indicate:

$$\text{Glucose} + \text{FAD} - \text{GOx} \longrightarrow \delta - \text{Gluconolactone} + \text{FADH}_2 - \text{GOx} \tag{4.3}$$

$$\text{FADH}_2 - \text{GOx} + \text{O}_2 \longrightarrow \text{FAD} - \text{GOx} + \text{H}_2\text{O}_2 \tag{4.4}$$

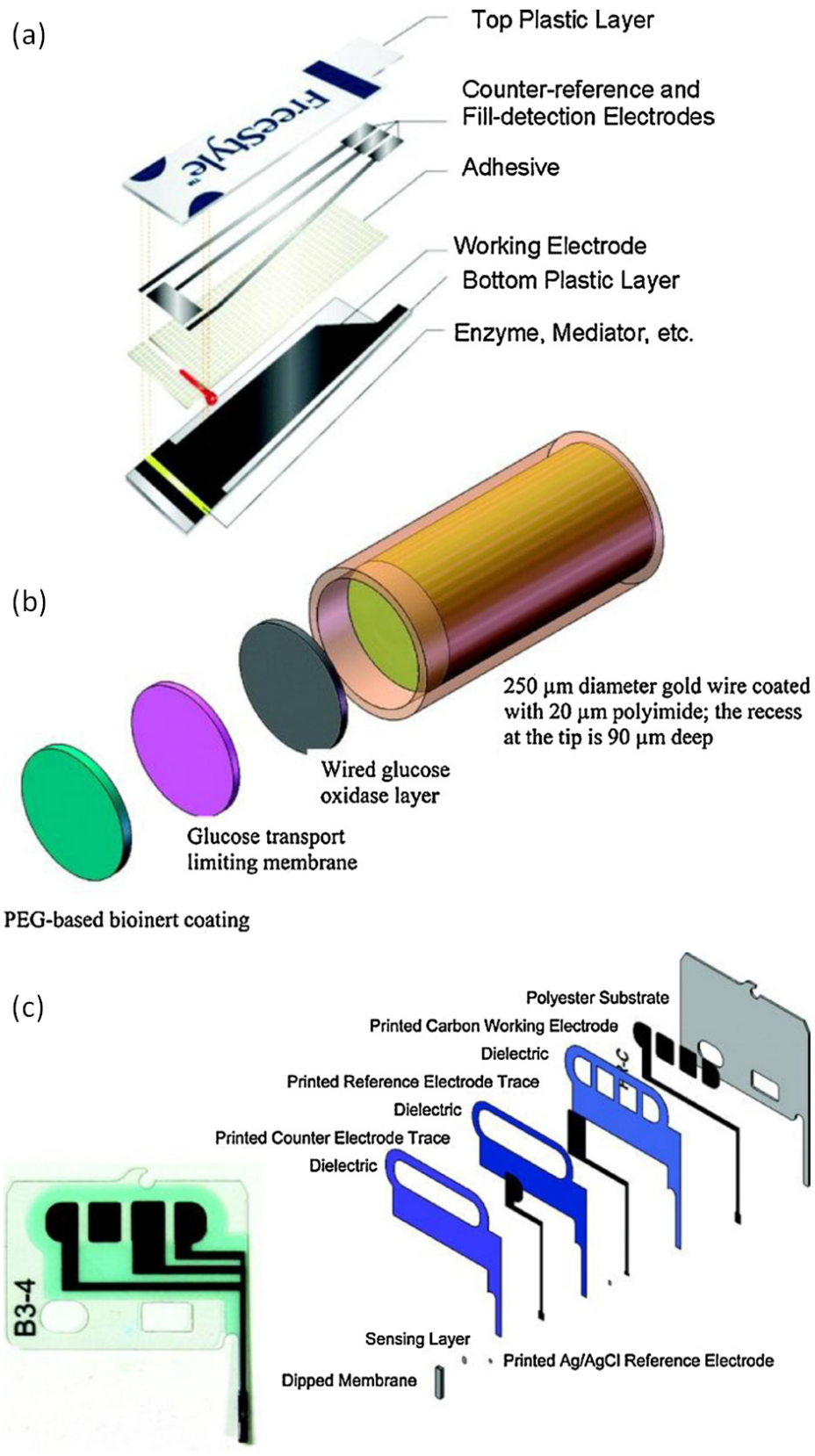


Figure 4.2. (a) Abbott's FreeStyle BGMS strip [76], (b) Subcutaneous wired GOx electrode [77], (c) FreeStyle Navigator Sensor Chip [78].

$$\mathrm{FAD} + 2\mathrm{H}^+ + 2\mathrm{e}^- \longrightarrow \mathrm{FADH_2} \tag{4.5}$$

$$\mathrm{PQQ} + 2\mathrm{H}^+ + 2\mathrm{e}^- \longrightarrow \mathrm{PQQH_2} \tag{4.6}$$

where FAD is flavin adenine dinucleotide and PQQ is pyrroloquinoline quinone.

Resulting electrons are transferred to the mediator substance which will carry the electrons to the reference/auxiliary electrodes. The mediators are the molecules which can be easily reduced or oxidized. In the reactions above the O_2 / H_2O_2 pair is the mediator when GOx enzyme is used. The utilization of O_2 as a mediator can result in limitations [79], therefore in commercial BGMSs alternative mediators may also be used. The reaction in Equation 4.7 is a general mediator reaction:

$$\mathrm{M_{red}} \longrightarrow \mathrm{M_{ox}} + 2\mathrm{e}^- \tag{4.7}$$

in which M_{red} represents the reduced mediator while M_{ox} is the oxidized mediator.

The mediator molecules are either reduced or oxidized when they reach the reference electrode exchanging electrons as in reactions which will create a transient current:

$$\mathrm{Glucose} \longrightarrow \delta - \mathrm{Gluconolactone} + 2\mathrm{H}^+ + 2\mathrm{e}^- \tag{4.8}$$

$$\mathrm{AgCl} + \mathrm{e}^- \longrightarrow \mathrm{Ag} + \mathrm{Cl}^- \tag{4.9}$$

$$\mathrm{Glucose} + 2\mathrm{AgCl} \longrightarrow \delta - \mathrm{Gluconolactone} + 2\mathrm{Ag} + 2\mathrm{H}^+ \tag{4.10}$$

This transient current will then pass through the external electrical circuit which is the device electronics. The device electronics, in general, contains several amplifier and signal processing units, necessary calibrations and a memory to record the past glucose measurement data.

4.3.3. A Comparison between Commercial Sensors

The information and comparison about several commercial BGMSs are provided in [80]. The sensors are all invasive to the body. Some of the sensors enable continuous, real time glucose level tracking whereas most of them are common strip-based single-use biosensors. The sensors enabling real time measurement are also should be changed with regular intervals. Most of the sensors do not use more than 1μl blood sample. Among todays commercial BGMSs, Freestyle series which is produced and marketed by Abbott is the sensor using the lowest amount of blood sample with a 0.3 μl volume size. The Freestyle is a coulometric device. As it was mentioned before in Section 4.2.3 the coulometric devices have smaller capillary chamber so they use smaller volumes of blood samples. All commercial sensors either use coulometric or amperometric measurement technologies. The response time of the sensors is minimum 5 seconds for most of the single-use BGMS.

4.4. The Proposed Model for Glucose Monitoring

The necessity for a noninvasive continuous method for blood glucose monitoring is undeniable. Obviously, if somehow the chemical composition of blood and tear liquids are related, using tear instead of blood can be a solution for monitoring blood glucose without invasion to the body. As it will be explained in Section 4.4.1, taking a sample from the tear liquid varies its chemical composition very much. Therefore, an in-situ measuring method is necessary. Also in situ measurement can provide us with the real time glucose data. Designing the sensor as a contact lens can be a possible solution for an in situ measurement technique. The effort on designing a contact lens glucose has led to many approaches [81–84].

Designing the contact lens as a split ring resonator is one of these approaches. In [85], an SRR based glucose measurement technique which utilizes the change in the reflectivity of the metamaterials due to the change in glucose concentration is presented. The novel idea behind this study is recording the real-time glucose concentration data with the help of a split ring resonator depending on the resonant frequency shift which is a result of permittivity change due to a chemical reaction of glucose in the presence of GOx enzyme. The products of the chemical reaction of glucose with GOx enzyme change the electromagnetic properties of the environment. SRRs are very sensitive to these changes, because it will change the gap capacitance. If the gap capacitance changes, the resonant frequency shifts.

In the remaining part of the thesis, the change in the behavior of SRR due the presence of glucose, DI water and enzymatic reaction will be presented. This sensor is aimed to be noninvasive which will also be a crucial advantage over the current commercial blood glucose sensors. In the final stage, this sensor can be designed as a contact lens on which the enzymes are wired and it will be wearable to the eye. For this purpose, the tear composition should be clearly investigated.

4.4.1. The Tear Composition

The tear film on human eye contains many different kinds of molecules and ions. There are many studies conducted on the tear composition [86], because it is essential to know particularly for ocular drug delivery. Moreover, a majority of noninvasive BGMSs are aiming to use tear instead of blood for sampling the glucose data of the body. Therefore, besides knowing the composition of tear, the relation between the tear glucose concentration and blood glucose concentration should be clarified in a characterizable manner.

There are three layers in the tear film: superficial lipid layer, aqueous media, and mucin layer. The superficial lipid layer is around 100 nm and secreted from the Meibomian glands. The lipid layer prevents the aqueous layer from rapid evaporation and thus prevents eye dryness. It also helps eyelids to slide over the tear film with an

ease.

Just beneath lipid layer there is an aqueous layer which contains mostly water. This layer also contains several biopolymers, glucose, proteins, glucoproteins, urea and inorganic salts. The total volume of aqueous layer is around 7 μl. It is secreted from the lachrymal gland. The reported thicknesses of this layer varies from 2.7 μm to 46 μm, one of the most recent reported value is 3.3 μm [87].

The mucin layer is located beneath the aqueous layer and mucous stratum. Thanks to several different glucoproteins in its content, it provides a hydrophilic surface for the aqueous media. The thickness is given as approximately 30 μm in [88]. The mucin layer also moves freely over the glycocalyx which is a layer of molecules that covers the membranes of the epithelia cells. From the publications, we can have an idea about the thicknesses of the tear layers. However, the reported values differs too much.

Another important point is the concentration of glucose in tear and its relation with the blood glucose concentration. Figure 4.3 reveals an interesting data set about several studies which investigates the average tear concentration using different methods since 1930 [89]. Studies are grouped by the type of the stimulation used to induce tearing (chemical, mechanical, and noninvasive). Each section is ordered chronologically within from left to right. According to this data set tear concentration varies too much with the stimulation technique. When acquiring sample may be due to the abrasion of conjunctiva, or maybe due to an unintended leakage of the intercellular liquid to the tear film, the acquired data for nondiabetic people is changing. Therefore, a stimulated tear sample may not give the correct data about the blood glucose concentration. That means, it is important to devise an in situ measurement technique after finding the relationship between blood and tear glucose concentrations. The results of a sample study on the main tear film concentrations and the corresponding values in blood can be seen in Table 4.1.

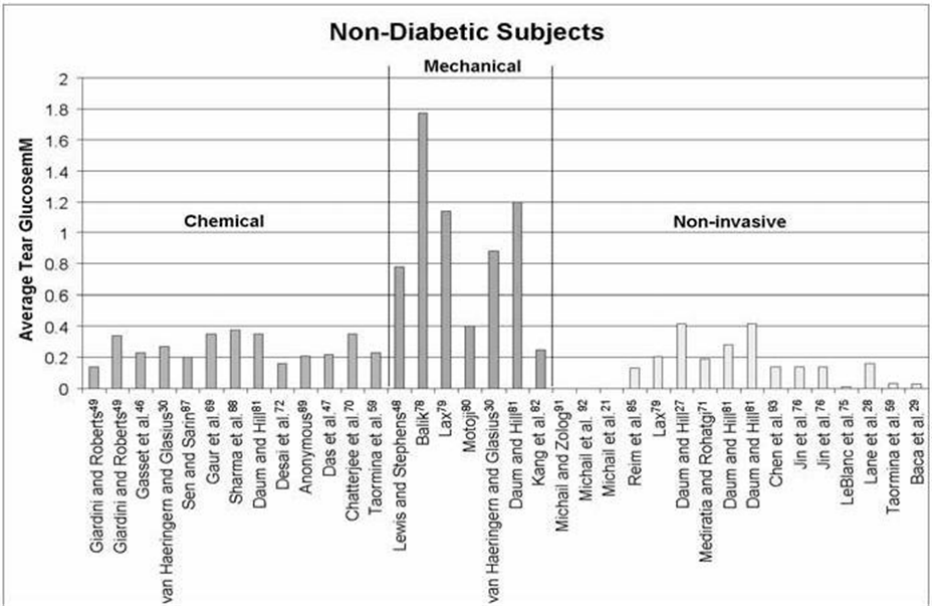


Figure 4.3. A collection of tear glucose level measurements on nondiabetic people since 1930 [89].

Table 4.1. Main tear film chemical concentrations and corresponding values in blood [90].

Component	**Tear Concentration**	**Blood Concentration**
Na^+	120 - 165 mM	10 - 145 mM
K^+	20 - 42 mM	3.5 - 5 mM
Ca^{2+}	0.4 - 1.1 mM	2.0 - 2.6 mM
Mg^{2+}	0.5 -0.9 mM	0.7 - 1.1 mM
Cl^-	118 - 135 mM	95 - 125 mM
$HC0_3^-$	20 - 26 mM	24 - 30 mM
Glucose	0.1 - 0.6 mM	3.3 - 6.5 mM
Urea	3.0 - 6.0 mM	3.3 - 6.5 mM
Lactate	2 - 5 mM	0.5 - 0.8 mM
Pyruvate	0.05 - 0.35 mM	0.1 - 0.2 mM
Ascorbate	0.008 - 0.04 mM	0.04 - 0.06 mM
Total protein	7 g/l	70 g/l

5. FABRICATION, SIMULATION AND EXPERIMENTS OF SRR BASED GLUCOSE SENSING

In this chapter, first of all the modelling and fabrication processes of SRRs, which are used for the experiments, are explained. A practical hybrid model is used to determine the dimensions of SRR structures which are matched to 2 GHz. 2 GHz resonant frequency is desired becacuse ZWB4 Rohde & Schwarz network analyzer in our laboratory can work in 300 kHz to 4 MHz interval. The proposed structure for glucose monitoring is a simple SRR structure which is actuated by a pair of monopole antennas matched to 2 GHz frequency. For this purpose, it is necessary to design and fabricate SRRs with a resonant dip at 2 GHz. The model is tested by CST simulations for the SRR designs with determined dimensions. The fabrication process and measurement setup are also explained in detail in the following sections. Finally, the results of several experiments considering the position, volume and concentration of the sample and the reaction time will be presented.

5.1. Theoretical Modeling and Simulations of SRR Structures

On Figure 5.1, the geometrical variables of an SRR are shown where r is the inner radius, w is the copper width, g is the gap width, h is the height is the copper plane, c is the separation between two consecutive rings, d is the FR4 (Flame retardant 4) substrate thickness, l_s is the width and length of the substrate plane.

Devices will be fabricated on copper coated FR4 platforms. Ignoring the resistance value of the copper line, the SRR can be modelled as in [91]. However, in that model, the devices are thought as conductive structures built in free air, not on an insulator such as FR4. This is an important detail, since the dielectric permittivity of FR4 is different from the air. Since the electromagnetic waves mostly travel through the boundary of two media, half of the waves travel in the air while the other half is still inside the FR4 media.

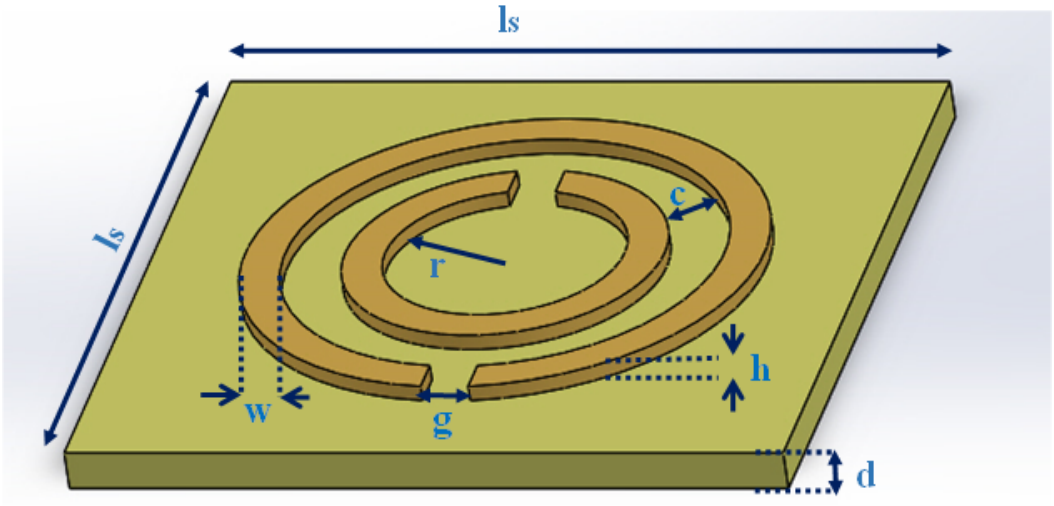


Figure 5.1. Split ring resonator: relative dimensions.

To compensate this difference, an effective value for the permittivity constant is modeled as in [92]. Instead of two media with different permittivity value, the model suggests a single medium with an effective value permittivity as in Figure 5.2.

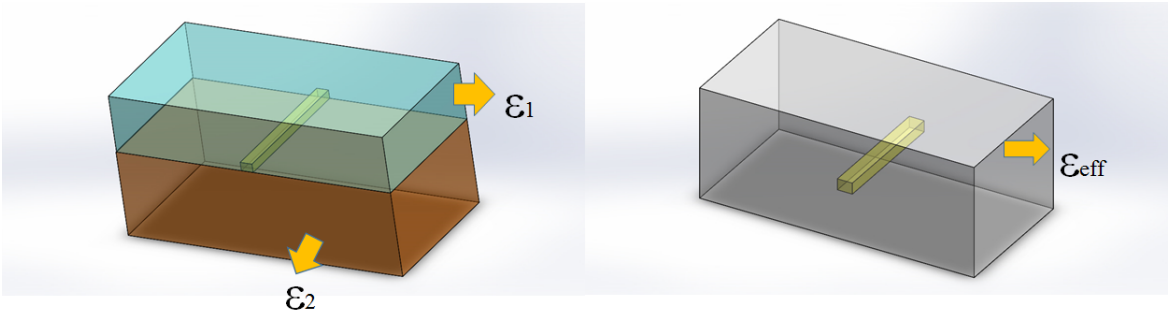


Figure 5.2. Two media with different permittivities.

This way, the two models will be combined and we get the hybrid computational model as in Equation 5.1 through Equation 5.6:

$$\epsilon_{eff} = \frac{\epsilon_r + 1}{2} + \frac{\epsilon_r - 1}{2 \times \sqrt{1 + 12w/d}} \tag{5.1}$$

where ϵ_{eff} is the effective permeability for a so called homogeneous medium, ϵ_r is the relative permeability of the substrate [92].

$$R_m = r + \frac{w}{2} \tag{5.2}$$

where R_m is the average radius of a single ring SRR.

$$L_{eff} = \mu_0 R_m \left(ln \frac{8R_m}{h + w} - \frac{1}{2} \right) \tag{5.3}$$

where L_{eff} is the effective inductance of SRR, μ_0 is the free space permeability [91].

$$C_{gap} = \epsilon_{eff} \epsilon_0 \left(h + w + g + \frac{hw}{g} \right) \tag{5.4}$$

where C_{gap} is the gap capacitance, ϵ_0 is the free space permittivity [91].

$$C_{surf} = \frac{2\epsilon_{eff}\epsilon_0(h + w)}{\pi} ln \frac{4R_m}{g} \tag{5.5}$$

where C_{surf} is the surface capacitance of the split ring resonator [91].

$$f_{srr} = \frac{1}{2\pi \sqrt{L_{eff}(C_{gap} + C_{surf})}} \tag{5.6}$$

where f_{srr} is the calculated resonant frequency of the SRR structure.

Using this hybrid computational model, dimensions of simple split ring resonator structures for different FR4 substrate thicknesses are designed (Table 5.1). The reason to design this many different resonators is that fabricating resonators that are matched to 2 GHz is not our only obligation, a good quality factor is also necessary to observe

a shift in the resonant frequency.

Table 5.1. SRR dimensions determined with analytical model.

Device number	**Substrate thickness (mm)**	**Radius (mm)**	**Gap (mm)**	**Copper width (mm)**	**Resonance frequency (GHz)**	**Gap angle (degree)**
1	1.59	7.2	1.2	2.0	1.997	4.7747
2	1.59	8.0	2.1	1.5	2.001	7.5201
3	1.40	7.2	1.9	1.9	1.999	8.3556
4	1.40	6.6	2.3	2.3	2.000	5.2087
5	1.40	9.0	1.2	1.2	2.000	5.0930
6	0.86	6.3	2.4	2.4	1.997	7.2757
7	0.86	8.0	1.5	1.5	1.998	5.3715
8	0.86	7.0	1.9	1.9	1.999	8.5944
9	0.34	8.0	1.2	1.2	2.006	7.1620
10	0.34	6.1	0.3	1.9	1.997	1.4089
11	0.34	5.5	0.5	2.4	2.000	2.6044
12	0.34	9.0	1.5	1.0	2.003	4.7747

The designs are also simulated in CST Microwave Studio program and the resonant frequencies are observed as in Figure 5.3. For the resonant frequencies of the simulated resonators, the average error percentage of this analytical model with respect to the simulation results is approximately 17 %.

5.2. Fabrication Methods

In this stage, designed resonators should be fabricated. For this purpose, designed resonators are drawn in L-Edit in two formats. The first format contains devices that are drawn to be on the same FR4 platform with the antenna pairs. The second format is the separate form in which only the resonators are drawn on a 3 cm

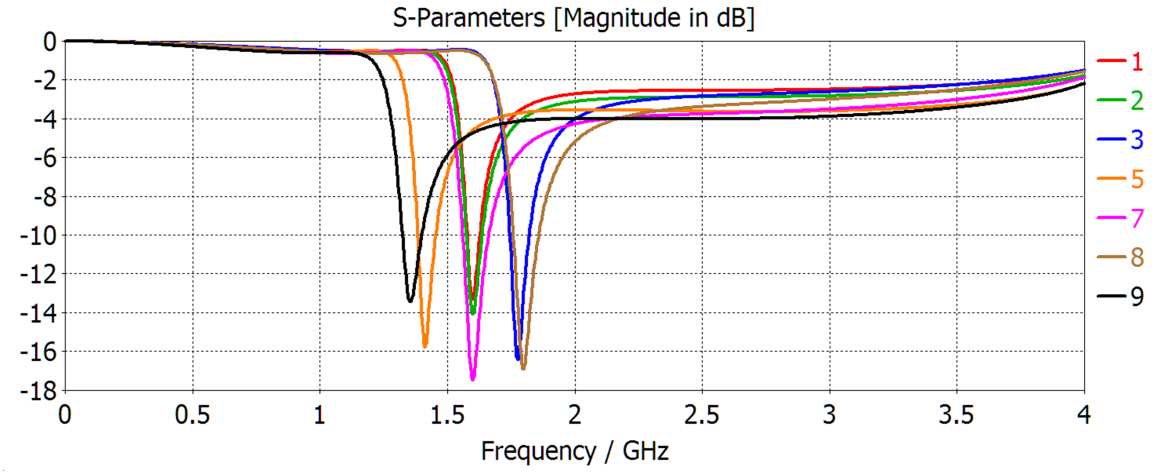


Figure 5.3. CST simulation results of SRRs designed with the hybrid calculational model.

to 3 cm FR4 substrate. In this second format, the resonators will be actuated by a separate pair of antennas.

In all drawings two important points are taken into account. In L-Edit the gaps can be designed as a pie wedge, so that the gap sidewalls are not parallel to each other. To make them parallel, rectangular compensation patches are added to both sides of the gap. The second point is that the sample will be placed right into the gap. Therefore, the position of the gap with respect to the edges of FR4 substrate is also important. For all designs, the distance of the center of the gap to the edge of the FR4 is kept constant as 6 mm.

There are two different fabrication processes for the resonators; each one has its own advantages and disadvantages. In the first technique a one-side-sticky paper is stuck on the whole surface of FR4 platform. The design drawings are opened on AutoCAD on a computer which is connected to a Versa Laser brand laser cutter and the paper on the design regions are burned by the laser precisely. Laser cannot burn or cut through the copper plane, but it burns paper and melts the sticky region so that, the sticky region uniformly coats the copper plane. In this step, it is crucial to adjust the laser power and precision to its optimum value. The low values of power

may not be enough to melt the sticky region whereas if the laser beam is too strong it can burn the sticky region instead of melting it. On the other hand, precision comes with a price of speed, to be more precise the process needs to be slower. However; if the burning process is too slow, the tiny flames occurring during laser burning process may also burn some the small regions at the boundary of the design region. In the end, that will cause a worse resolution. In Figure 5.4, the sample devices taken out of laser cutter can be seen.

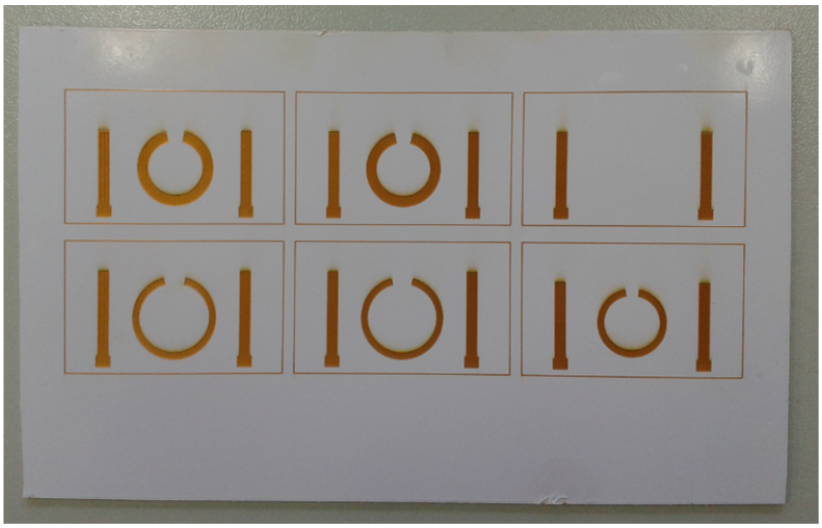


Figure 5.4. A sample photograph of the devices taken out of laser cutter machine.

The FR4 plaque is taken out of laser cutter and the sticky paper on it is carefully peeled off. The only covered parts are the burned regions. The sample is put in a standard PCB etching solution of hydrochloric acid and hydrogen peroxide, the etching process is controlled manually. Since the device regions are fully covered with the sticky region, the copper beneath is totally protected from the acid and the rest of the copper is etched away. The sample is then taken out of acid and washed away.

This fabrication technique gives us smooth devices. Since the copper is totally isolated from the acid during the process, the copper thickness and uniformity is preserved on resonators. Also, FR4 is not affected during wet etching so that the substrate thickness is also preserved. This is an advantage which the second technique cannot provide. However, this technique is troublesome requiring too much effort.

Wet etching and burning process cannot be controlled perfectly. Therefore, some tiny unwanted copper spots may remain on the substrate. Also, during cutting with guillotine, it is very hard to avoid cracking the substrate, particularly if the substrate is thick.

The second fabrication technique is fabricating the resonators with a PCB processing machine, LPKF S103. The machine, uses drilling, milling and cutting tips to shape the PCB mechanically. The fabrication with the machine is much easier and the fabricated resonator geometries are good. However, since the machine calibration is not good enough, it also takes away a portion of the substrate thickness. This changes resonance characteristics of the resonator a little. Initially, it may seem that it is an undesired result. However, this property plays a crucial role in the measurement setup.

During characterization of the enzymatic reaction the position and the shape of the droplet needs to be determined and preserved precisely. Otherwise, the characterization of the resonator response to the reaction will be very challenging since the response of the resonator vary too much with the position and the spread of droplet over time. To prevent this a small cell is necessary to keep the droplet just in the gap. For this purpose, a very thin rectangular cell is drawn on the gap of each resonator in L-Edit. Since the PCB processing machine does not mill the regions drawn in L-Edit and since it takes away some portion of the substrate thickness together with the copper on the rest of the surface, the post fabricated substrate thickness is measured as 1.09 mm with callipers. That means a 0.5 mm deep small reservoir is built in the gap position. This reservoir will be enough to keep the droplet inside.

In the end of both fabrication techniques the split ring resonators are coated with 7 μm thick parylene. When the droplet is placed in the gap, even though the droplet does not reach the metals at both sides at the beginning, there is a chance that the droplet will spread over time and will cause an electrical short in the gap because the water can become conductive due to reaction. When the gap is shorted, the resonance dip will disappear. Therefore, it is important to isolate the resonator. Being a polymer resistant to acid, heat, chemical reaction and oxidation, parylene is

the suitable choice for isolation. This way also, the copper beneath is protected from the byproducts of the enzymatic reaction. Lastly, the parylene is hydrophobic. That means, the droplet tends to preserve its shape on parylene, and not spread over it. In Figure 5.5, the devices fabriacted with a reservoir and coated with parylene can be seen.

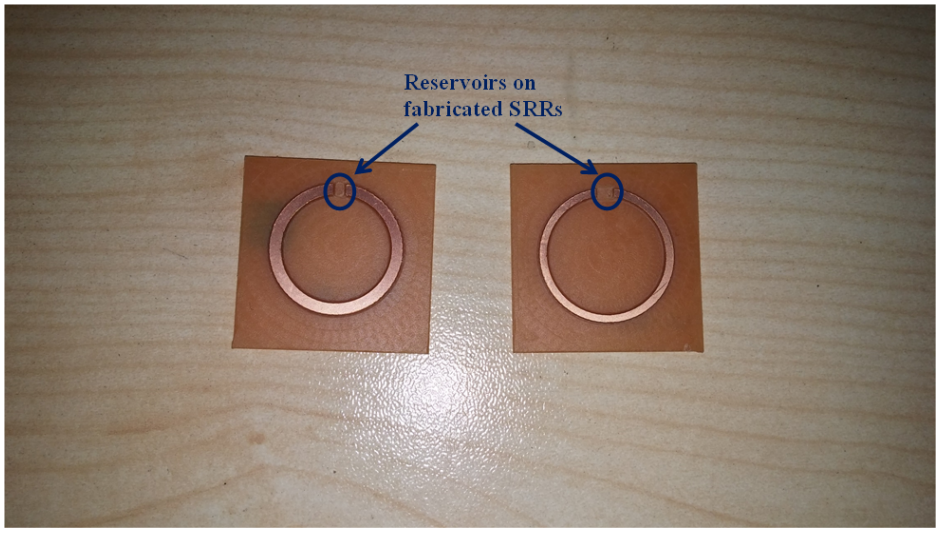


Figure 5.5. The fabricated SRRs with a chamber in the gap.

The devices fabricated in PCB processing machine is characterized with the network analyzer and their unloaded resonance behaviors are observed. Any of the resonators with a high quality factor and a resonant frequency close to 2 GHz can be used for enzymatic reaction characterization. In this case, device 1 in Table 5.1 is used.

5.3. CST Simulations with and without DI water

The chosen resonator is drawn in CST Microwave Studio. Approximately 0.5 mm decrease in the thickness of the substrate due to the fabrication with machine is also taken into account in simulation. Position of the gap, the substrate dimensions, and the uniform parylene thickness are also drawn identical to the actual case. Volume of the droplet that will be used during the experiment is 1 μl. The simulations with and without DI water in the gap gives the results in Figure 5.6. The difference between

the resonant frequencies of the unloaded case and loaded with DI case is 215 MHz. On the other hand, the resonance dip increased by 3.27 dB when DI droplet is placed in the gap.

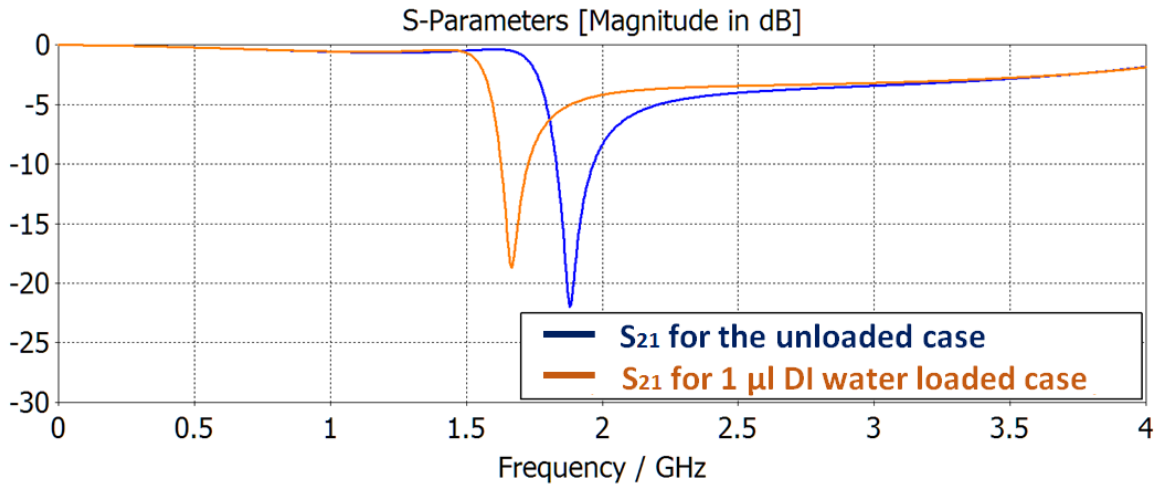


Figure 5.6. The simulation showing the resonance shift due to 1 μl DI water placed in the reservoir of SRR.

The effect of droplet on the electric field around the gap can be seen in Figure 5.7 and Figure 5.8, respectively. Also the surface current is given in Figure 5.9.

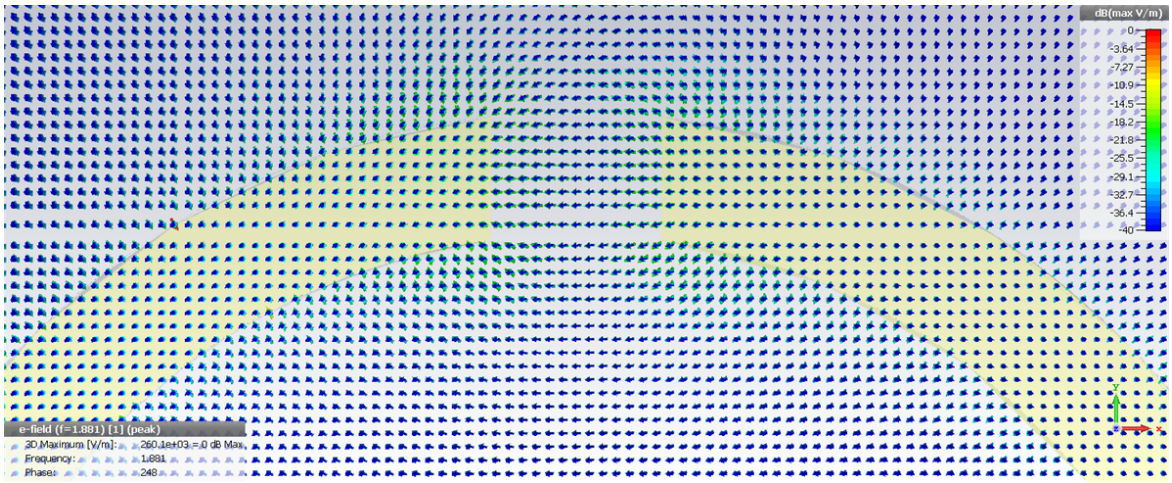


Figure 5.7. Electrical field distribution around the gap at the resonant frequency before DI droplet is placed.

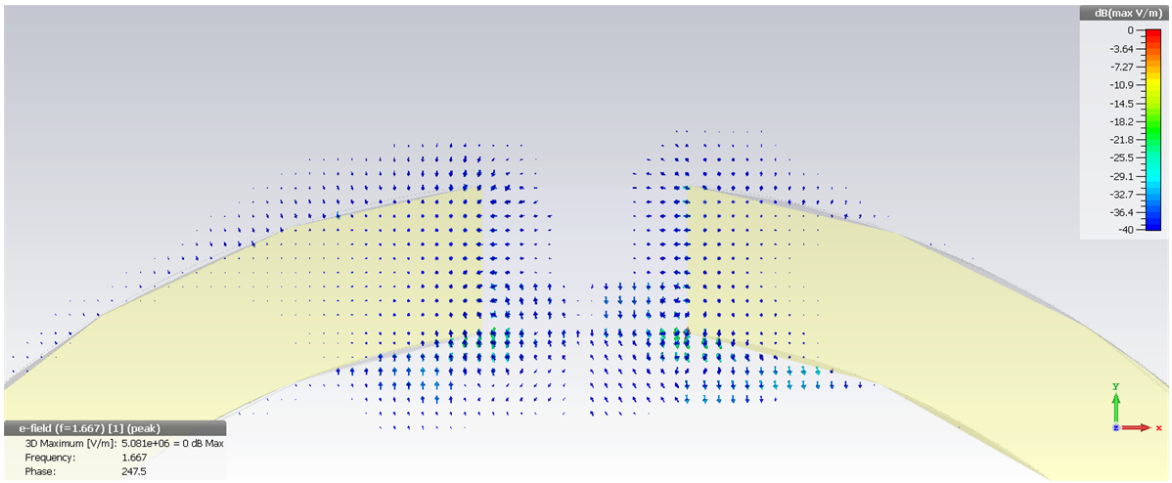


Figure 5.8. Electrical field distribution around the gap at the resonant frequency after DI droplet is placed.

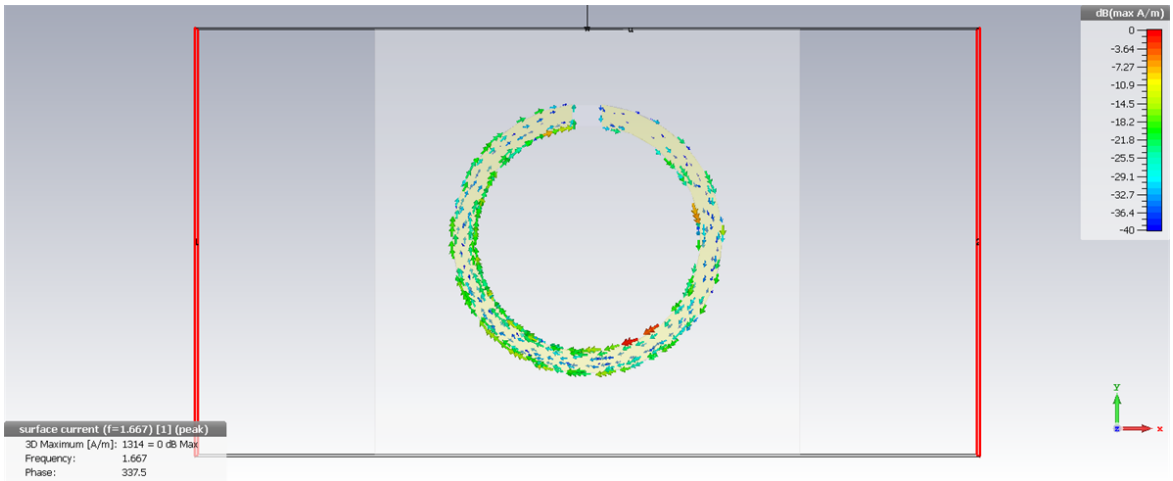


Figure 5.9. Surface current induced on the resonator.

5.4. Measurement Setup

The reliability and repeatability of the measurements are vital aspects of this study. In this section, the measurement setup is explained with the possible problems encountered and their suggested solutions.

First of all, we read out the transconductance parameters of split ring resonator with a network analyzer. Therefore, the set up should be calibrated and saved once and the calibration should be checked out at the beginning of every experiment.

The SRRs are actuated via a pair of monopole antennas. Any moving conductive object distorts the signal transmitted. First of all, it is thought that the measurement will be better if the resonator is placed inside Faraday cage, because the Faraday cage antennas and the reflected signals are also read out by the same antenna pair. This situation makes a healthy measurement challenging. The s parameters are distorted due to even our hand movements when we are in close range to the resonator. Therefore, it is necessary to manage the network analyzer from a distance away. A long cabled mouse and keyboard will be an adequate solution.

Finally, the experiment setup is stabilized as in Figure 5.10. The network analyzer is placed on an insulator table and the calibration is done to the end point of RF cables. An aluminum metal plaque with a pair of holes drilled through it is fixed in vertical position. Acting as a large ground plane, the metal sheet helps us get more clear response. The distance between the drilled holes is 5.4 cm. The ends of the RF cables are put through the holes and each of them connected to a monopole antenna matched to 2 GHz. Since both the antennas and the split ring resonators will lay parallel to the ground (vertical to the metal plane) a resonator holder is designed to keep them in position and fabricated in a 3D printer. The holder design is also necessary to prevent the possible stress on RF cables which may distort signal transmission. Moreover, by fixing the position of the resonator which is fabricated on a separate FR4 platform than the antennas, the reliability of the experiment will increase. The resonators are placed in the small pins, when we want to change the resonator that we

work with, it is taken off from those pins and the new resonator is placed in exactly the same position.

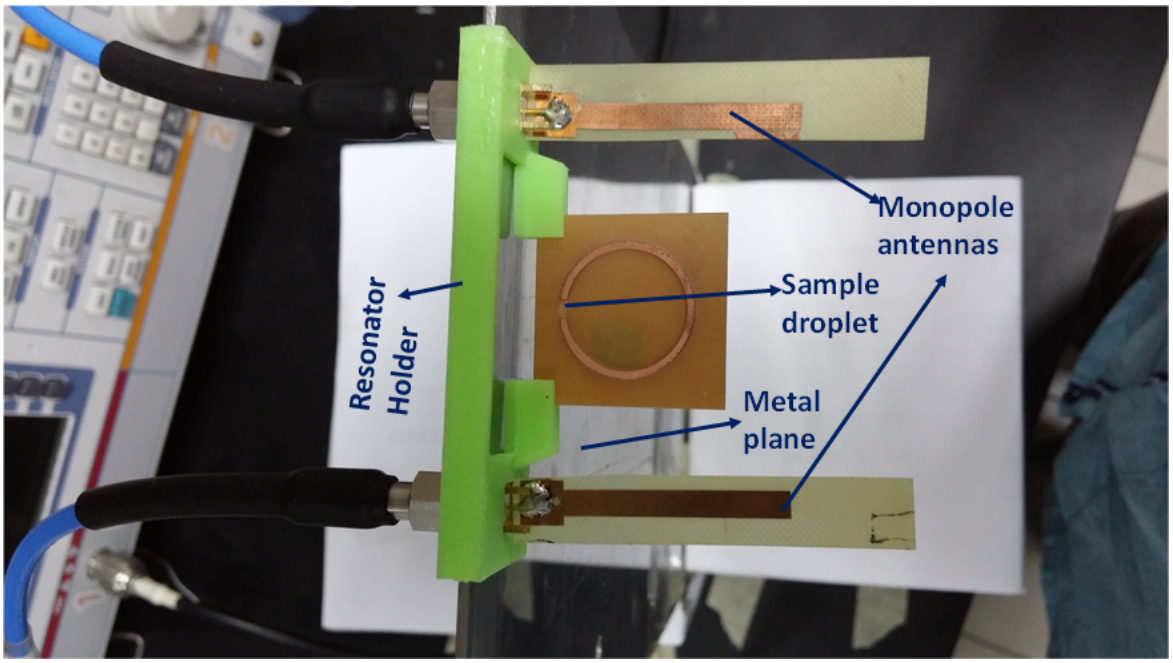


Figure 5.10. Characterization setup used for SRR microwave glucose sensing tests.

5.5. Characterization Procedure and Results

During the measurements the resonator 1 in Table 5.1 is used. First of all, the unloaded state s_{21} parameter is recorded with the network analyzer. The unloaded state is defined as the parylene coated resonator is placed in between the monopole antennas and holded by a 3D printed holder which can be seen in Figure 5.11.

Choice of glucose is important, because the GOx enzyme has different selectivitity for different glucose types. The GOx is the most selective to β-D-glucose, then different glucose types comes with lower selectivity [93]. The glucose used during this study is dextrose monohydrate glucose which is a commercial type that can be bought from a pharmacy shop. Dextrose glucose is used in serum liquid which is given to the bloodline of the patients directly as a glucose supplement. Therefore, it is assumed that Dextrose monohydrate can represent the glucose type in the blood. Then the glucose solution with 2.55 g glucose/ml of DI water initial concentration is prepared.

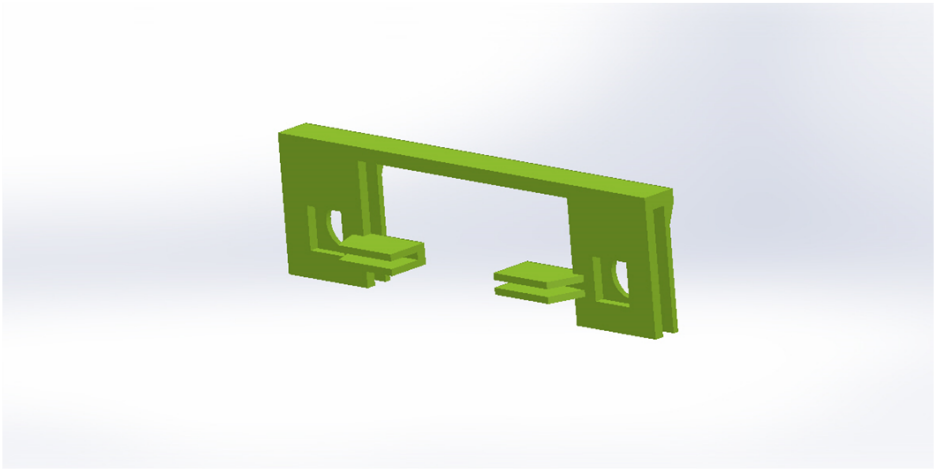


Figure 5.11. The resonator holder designed for glucose measurement setup.

Since it is widely used in food industry [94, 95] as well as medicine, the GOx enzyme is commercially available. However, in this experiment, it is obtained from fasTTest brand glucose test strips which can be seen in Figure 5.12. As it was mentioned in Section 4.3.1 there is a capillary chamber at back of the strip which contains the reactive chemicals including the GOx enzyme and its buffer. Since they are water-free, they are not activated until they touch to the sample liquid.

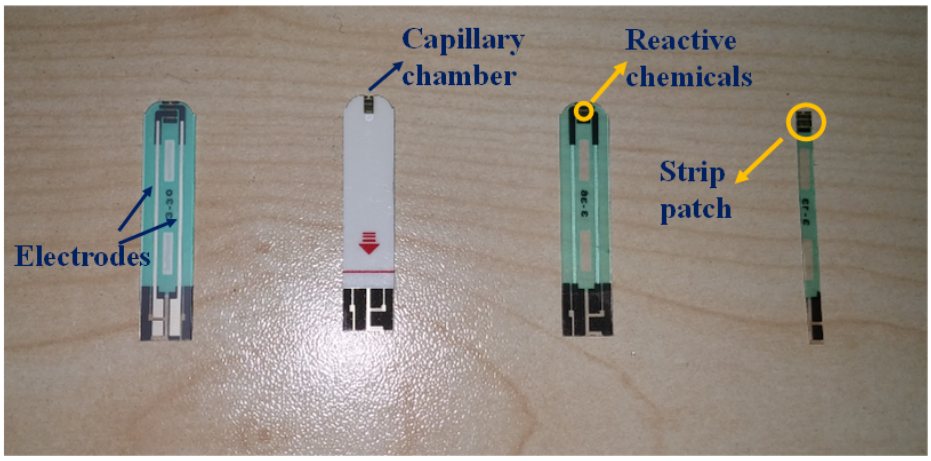


Figure 5.12. The fasTTest glucose test strips used in experiments as an enzyme source.

We cannot put the sample DI and glucose solution droplet directly to the strip

and characterize the change in SRR response, because there are too many parasitic effects that may lead us to wrong results. The metallic lines, which are the electrodes inside the strip is one of them. The position of the strip and the sample on SRR is another one. Even the shape of the droplet and evaporation of the sample during the experiment are also important causes of noisy or misleading results.

To use the enzymatic part of the strip efficiently, first the sticker part on the top side of the glucose sensing strip is stripped off. Then aligning through and including the electrodes, the side part are cut away. Then all other excess parts which do not carry the reactive agent are also cut away. A micropipette with a maximum precision of 10 nanoliter is used to take samples from DI waters and glucose solution. For DI water and for glucose dissolved sample different micropipette heads are used, so that none of the sample will not be contaminated by the other.

During all the experiments, after each measurement the surface of the substrate is carefully and rigorously cleaned with DI water and dried with cotton or paper tissue. The resonance characteristics of the system (the position of the resonant dip) should return to the unloaded after each measurement. That means there is nothing remained from the previous measurement. Extra care was taken to peel off parylene the parylene layer previously coated on the substrate during cleaning procedure.

Also, it is very important to prevent contamination as much as possible, because we cannot be sure about reliability and repeatability of the experiments if any one of the sample, enzyme or resonator is contaminated. For this purpose, the experimenter should wear gloves.

When the reaction starts the carrier concentration inside the droplet also starts to change, which affects the effective permittivity and the electric field distribution at the edges of the gap. The effective permittivity change will change the gap capacitance, which, in the end, results a shift in the resonant frequency. The experiments are conducted to observe the responses of the resonator in terms of several aspects:

5.5.1. The Effect of the Position of the Droplet

To see the effect of the position of droplet on the resonant frequency shift, DI droplets with different volumes are placed on five different positons according to gap which can be seen on Figure 5.13. The measurement results for every position are given in Figure 5.14 through Figure 5.18. It is observed that the largest shift occurred when the droplet is placed at the boundaries, then gap center and then the right and left (both equal) ends, respectively. Note that, for this case the manipulated resonator is planar and does not have a reservoir on it.

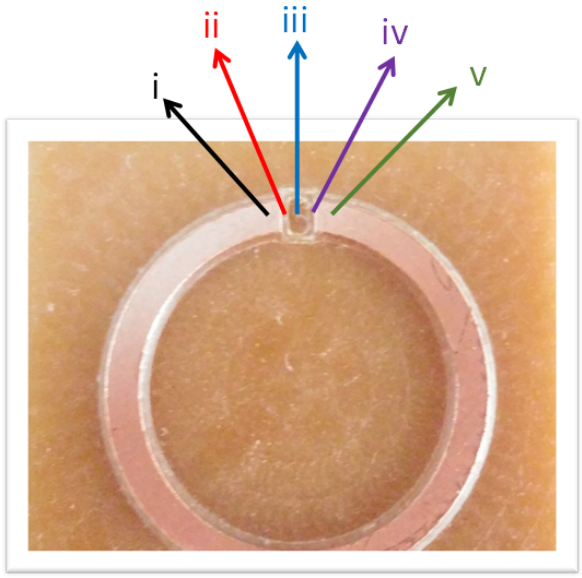


Figure 5.13. The measurement positions with respect to gap: (i) left end, (ii) left boundary, (iii) gap center, (iv) right boundary and (v) right end.

This experiment showed us that the most sensitive part of an SRR is the boundaries of the gap, because due to its shape the field density is the highest at the gap boundaries. Any disturbance here will cause a relatively larger frequency shift. Also a comparison can be made for volume of the droplet. As the volume of the droplet increases the resonant frequency shifts more towards left. Beware that there are still some outliers due to the imperfections of the measurement setup.

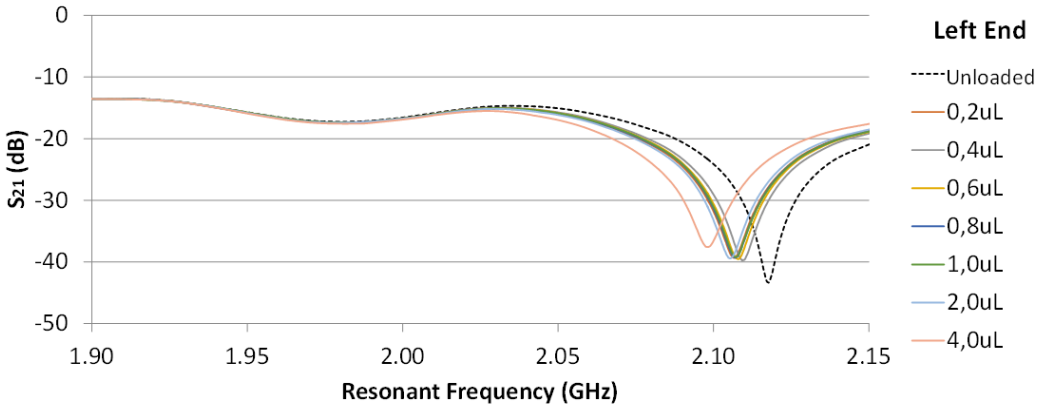


Figure 5.14. The effect of DI droplet placed on the left side of the resonator.

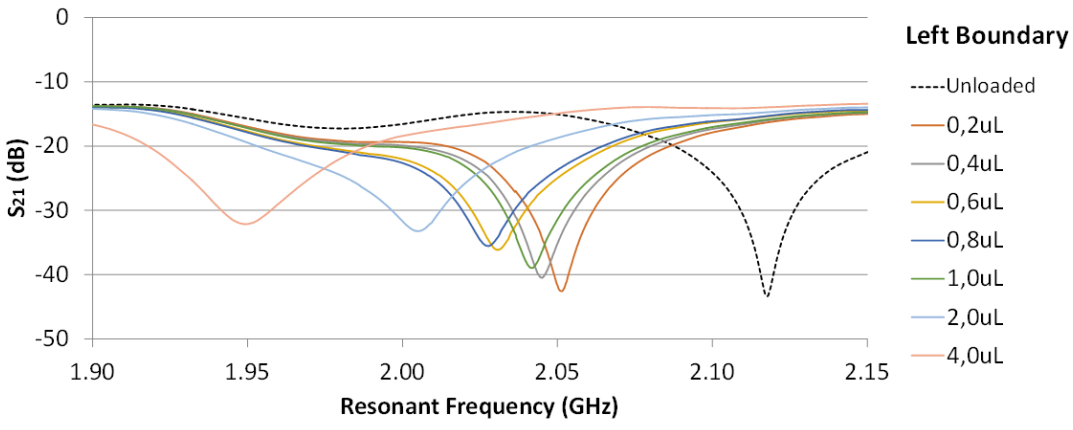


Figure 5.15. The effect of DI droplet placed on the left boundary of the gap.

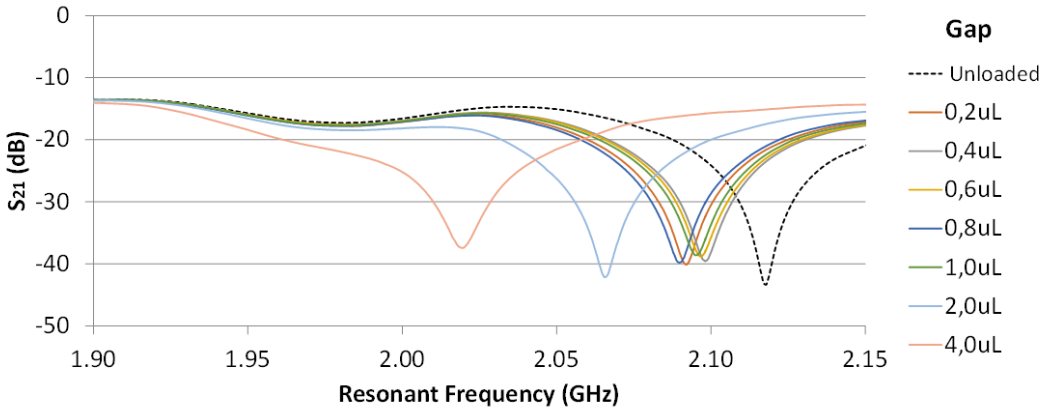


Figure 5.16. The effect of DI droplet placed on the gap.

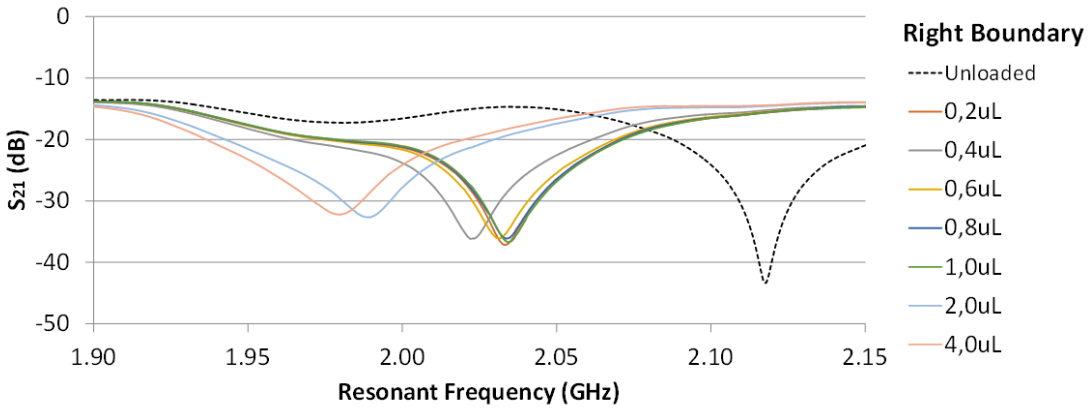


Figure 5.17. The effect of DI droplet placed on the right boundary of the gap.

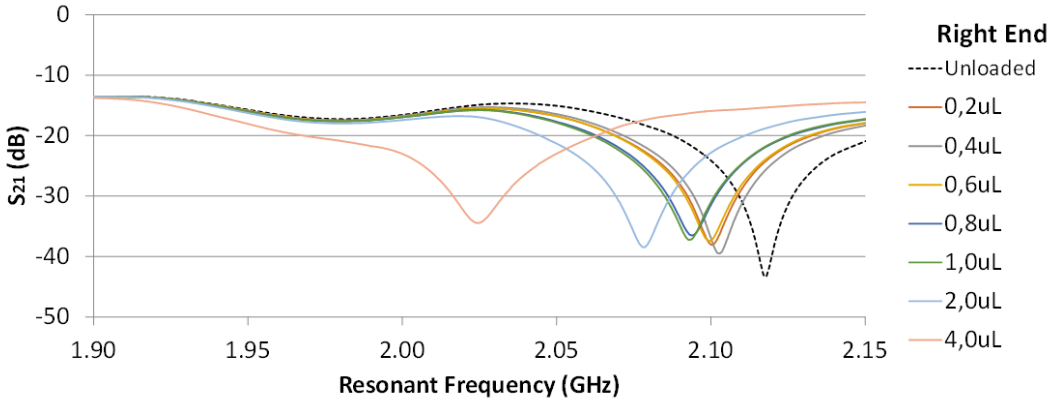


Figure 5.18. The effect of DI droplet placed on the right side of the resonator.

5.5.2. The Effect of Volume

In this measurement, SRR with a reservoir which is fabricated in a PCB machine is manipulated. The original thickness of the FR4 substrate was 1.59 mm. However, the substrates are made thinner by the PCB machine during milling the excess copper removal. The post – fabrication thickness of the substrate is 1.09 mm, so the resonator is 0.5 mm higher than the substrate plane. The whole top surface is then coated with 7 μm uniform parylene layer for isolation.

DI water droplets with different volumes are placed in the reservoir. Measurements are repeated five times for each volume size. In Figure 5.19, the maximum, minimum and average measurement values for each volume can be seen. Here, the trend line is drawn as quadratic however a linear pattern may also fit the data. Note that the values on the y-axis is the resonant frequency value (not the frequency shift); but the frequency shift can be extracted from the slope of the curve. In the figure it can be seen that the second measurement is varying too much, possibly due to imperfect measurement setup.

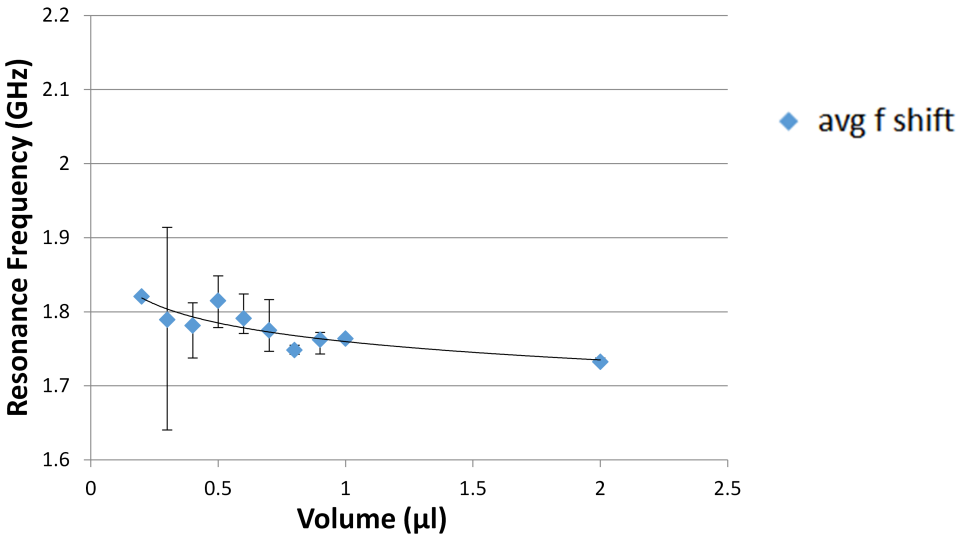


Figure 5.19. The effect of DI droplet volume.

Figure 5.19 shows that, the amount of resonant frequency shift is proportional to

the sample volume size. As the sample size in the gap is increased, the effect of droplet on the permittivity of the media will be more significant. The relative permittivity of DI water is 80 at room temperature. Therefore, an increase in the permittivity of the gap environment leads to an increase in the gap capacitance and if the gap capacitance increases the resonant frequency will shift to the lower frequency values.

5.5.3. The Effect of Concentration

In the third experiment the effect of concentration on the resonance characteristics and reaction dynamics is studied. For this experiment, again the SRR with a reservoir is used. Glucose solution with an initial concentration of 0.55 g/ml is prepared and for lower concentration measurement it is diluted with a necessary amount of DI water. In this part of the measurements it is necessary to utilize the enzymatic chemicals on the glucose strips (FasTTest BGM strip) mentioned before in the beginning of this section (see also Figure 5.12).

For this purpose, it is necessary to meet the reactive region of the strip with the droplet, without a significant disturbance to the droplet. For this purpose different methods are applied. The first method is to put a 1 μl droplet of solution to the reservoir using a micropipette and very carefully leaving the reactive part of the glucose test on top of the droplet. By this approach, it is aimed that the enzymatic region can make a better contact with the droplet. In each trial, first, the frequency response of SRR with strip patch on top of it is recorded without a droplet and then the measurement with a droplet is taken. It is hoped that this way the frequency shift is characterizable. However, due to the weight of strip patch the droplets changes shape and location which disturbs the response. Also it is hard to keep the strip patch in the desired position with a liquid beneath.

In the second method, the strip patch is placed in the gap first and the droplet is placed on top of it. However, the disturbance due to the patch is too much. Moreover, the position of the patch may not be identical everytime, so it is not repeatable.

After the fabrication of SRRs with a reservoir, another method become available. 1 μl droplet of the glucose solution is placed carefully in the reservoir and the reactive part is held (not left) in contact with the droplet for 15 seconds. After 15 seconds the strip patch is pulled away with an intense care about minimum disturbance to the droplet. Obviously, this method is also not perfect. A very tiny layer of the liquid always will be taken away by the patch because of the cohesion of the patch surface. However, it is the maximum precision that can be attained with the strip patches.

With this method, the reactive part is dissolved in the 1 μl droplet and reacted with the glucose inside the solution. Data is regularly saved with 30 seconds interval starting from the first moment the patch contacted with the droplet. Measurements are repeated five times for every concentration value. The effect of concentration on the resonance characteristics are shown in Figure 5.20 through Figure 5.22. Figures in the left column show the resonant frequency shift (GHz) versus different concentrations (g/ml) whereas the figures in the right column shows the change magnitude of the resonance (dB). The horizontal axis in each figure show the concentration values. From top to bottom, figures show the measurement results at 30 seconds, 90 seconds and 150 seconds. The trendlines on all figures are linear.

The amount of shift in the resonant frequency at any measured reaction time is more for the denser solutions. That is after a certain time, the resonant frequency shifts more for the denser solutions with respect to the time the droplet is first placed in the gap. This can be an indicator of the fact that the reaction with GOx is faster in a denser solution. A faster reaction means that after a certain time there are more reaction products which may result in a greater resonance frequency shift.

Considering the graphs on the right side which shows the change in the depth of resonance dip with respect to different concentrations recorded in different times, the denser droplets caused more shift in the value of scattering parameters after a certain time. For denser solutions the change in the magnitude of the dip is more.

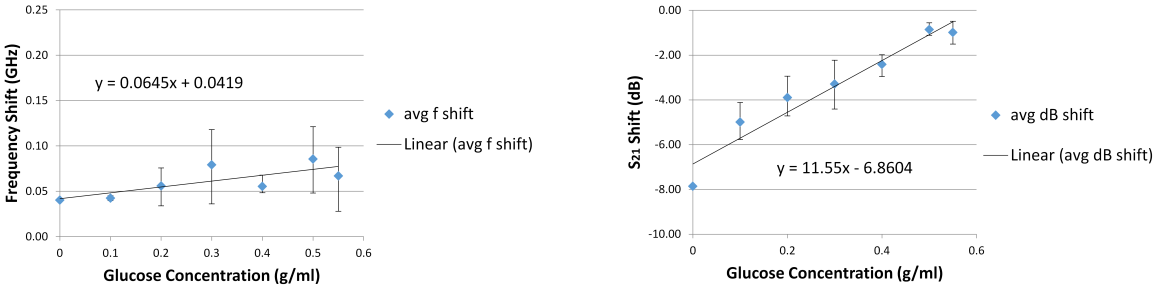


Figure 5.20. The effect of concentration on resonant frequency and dip value at 30 seconds.

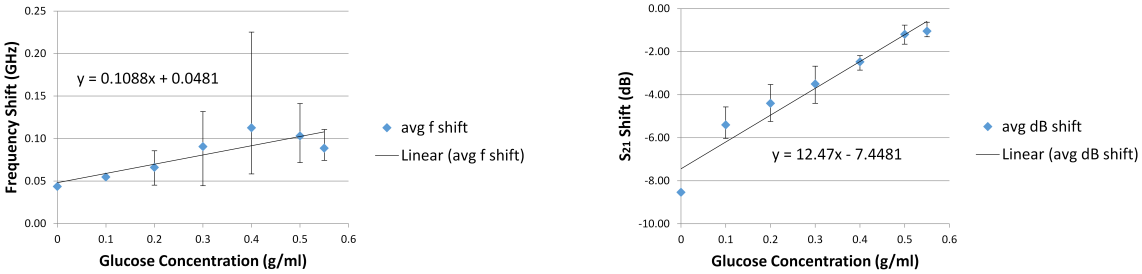


Figure 5.21. The effect of concentration on resonant frequency and dip value at 90 seconds.

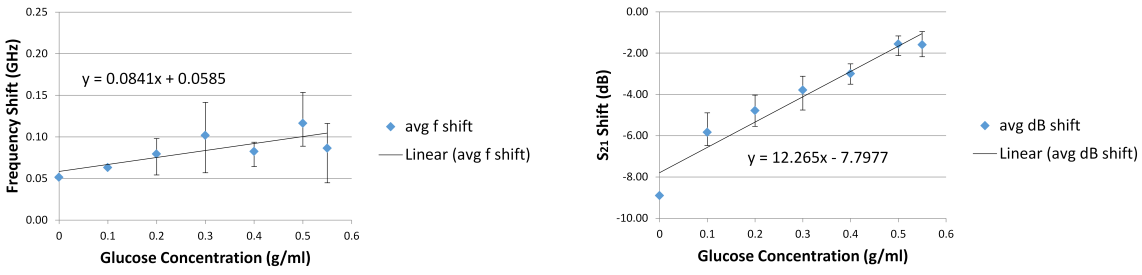


Figure 5.22. The effect of concentration on resonant frequency and dip value at 150 seconds.

5.5.4. The Effect of Reaction Time

In this last experiment, the resonance characteristics of SRR with respect to the reaction time is recorded for 10 minutes with 30 seconds time intervals. To observe the over-time response of SRR during the enzymatic reaction, solutions with different concentrations prepared. From each concentration, 1μl sample is placed in the reservoir. The reactive region is dissolved in the sample in the same way as the previous experiment. s_{21} data is saved for every 30 seconds, starting from the moment the patch first contacts the droplet up to 10 minutes. Figure 5.23 shows the resonant freqency change whereas Figure 5.24 shows the change in the depth of the resonance dip over reaction time for different concentrations.

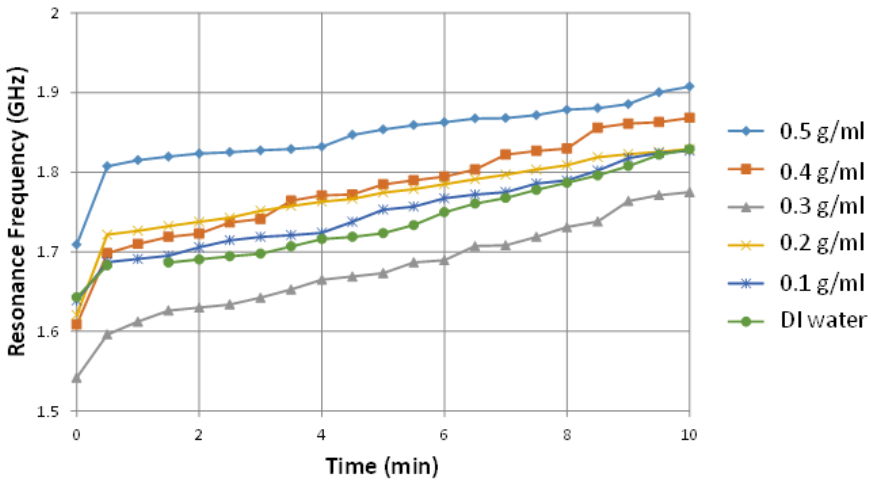


Figure 5.23. Resonant frequency change during reaction for different concentrations.

In Figure 5.23 and Figure 5.24, an increase in the resonant frequency and a decrease in the magnitude of the resonance dip is observed with respect to the increasing reaction time. However, there is no clear relationship between the resonance characteristics corresponding to different concentrations. For instance, in Figure 5.23, which shows the resonance frequency measurements, 0.3 g/ml concentration droplet seems to be an outlier, because its resonant frequency is the lowest during 10 minutes even though there less dense and denser droplets than 0.3 g/ml.

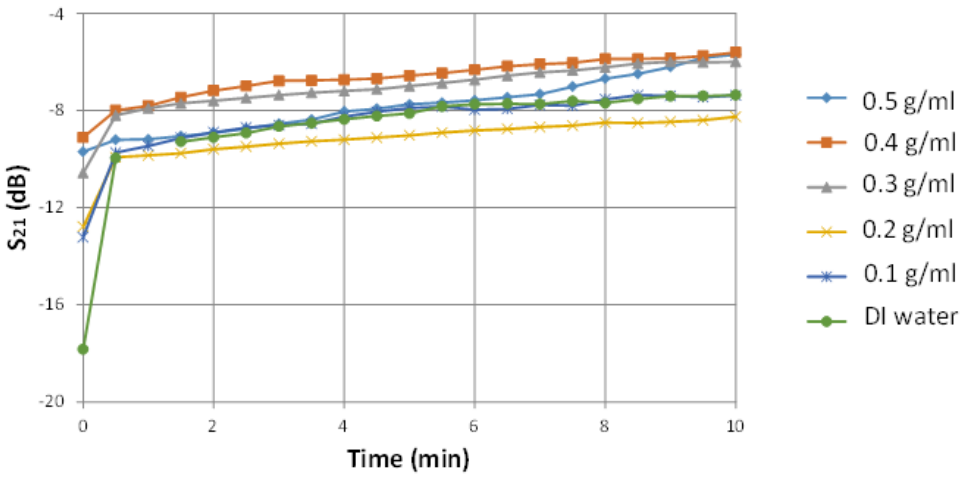


Figure 5.24. Resonance dip change during reaction for different concentrations.

Also we observe a frequency shift for DI water in the same table, which is an unexpected result. This result shows us that the shift in the frequency is not only a result of a chemical reaction of glucose with the enzyme. That is, there are several other reasons which may lead to a shift. Evaporation during the reaction time is the most probable major effect resulting this odd behavior of DI water. During this 10 minutes, the sample droplet evaporates and diminishes in volume. As it is measured in Section 5.5.2, as the volume of droplet is increased the shift in the resonant frequency increases. Reading this statement in reverse, as the droplet gets smaller by evaporation, the effect of droplet diminishes and the resonance starts to turn its unloaded situation.

The slope of each curve shows us how fast the resonant frequency or the depth of the resonant dip changes. However, we cannot find a pattern about the resonant frequency (or the resonance dip) changes over 10 minutes with respect to the glucose concentration, depending on this data.

Another interesting result is for all concentrations the slope of the curves is much higher between 0 and 30 seconds. After 30 seconds the all curves sits on approximately linear trendlines. There are two possible reasons for this. The first reason is the reaction is mostly completed in the first 30 second time interval. However, we observe

a similar behavior in DI case in which there should not be any reaction. This may have several causes. The major reason can be that even though the gap reservoir is cleaned and dried after every measurement, we may not be able to get rid of the previous sample completely, which may contaminate the reservoir and affect the next measurements.

If contamination is not the main reason for the behavior of DI, there is another possible explanation for the behavior of DI water in the first 30 seconds interval. Including the DI water case during the first 15 seconds of each measurement, the strip patch is held in contact with the solution droplet and then it is pulled away from the droplet. While pulling away the patch, it may steal some of the sample solution from the droplet due to cohesion so that the droplet gets smaller in volume immediately. An immediate decrease in volume will to rapid change of resonance characteristics towards the unloaded case. This may be a possible cause of high slopes between 0 and 30 seconds.

6. CONCLUSION

In this thesis the study on two separate resonator bioapplications were explained. The first bioapplication is about an optical catheter tracking system in MRI utilizing optical interconnects for power and data readout. In this thesis, two generations of MEMS modules which are fabricated by nickel electroplating method are studied. With the first generation MEMS devices, it is shown that the electroplating is a rapid and cost effective metal deposition technique which enables us with very low residual stress devices even with three times higher aspect ratios compared to the sputtering technique. Also it is shown that the first generation devices are functional in the measurement setup utilizing 0.62 T magnetic field in the laboratory environment. Therefore, it can be assumed that in a 3 T MRI environment they will be functional.

On the other hand, due to the fact that the second lithography is a negative lithography process using a negative photoresist the first generation devices do not allow metal deposition thicker than 1.5 μm. Also, since the device dimensions are comparable to the LDV beam size it is not possible to get response from multiple resonators which are necessary to cover up the required frequency interval.

The second generation MEMS devices are designed to satisfy these needs. The second generation devices designed in groups of resonators fitting in 60 μm diameter beam size. Six different groups are formed such that each group can cover a continuous frequency interval greater than 200 kHz. The beam type resonators and resonators with perforated masses are simulated in COMSOL and in SolidWorks to get the resonance frequency data of devices and DC displacement values, respectively. The fabrication of second generation resonators is not completed. 3 μm minimum feature size makes the fabrication challenging. In the second lithography process of the fabrication of second generation devices a positive photoresist can be used, which makes thicker metal deposition possible.

Once the fabrication of second generation MEMS devices is completed, they

can even be used in real surgical applications provided that they are integrated to a platform and to fibers very robust (see Figure 1.1). In this case there should be two fibers, one for the power transmission and the other for the readout. Integration to a small platform can be achievable through wire bonding of the CMOS IC and MEMS resonators. Integration of the fiber carrying the power laser to the IC, which is stationary, can be relatively easy compared to fiber optical integration to the MEMS devices. Since the MEMS devices are vibrating the fiber cannot be directly fixed on the MEMS devices. A possible solution can be a micron size V-groove and integrating the fibers on it instead. To focus the LDV beam on the MEMS devices gradient-index (GRIN) lens structures and reflective chambers can be used. However, this time the phase shift due to reflections from the chamber walls should be modelled carefully. Moreover, for the MEMS devices, the chamber should be able to collect the reflected light and and direct it back to the fiber cable without a significant loss.

In the second bioapplication part the theoretical background and the basic experimental study for an SRR based glucose sensor design is presented. The SRRs matched to 2 GHz are modelled analytically, simulated in CST and characterized experimentally. The behavior of SRR for different sample positions, volumes and concentrations and reaction time is studied experimentally.

It is found that the most sensitive parts of an SRR structure are the gap boundaries. As the volume size increases the resonance frequency shifts more. Since the relative dielectric constant of DI water is higher, the gap capacitance increases as the sample volume increases and the resonant frequency shifts towards lower frequencies. In the concentration experiment, for a predefined time interval, for denser samples the resonant frequency increases more and the magnitude of the resonance dip decreases more with respect to the initial resonance characteristics. In the last experiment about the reaction time, a shift in frequency and in resonance dip magnitude is observed for all samples with different concentrations with increasing reaction time. However, in this study, there is no pattern detected for the reaction time.

All experiments are conducted with an intense care. Any parasitic effects are

tried to be eliminated or minimized. However, the results of these experiments still cannot provide a very reliable quantification of the reaction effects on resonance. There are still so many parameters which should be kept under control during the experiment. First of all, the evaporation of droplets over time is a significant factor that can affect the measurement results. The most obvious proof of this effect is the resonant frequency shift observed for DI water in Section 5.5.4. The change in geometry of droplet due to its spreading over the gap can also affect the resonance behavior. Contamination due to the particles in the air or due to the remnants of the previous sample droplets can be an important cause for misleading experimental results. Therefore, the experiments should be repeated in clean room environment. Temperature change and even pH of the droplet can effect the results. The buffer solution is therefore very important to pay attention, because it arranges the pH of the droplet which affects the reaction kinematics. In short, all possible parameters should be kept under control as much as possible.

In the end, this device is planned to be used as a noninvasive, wearable contact lens blood glucose monitoring sensor as in [82] and [84]. Therefore it should be designed such that the reactive enzyme should be chained to the sensor face remaining functional for a few days. Also to regularly analyze only a required amount of tear sample, capillary chambers and microfluidic channel structures can be useful in the future steps.

REFERENCES

1. Reinhardt, H. and H. Landolt, "CT-Guided "Real Time" Stereotaxy", G. Broggi, J. Burzaco, E. Hitchcock, B. Meyerson and S. Tóth (Editors), *Advances in Stereotactic and Functional Neurosurgery 8*, Vol. 46 of *Acta Neurochirurgica Supplementum*, pp. 107–108, Springer Vienna, 1989.

2. Doshi, P., L. Lemmieux, D. Fish, S. Shorvon, W. Harkness and D. Thomas, "Frameless Stereotaxy and InteractiveNeurosurgery with the ISG Viewing Wand", B. Meyerson and C. Ostertag (Editors), *Advances in Stereotactic and Functional Neurosurgery 11*, Vol. 64 of *Acta Neurochirurgica Supplementum*, pp. 49–53, Springer Vienna, 1995.

3. Dyer, P., N. Patel, G. Pell, B. Cummins and D. Sandeman, "The ISG Viewing Wand: An Application to Atlanto-Axial Cervical Surgery Using the Le Fort I Maxillary Osteotomy", *British Journal of Oral Maxillofacial Surgery*, Vol. 33, No. 6, pp. 370–374, 1995.

4. Sipos, E., S. Tebo, S. Zinreich, D. Long and H. Brem, "In Vivo Accuracy Testing and Clinical Experience with the ISG Viewing Wand", *Neurosurgery*, Vol. 39, No. 1, pp. 194–202, 1996.

5. Hynynen, K., R. Roemer, D. Anhalt, C. Johnson, Z. X. Xu, W. Swindell and T. Cetas, "A Scanned, Focused, Multiple Transducer Ultrasonic System for Localized Hyperthermia Treatments", *International Journal of Hyperthermia*, Vol. 3, No. 1, pp. 21–35, 1987.

6. Hata, N., T. Dohi, H. Iseki and K. Takakura, "Development of a Frameless and Armless Stereotactic Neuronavigation System with Ultrasonographic Registration", *Neurosurgery*, Vol. 41, No. 3, pp. 608–613, 1997.

7. Nolte, L., L. Zamorano, H. Visarius, U. Berlemann, F. Langlotz, E. Arm and

O. Schwarzenbach, "Clinical Evaluation of a System for Precision Enhancement in Spine Surgery", *Clinical Biomechanics*, Vol. 10, No. 6, pp. 293–303, 1995.

8. Gumprecht, H., D. Widenka and C. Lumenta, "BrainLab VectorVision Neuronavigation System: Technology and Clinical Experiences in 131 Cases", *Neurosurgery*, Vol. 44, No. 1, 1999.

9. Vetterli, D., S. Thalmann, F. Behrensmeier, L. Kemmerling, E. J. Born, R. Mini, R. H. Greiner and D. M. Aebersold, "Daily Organ Tracking in Intensity-Modulated Radiotherapy of Prostate Cancer Using an Electronic Portal Imaging Device with a Dose Saving Acquisition Mode", *Radiotherapy and Oncology : Journal of the European Society for Therapeutic Radiology and Oncology*, Vol. 79, No. 1, p. 101—108, 2006.

10. Webster, J., *Minimally Invasive Medical Technology*, Tayor&Francis, Boca Raton, 2010.

11. Placidi, G., *MRI: Essentials for Innovative Technology*, Tayor&Francis, Boca Raton, 2012.

12. Horvath, K. A., M. Li, D. Mazilu, M. A. Guttman and E. R. McVeigh, "Real-Time Magnetic Resonance Imaging Guidance for Cardiovascular Procedures", *Seminars in Thoracic and Cardiovascular Surgery*, Vol. 19, No. 4, pp. 330–335, 2007.

13. Dickfeld, T., R. Kato, M. Zviman, S. Lai, G. Meininger, A. C. Lardo, A. Roguin, D. Blumke, R. Berger, H. Calkins and H. Halperin, "Characterization of Radiofrequency Ablation Lesions With Gadolinium-Enhanced Cardiovascular Magnetic Resonance Imaging", *Journal of the American College of Cardiology*, Vol. 47, No. 2, pp. 370–378, 2006.

14. Fink, C., M. Bock, R. Umathum, S. Volz, S. Zehlsdorff, R. Grobholz, H. Hauczor and P. Hallscheidt, "Renal Embolization: Feasibility of Magnetic Resonance-Guidance Using Active Catheter Tracking and Intraarterial Magnetic Resonance

Angiography", *Investigative Radiology*, Vol. 39, No. 2, pp. 111–119, 2004.

15. Tweedle, M. and K. Kumar, "Magnetic Resonance Imaging (MRI) Contrast Agents", M. Clarke and P. Sadler (Editors), *Metallopharmaceuticals II*, Vol. 2 of *Topics in Biological Inorganic Chemistry*, pp. 1–43, Springer Berlin Heidelberg, 1999.

16. Bernstein, M. A., K. F. King and X. J. Zhou, *Handbook of MRI Pulse Sequences*, Elsevier Academic Press, Burlington, MA, USA, 2004.

17. Camli, B., *Design and Characterization of the Power Supply Unit and Driver Blocks of a CMOS Based Localization System for MRI*, Master's Thesis, Bogazici University, 2013.

18. Sarioglu, B., M. Tumer, U. Cindemir, B. Camli, G. Dundar, C. Ozturk and A. Yalcinkaya, "An Optically Powered CMOS Tracking System for 3 T Magnetic Resonance Environment", *Biomedical Circuits and Systems, IEEE Transactions on*, Vol. 9, No. 1, pp. 12–20, Feb 2015.

19. Kouhani, M., B. Camli, A. Cakaci, E. Kusakci, B. Sarioglu, G. Dundar, H. Torun and A. Yalcinkaya, "Integrated Silicon Photovoltaics on CMOS with MEMS Module for Catheter Tracking", *Lightwave Technology, Journal of*, Vol. 33, No. 16, pp. 3426–3432, 2015.

20. Kang, T., J. Kim, J. Kim, K. Hwang, B. Lee, C. Baek, Y. Kim, D. Kwon, H. Lee and Y. Kim, "Deformation Characteristics of Electroplated MEMS Cantilever Beams Released by Plasma Ashing", *Sensors and Actuators A: Physical*, Vol. 148, No. 2, pp. 407–415, 2008.

21. Chao-Heng, C. and C. Shi-Hao, "Fabrication Comb-Drive Device by MEMS and Electroplating", *Design, Test, Integration and Packaging of MEMS/MOEMS 2003. Symposium on*, pp. 362–366, 2003.

22. Kouhani, M. H. M., *Electroplating RF MEMS Resonators and Optical Characterization*, Master's Thesis, Bogazici University, 2014.

23. Nayfeh, A., M. Younis and E. Abdel-Rahman, "Reduced-Order Models for MEMS Applications", *Nonlinear Dynamics*, Vol. 41, No. 1-3, pp. 211–236, 2005.

24. Zhang, W.-M., G. Meng and H.-G. Li, "Modeling and Simulation of the Squeeze Film Effect on the MEMS Structures", *Microwave Conference Proceedings, 2005. APMC 2005. Asia-Pacific Conference Proceedings*, Vol. 2, pp. 1–3, Suzhou, China, 2005.

25. Veijola, T., "Compressible Squeeze-Films in Vibrating MEMS Structures at High Frequencies", *Design, Test, Integration Packaging of MEMS/MOEMS, 2009. MEMS/MOEMS '09. Symposium on*, pp. 235–238, Rome, Italy, 2009.

26. Basak, S., A. Raman and S. V. Garimella, "Hydrodynamic Loading of Microcantilevers Vibrating in Viscous Fluids", *Journal of Applied Physics*, Vol. 99, No. 11, pp. 447–456, 2006.

27. Kouhani, M. H. M., A. Cakaci, E. Kusakci, H. Torun and A. D. Yalcinkaya, "Design, Fabrication and Characterization of a RF MEMS Resoantor for MRI Applications", *25th Micromechanics and Microsystems Europe Conference, 2014.*, Istanbul, Turkey, 2014.

28. Kusakci, E., M. H. M. Kouhani, B. Camli, A. U. Cakaci, H. Torun and A. D. Yalcinkaya, "MR Görüntüleme Uygulamaları İçin Üretilen RF MEMS Çınlayıcıların Test Edilmesi ve CMOS Tümleşik Devre Tarafından Sürülmesi", *16. Ulusal Optik, Elektro-Optik ve Fotonik Çalıştayı*, Kocaeli, Turkey, 2014.

29. Wylde, J. and T. Hubbard, "Elastic Properties and Vibration of Micro-Machined Structures Subject to Residual Stresses", *Electrical and Computer Engineering, 1999 IEEE Canadian Conference on*, Vol. 3, pp. 1674–1679, Edmonton, Canada, 1999.

30. Urey, H., C. Kan and W. O. Davis, "Vibration Mode Frequency Formulae for Micromechanical Scanners", *Journal of Micromechanics and Microengineering*, Vol. 15, No. 9, p. 1713, 2005.

31. Cakaci, A. U., *Electromagnetic MEMS-Based Resonator Design for Catheter Tracking in MRI*, Master's Thesis, Bogazici University, 2013.

32. Camli, B., B. Sarioglu and A. Yalcinkaya, "Photodiodes for Monolithic CMOS Circuit Applications", *Selected Topics in Quantum Electronics, IEEE Journal of*, Vol. 20, No. 6, pp. 336–343, 2014.

33. El-Sharkawy, A., M. Schär, P. Bottomley and E. Atalar, "Monitoring and Correcting Spatio-Temporal Variations of the MR Scanner's Static Magnetic Field", *Magnetic Resonance Materials in Physics, Biology and Medicine*, Vol. 19, No. 5, pp. 223–236, 2006.

34. Greil, G., T. Geva, S. E. Maier and A. J. Powell, "Effect of Acquisition Parameters on the Accuracy of Velocity Encoded Cine Magnetic Resonance Imaging Blood Flow Measurements", *Journal of Magnetic Resonance Imaging*, Vol. 15, No. 1, pp. 47–54, 2002.

35. Oniciu, L. and L. Mureşan, "Some Fundamental Aspects of Levelling and Brightening in Metal Electrodeposition", *Journal of Applied Electrochemistry*, Vol. 21, No. 7, pp. 565–574, 1991.

36. Chandrasekar, M. and M. Pushpavanam, "Pulse and Pulse Reverse Plating—Conceptual, Advantages and Applications", *Electrochimica Acta*, Vol. 53, No. 8, pp. 3313–3322, 2008.

37. Luo, J. K., A. J. Flewitt, S. M. Spearing, N. A. Fleck and W. I. Milne, "Young's Modulus of Electroplated Ni Thin Film for MEMS Applications", *Materials Letters*, Vol. 58, No. 17–18, pp. 2306–2309, 2004.

38. Moser, H. O., B. D. F. Casse, O. Wilhelmi and B. T. Saw, "Terahertz Response of a Microfabricated Rod-Split-Ring-Resonator Electromagnetic Metamaterial", *Phys. Rev. Lett.*, Vol. 94, p. 063901, 2005.

39. Wilbert, D. S., M. P. Hokmabadi, J. Martinez, P. Kung and S. M. Kim, "Terahertz Metamaterials Perfect Absorbers for Sensing and Imaging", Vol. 8585, 2013.

40. Kusakci, E., B. Camli, H. Torun and A. D. Yalcinkaya, "Narrowband Noise Figure Study with Split Ring Resonators for MRI Applications", *Microelectronics Technology, Circuits, and Systems for Space Applications Workshop, 2015.*, Istanbul, Turkey, 2015.

41. Smith, D. R., J. B. Pendry and M. C. K. Wiltshire, "Metamaterials and Negative Refractive Index", *Science*, Vol. 305, No. 5685, pp. 788–792, 2004.

42. Shalaev, V. M., "Optical Negative-Index Metamaterials", *Nature Photonics*, Vol. 1, pp. 41–48, 2006.

43. Shelby, R. A., D. R. Smith and S. Schultz, "Experimental Verification of a Negative Index of Refraction", *Science*, Vol. 292, No. 5514, pp. 77–79, 2001.

44. Shalaev, V. M., W. Cai, U. K. Chettiar, H.-K. Yuan, A. K. Sarychev, V. P. Drachev and A. V. Kildishev, "Negative Index of Refraction in Optical Metamaterials", *Optics Letters*, Vol. 30, No. 24, pp. 3356–3358, 2005.

45. Smith, D. R. and N. Kroll, "Negative Refractive Index in Left-Handed Materials", *Physical Review Letters*, Vol. 85, pp. 2933–2936, 2000.

46. Aydin, K. and E. Ozbay, "Identifying Magnetic Response of Split-Ring Resonators at Microwave Frequencies", *Opto-Electronics Review*, Vol. 14, pp. 193–199, 2006.

47. Zhang, X. and Z. Liu, "Superlenses to Overcome the Diffraction Limit", *Nature Materials*, Vol. 7, No. 6, pp. 435–441, 2008.

48. Torun, H., F. Top, G. Dundar and A. Yalcinkaya, "A Split-Ring Resonator-Based Microwave Sensor for Biosensing", *Optical MEMS and Nanophotonics (OMN), 2014 International Conference on*, pp. 159–160, Glasgow, UK, 2014.

49. Rho, J., Z. Ye, Y. Xiong, X. Yin, Z. Liu, H. Choi, G. Bartal and X. Zhang, "Spherical Hyperlens for Two-Dimensional Sub-Diffractional Imaging at Visible Frequencies", *Nature Communications*, Vol. 1, p. 143, 2010.

50. Schurig, D., J. J. Mock, B. J. Justice, S. A. Cummer, J. B. Pendry, A. F. Starr and D. R. Smith, "Metamaterial Electromagnetic Cloak at Microwave Frequencies", *Science*, Vol. 314, No. 5801, pp. 977–980, 2006.

51. Aydin, K., *Characterization and Applicaitons of Negative Index Metamaterials*, Ph.D. Thesis, Bilkent University, 2008.

52. Chen, T., S. Li and H. Sun, "Metamaterials Application in Sensing", *Sensors*, Vol. 12, No. 3, p. 2742, 2012.

53. Wang, J., "Electrochemical Glucose Biosensors", *Chemical Reviews*, Vol. 108, No. 2, pp. 814–825, 2008.

54. Blonde, L. and A. Kartner, "Current Evidence Regarding the Value of Self-Monitored Blood Glucose Testing", *The American Journal of Medicine*, Vol. 118, No. Suppl 9A, pp. 20S–26S, 2005.

55. Bergenstal, R. and J. Gavin, "The Role of Self-Monitoring of Blood Glucose in the Care of People with Diabetes: Report of a Global Consensus Conference", *The American Journal of Medicine*, Vol. 118, No. Suppl 9A, pp. 1S–6S, 2005.

56. Vacanti, J. P., M. A. Morse, W. M. Saltzman, A. J. Domb, A. Perez-Atayde and R. Langer, "Selective Cell Transplantation Using Bioabsorbable Artificial Polymers as Matrices", *Journal of Pediatric Surgery*, Vol. 23, No. 1, pp. 3–9, 1988.

57. Yoon, K., R. Quickel, K. Tatarkiewicz, T. Ulrich, J. Hollister-Lock, N. Trivedi, S. Bonner-Weir and G. Weir, "Differentiation and Expansion of Beta Cell Mass in Porcine Neonatal Pancreatic Cell Clusters Transplanted into Nude Mice", *Cell Transplantation*, Vol. 8, No. 6, pp. 673–689, 1999.

58. Turner, A. P., "Biosensors–Sense and Sensitivity", *Science*, Vol. 290, No. 5495, pp. 1315–1317, 2000.

59. Wang, J., "Glucose Biosensors: 40 Years of Advances and Challenges", *Electroanalysis*, Vol. 13, No. 12, pp. 983–988, 2001.

60. Clarke, S. F. and J. R. Foster, "A History of Blood Glucose Meters and Their Role in Self-Monitoring of Diabetes", *British Journal of Biomedical Science*, Vol. 69, No. 2, pp. 83–93, 2012.

61. Goldstein, D. E., R. R. Little, R. A. Lorenz, J. I. Malone, D. Nathan, C. M. Peterson and D. B. Sacks, "Tests of Glycemia in Diabetes", *Diabetes Care*, Vol. 27, No. 7, pp. 1761–1773, 2004.

62. Hayford, J. T., J. A. Wydert and R. G. Thompson, "Validity of Urine Glucose Measurements for Estimating Plasma Glucose Concentration", *Diabetes Care*, Vol. 6, No. 1, pp. 40–44, 1983.

63. Thomas, L. E., M. P. Kane, G. Bakst, R. S. Busch, R. A. Hamilton and J. M. Abelseth, "A Glucosemeter Accuracy and Precision Comparison: the FreeStyle Flash Versus the Accu-Chek Advantage, Accu-Chek Compact Plus, Ascensia Contour, and the BD Logic", *Clinical Chemistry*, Vol. 10, No. 2, pp. 102–110, 2008.

64. Tate, P. F., C. A. Clements and J. E. Walters, "Accuracy of Home Blood Glucose Monitors", *Diabetes Care*, Vol. 15, No. 4, pp. 536–538, 1992.

65. Dou, X., Y. Yamaguchi, H. Yamamoto, H. Uenoyama and Y. Ozaki, "Biological Applications of Anti-Stokes Raman Spectroscopy: Quantitative Analysis of

Glucose in Plasma and Serum by a Highly Sensitive Multichannel Raman Spectrometer", *Journal of Appied Spectroscopy*, Vol. 50, No. 10, pp. 1301–1306, 1996.

66. Shafer-Peltier, K. E., C. L. Haynes, M. R. Glucksberg and R. P. Van Duyne, "Toward a Glucose Biosensor Based on Surface-Enhanced Raman Scattering", *Journal of the American Chemical Society*, Vol. 125, No. 2, pp. 588–593, 2003.

67. March, W. F., B. Rabinovitch and R. L. Adams, "Noninvasive Glucose Monitoring of the Aqueous Humor of the Eye: Part II. Animal Studies and the Scleral Lens", *Diabetes Care*, Vol. 5, No. 3, pp. 259–265, 1982.

68. Larin, K. V., M. S. Eledrisi, M. Motamedi and R. O. Esenaliev, "Noninvasive Blood Glucose Monitoring With Optical Coherence Tomography: A Pilot Study in Human Subjects", *Diabetes Care*, Vol. 25, No. 12, pp. 2263–2267, 2002.

69. Caduff, A., E. Hirt, Y. Feldman, Z. Ali and L. Heinemann, "First Human Experiments with a Novel Non-Invasive, Non-Optical Continuous Glucose Monitoring System", *Biosensors and Bioelectronics*, Vol. 19, No. 3, pp. 209–217, 2003.

70. Malin, S. F., T. L. Ruchti, T. B. Blank, S. N. Thennadil and S. L. Monfre, "Noninvasive Prediction of Glucose by Near-Infrared Diffuse Reflectance Spectroscopy", *Clinical Chemistry*, Vol. 45, No. 9, pp. 1651–1658, 1999.

71. Aslan, K., J. R. Lakowicz and C. D. Geddes, "Nanogold-Plasmon-Resonance-Based Glucose Sensing", *Analytical Biochemistry*, Vol. 330, No. 1, pp. 145 – 155, 2004.

72. Das, S., D. N. Finegold and S. A. Asher, "Photonic Crystal Glucose-Sensing Material for Noninvasive Monitoring of Glucose", *Clinical Chemistry*, Vol. 50, No. 12, pp. 2353–2360, 2004.

73. Choi, H., J. Nylon, S. Luzio, J. Beutler and A. Porch, "Design of Continuous Non-Invasive Blood Glucose Monitoring Sensor Based On a Microwave Split Ring

Resonator", *RF and Wireless Technologies for Biomedical and Healthcare Applications (IMWS-Bio), 2014 IEEE MTT-S International Microwave Workshop Series on*, pp. 1–3, London, UK, 2014.

74. Song, K., U. Ha, S. Park, J. Bae and H.-J. Yoo, "An Impedance and Multi-Wavelength Near-Infrared Spectroscopy IC for Non-Invasive Blood Glucose Estimation", *Solid-State Circuits, IEEE Journal of*, Vol. 50, No. 4, pp. 1025–1037, 2015.

75. Szekely, J., A. Neumann and Y. Chuang, "The Rate of Capillary Penetration and the Applicability of the Washburn Equation", *Journal of Colloid and Interface Science*, Vol. 35, No. 2, pp. 273–278, 1971.

76. Jungheim, K. and T. Koschinsky, "Glucose Monitoring at the Arm: Risky Delays of Hypoglycemia and Hyperglycemia Detection", *Diabetes Care*, Vol. 25, No. 6, pp. 956–960, 2002.

77. Csoregi, E., D. W. Schmidtke and A. Heller, "Design and Optimization of a Selective Subcutaneously Implanted Glucose Electrode Based on "Wired" Glucose Oxidase", *Analytical Chemistry*, Vol. 67, pp. 1240–1244, 1995.

78. Heller, A. and B. Feldman, "Electrochemistry in Diabetes Management", *Accounts of Chemical Research*, Vol. 43, pp. 963–973, 2010.

79. Burritt, M. F., "Current Analytical Approaches to Measuring Blood Analytes.", *Clinical Chemistry*, Vol. 36, No. 8, pp. 1562–1566, 1990.

80. Vashist, S. K., D. Zheng, K. Al-Rubeaan, J. H. T. Luong and F.-S. Sheu, "Technology Behind Commercial Devices for Blood Glucose Monitoring in Diabetes Management: A Review", *Analytica Chimica Acta*, Vol. 703, No. 2, pp. 124–136, 2011.

81. Chu, M., S. Iguchi, D. Takahashi, T. Arakawa, H. Kudo and K. Mitsubayashi,

"Wearable Biosensor for Monitoring Tear Glucose on Rabbit Eye as Novel Device of Body Sensor Network", *Intelligent Sensors, Sensor Networks and Information Processing (ISSNIP), 2009 5th International Conference on*, pp. 191–194, Melbourbe, VIC, 2009.

82. Yao, H., A. Afanasiev, I. Lahdesmaki and B. Parviz, "A Dual Microscale Glucose Sensor on a Contact Lens, Tested in Conditions Mimicking the Eye", *Micro Electro Mechanical Systems (MEMS), 2011 IEEE 24th International Conference on*, pp. 25–28, Cancun, Mexico, 2011.

83. Liao, Y.-T., H. Yao, A. Lingley, B. Parviz and B. Otis, "A 3-μW CMOS Glucose Sensor for Wireless Contact-Lens Tear Glucose Monitoring", *Solid-State Circuits, IEEE Journal of*, Vol. 47, No. 1, pp. 335–344, 2012.

84. Yao, H., C. Marcheselli, A. Afanasiev, I. Lahdesmaki and B. Parviz, "A Soft Hydrogel Contact Lens with an Encapsulated Sensor for Tear Glucose Monitoring", *Micro Electro Mechanical Systems (MEMS), 2012 IEEE 25th International Conference on*, pp. 769–772, Paris, France, 2012.

85. Rapp, P., M. Mesch, H. Giessen and C. Tarín, "Regression Methods for Ophthalmic Glucose Sensing Using Metamaterials.", *Journal of Electrical and Computer Engineering*, Vol. 2011, pp. 953064:1–953064:12, 2011.

86. Baeyens, V. and R. Gurny, "Metamaterials Application in Sensing", *Pharmaceutica acta Helvetiae*, Vol. 72, No. 4, pp. 191–202, 1997.

87. King-Smith, P. E., B. A. Fink, R. M. Hill, K. W. Koelling and J. M. Tiffany, "The Thickness of the Tear Film", *Current Eye Research*, Vol. 29, No. 4-5, pp. 357–68, 2004.

88. Domschke, A., W. F. March, S. Kabilan and C. Lowe, "Initial Clinical Testing of a Holographic Non-Invasive Contact Lens Glucose Sensor", *Diabetes Technology & Therapeutics*, Vol. 8, No. 1, pp. 89–93, 2006.

89. Asher, S. A. and J. T. Baca, *Handbook of Optical Sensing of Glucose in Biological Fluids and Tissues*, chap. Tear Fluid Photonic Crystal Contact Lens Noninvasive Glucose Sensor, Taylor&Francis, 2008.

90. Berman, E. R., *Biochemistry of the Eye*, Vol. 19, Headington Hill Hall, New York, USA, 1991.

91. Sydoruk, O., E. Tatartschuk, E. Shamonina and L. Solymar, "Analytical Formulation for the Resonant Frequency of Split Rings", *Journal of Applied Physics*, Vol. 105, No. 1, p. 014903:1–014903:4, 2009.

92. Pozar, D. M., *Microwave Engineering*, John Wiley & Sons, Inc., Hoboken, NJ, USA, 2005.

93. Raba, J. and H. A. Mottola, "Glucose Oxidase as an Analytical Reagent", *Critical Reviews in Analytical Chemistry*, Vol. 25, No. 1, pp. 1–42, 1995.

94. Kirk, O., T. V. Borchert and C. C. Fuglsang, "Industrial Enzyme Applications", *Current Opinion in Biotechnology*, Vol. 13, No. 4, pp. 345–351, 2002.

95. Wong, C., K. Wong and X. Chen, "Glucose Oxidase: Natural Occurrence, Function, Properties and Industrial Applications", *Applied Microbiology and Biotechnology*, Vol. 78, No. 6, pp. 927–938, 2008.